Titre: Title:	Optical Power Beaming in the Lunar Environment
Auteur: Author:	Mohamed Naqbi
Date:	2024
Type:	Mémoire ou thèse / Dissertation or Thesis
Référence: Citation:	Naqbi, M. (2024). Optical Power Beaming in the Lunar Environment [Mémoire de maîtrise, Polytechnique Montréal]. PolyPublie. https://publications.polymtl.ca/61053/

POLYTECHNIQUE MONTRÉAL
affiliée à l'Université de Montréal

Optical Power Beaming in the Lunar Environment

MOHAMED NAQBI
Département de génie électrique

Mémoire présenté en vue de l'obtention du diplôme de *Maîtrise ès sciences appliquées*
Génie aérospatial

Novembre 2024

POLYTECHNIQUE MONTRÉAL
affiliée à l'Université de Montréal

Ce mémoire intitulé :

Optical Power Beaming in the Lunar Environment

présenté par **Mohamed NAQBI**
en vue de l'obtention du diplôme de *Maîtrise ès sciences appliquées*
a été dûment accepté par le jury d'examen constitué de :

Raman KASHYAP, président
Gunes KARABULUT KURT, membre et directrice de recherche
Sébastien LORANGER, membre et codirecteur de recherche
Roman KRUZELECKY, membre

DEDICATION

To my family and friends,

ACKNOWLEDGEMENTS

First of all, I would like to express my deep gratitude to my research director, Prof. Gunes Karabulut Kurt, as well as my co-director, Prof. Sébastien Loranger, for their support throughout my master's degree. Gunes, I am very grateful for your trust, your guidance throughout this journey, your humanity, and your encouragement, regardless of the circumstances. Sébastien, I would like to praise your rigor, patience, and valuable advice that guided me to the completion of this work. Your optimism and confidence allowed me to overcome the obstacles encountered along the way. I also thank you for all the opportunities and flexibility you have offered me.

I would also like to express my most sincere thanks to my family and friends for their support throughout my academic journey. None of this would have been possible without your encouragement. To my office colleagues, thank you for our discussions, our laughs, our shared working hours, as well as for your advice and support, especially Eray Guven, Leila Marandi, and Pablo Emilio Camacho. I would also like to thank Baris Donmez and Irfan Azam for our enriching discussions and their help. Finally, I thank the École Polytechnique de Bruxelles for selecting me to pursue a double-degree at Polytechnique Montréal and thank everyone who played a role, directly or indirectly, in the completion of my studies, and whom I may have forgotten to mention.

Lastly, I would like to thank the financial support, specifically the Tier 1 Canada Research Chair program.

RÉSUMÉ

L'intérêt croissant mondial pour l'exploration lunaire nécessite des solutions énergétiques fiables pour des activités telles que la recherche scientifique, l'exploitation minière et l'habitation dans l'environnement hostile de la Lune. Les sources d'énergie traditionnelles et les systèmes de distribution font face à des défis importants en raison des fluctuations de température extrêmes et des cycles jour-nuit prolongés sur la Lune. Pour remédier à ces problèmes, la transmission de puissance par faisceau optique (*optical power beaming*, OPB) a émergé au cours des dernières années comme une solution prometteuse dans le cadre d'opérations lunaires. Depuis son apparition, la recherche sur l'OPB s'est principalement concentrée sur l'amélioration des efficacités de conversion au niveau des composants et sur la démonstration expérimentale de sa faisabilité pour des applications à petite échelle. En parallèle, des études sur l'exosphère lunaire ont apporté de nouvelles perspectives sur l'environnement de la Lune, notamment en révélant la présence de poussières dans cette exosphère, susceptibles de perturber divers systèmes sur place, comme les transmissions optiques. Ainsi, une lacune de recherche a émergé, à savoir si la poussière lunaire soulevée pouvait atténuer les transmissions optiques de haute puissance. De manière plus générale, les études existantes n'offrent pas de modèles complets intégrant à la fois les facteurs optiques, thermiques et environnementaux nécessaires pour évaluer la performance de l'OPB dans l'environnement lunaire. Par conséquent, cette recherche vise à combler ces lacunes en évaluant d'abord l'impact potentiel de la poussière lunaire soulevée sur la transmission d'énergie, puis en optimisant la performance du système OPB pour récolter efficacement de l'énergie à longue distance sur la Lune, tout en respectant les contraintes de taille, de poids et de puissance (*size, weight, and power*, SWaP).

Pour ce faire, nous avons mené une étude théorique et des simulations. Ces dernières ont initialement évalué les pertes de transmission dues à la poussière lunaire soulevée en utilisant la théorie de Mie et ont évalué la performance de la récolte d'énergie avec un modèle de lien optique en espace libre. Reconnaissant les limitations de cette approche initiale, nous avons amélioré le modèle en employant la théorie du faisceau gaussien pour la récolte d'énergie et la propagation du faisceau, ainsi que la méthode T-matrix pour modéliser l'atténuation due aux particules de poussière. Par la suite, des contraintes de gestion thermique ont été intégrées au modèle, en considérant les limitations du refroidissement radiatif dans l'environnement lunaire. Des simulations ont été réalisées pour les scénarios OPB sol-sol et orbite-sol, en optimisant des paramètres de conception clés tels que les tailles des ouvertures des émetteurs et des récepteurs, et en utilisant des données réalistes à jour pour évaluer la performance de

l'OPB pour les missions lunaires.

Nos résultats indiquent que la poussière lunaire électrostatiquement soulevée peut significativement atténuer la transmission de puissance optique près de la surface dans les zones illuminées de la Lune. Néanmoins, en positionnant les émetteurs et les récepteurs à des altitudes plus élevées, nous pouvons efficacement réduire l'impact de la poussière et améliorer l'efficacité de la transmission. Nous avons également abordé l'importance de l'optimisation optique et des capacités de dissipation thermique pour respecter les contraintes SWaP, et démontré la capacité du système à alimenter un récepteur distant de plusieurs kilomètres, nécessitant quelques kilowatts pour fonctionner. Dans le scénario orbite-sol, nous avons identifié les orbites gelées de basse altitude de la Lune comme optimales pour les satellites solaires afin de fournir de l'énergie pendant la nuit lunaire et avons montré, à travers des simulations, qu'une couverture quasi-continue est nécessaire pour soutenir des systèmes de support de vie et réduire la dépendance à des systèmes de stockage d'énergie à grande échelle. En conclusion, nous démontrons que bien que l'impact de la poussière lunaire puisse être significatif, des approches de conception stratégiques peuvent efficacement atténuer cet effet. De plus, nous établissons que l'OPB est une solution faisable et efficace pour fournir une énergie fiable sur la Lune. Ces résultats soutiennent une exploration et une habitation durables pour les futures missions lunaires.

ABSTRACT

The rising global interest in lunar exploration necessitates reliable power solutions for activities such as scientific research, mining, and habitation in the Moon's harsh environment. Traditional power sources, and distribution systems, face significant challenges due to the Moon's extreme temperature fluctuations and prolonged day-night cycles. To address these issues, optical power beaming (OPB) has emerged over the past years as a promising solution. Since its inception, research on OPB has principaly focused on enhancing end-to-end efficiencies at the component level and experimentally demonstrating its feasibility for small-scale applications. In parallel, studies have increasingly provided new insights into the lunar environment, such as the dusty exosphere, which could disrupt many on-site systems, including optical transmissions. Thus, a gap has emerged in assessing whether lofted lunar dust (LLD) can attenuate high-power optical transmission. More generally, existing studies do not offer comprehensive models that integrate optical, thermal, and environmental factors necessary to evaluate the performance of OPB in the lunar environment. As a consequence, this research aims to address these gaps by first evaluating whether LLD affects power transmission, and then by optimizing the OPB system's performance to efficiently harvest energy over long distances on the Moon, while adhering to size, weight, and power (SWaP) constraints.

To achieve this, we conducted a theoretical and simulation-based study that initially assessed transmission losses due to LLD using Mie theory and evaluated energy harvesting performance with a line-of-sight (LoS) free-space optics (FSO) link model. Recognizing limitations in this initial approach, we improved the model by employing Gaussian beam theory for energy harvesting and beam propagation, and the T-matrix method to model attenuation due to LLD. Then, thermal management constraints were integrated into the model, considering the limitations of radiative cooling in the lunar environment. Simulations were performed for both ground-to-ground and orbit-to-ground OPB scenarios, optimizing key design parameters such as transmitter and receiver aperture sizes, and using up-to-date realistic data to assess the performance of OPB for lunar missions.

Our results indicate that electrostatically LLD can significantly attenuate optical power transmission near the surface in the illuminated parts of the Moon. However, by positioning transmitters and receivers at higher elevations, we effectively reduced dust impact and enhanced transmission efficiency. We also addressed the importance of optical optimization

and thermal dissipation capabilities to meet SWaP constraints, and demonstrated the system's ability to power a receiver located several kilometers away, requiring a few kilowatts to operate. In the orbit-to-ground scenario, we identified low lunar frozen orbits as optimal for solar-powered satellites to provide power during the lunar night and showed through simulations that near-continuous coverage is necessary to support life support systems and reduce reliance on large-scale energy storage. In conclusion, we demonstrate that although the impact of LLD on high-power optical transmission can be significant, strategic design approaches can effectively mitigate this effect. Furthermore, we establish that OPB is a feasible and efficient solution for delivering reliable power on the Moon. These findings support sustainable exploration and habitation for future lunar missions.

TABLE OF CONTENTS

LIST OF TABLES

LIST OF FIGURES

LIST OF SYMBOLS AND ACRONYMS

OPB	Optical Power Beaming
SWaP	Size, Weight, and Power
LLD	Lofted Lunar Dust
SPS	Solar-Powered Satellites
PV	Photovoltaic
WPT	Wireless Power Transmission
LoS	Line-of-Sight
LPC	Laser Power Converter
PCE	Power Conversion Efficiency
FSO	Free-Space Optics
EHCE	Energy Harvesting Conversion Efficiency
UAVs	Unmanned Aerial Vehicles
PSRs	Permanently Shadowed Regions
DDA	Discrete Dipole Approximation
VSWFs	Vector Spherical Wave Functions

LIST OF APPENDICES

CHAPTER 1 INTRODUCTION

1.1 Context and Motivation

The renewed global focus on lunar exploration, driven by both governmental space agencies and private enterprises, emphasizes the growing ambition to establish sustainable infrastructure on the Moon. This is exemplified by initiatives such as NASA's Artemis program, which aims to return humans to the lunar surface and develop a long-term presence [4]. An important aspect of this ambition is the provision of reliable and adaptable power systems to support a wide range of activities, including scientific research, resource extraction, and human habitation [5]. The lunar south pole has emerged as a key location for these activities and is the planned landing place for the future Artemis missions. The programmed operations in lunar craters in this region will require significant power, particularly for mobile platforms like rovers engaged in mining or prospecting for resources such as water ice or minerals [6].

Powering these platforms could be achieved through various methods: batteries, fuel cells, nuclear energy, reflected solar power, tethers, or power beaming. Each of these options has pros and cons, and their challenges are exacerbated by the Moon's long day-night cycles, which last about two weeks. For instance, solar photovoltaic (PV) systems, while effective during the lunar day, become inoperative during the 14-day lunar night and are limited to areas receiving direct sunlight, thus excluding areas within permanently shadowed craters. On the other hand, nuclear reactors have also often been highlighted for their capacity to offer continuous power, but involve significant logistical challenges due to their mass, the need for shielding, and safety concerns [7].

In addition, extreme lunar temperature variations, ranging from 121°C during the day at the equator to -246°C in crater floors at night [8], pose thermal challenges, requiring substantial energy to keep equipment operational. In order to effectively address these challenges while minimizing the mass and volume of mobile platforms, it is preferable to deliver energy from external sources rather than integrating power generation directly into the system. Thus, an efficient way of distributing energy in the lunar environment is needed. While electrical cables are reliable on Earth, they become highly impractical on the Moon due to their significant mass and deployment difficulties. Each kilogram of material sent to the Moon requires a large amount of fuel for both launch and landing, which greatly increases the overall cost

of the mission. Additionally, placing cables on the Moon's rough and dusty surface would create more practical difficulties, especially for maintenance and durability, partly due to the roughness of lunar dust [7]. Moreover, another issue with tethers is I^2R losses, where resistance causes energy dissipation as heat when current flows through the conductor. Since resistance increases with tether length, longer distances lead to greater losses, reducing transmission efficiency and causing heating that can weaken the tether, particularly in extreme environments like the Moon.

To address these challenges, wireless power transmission (WPT) emerges as a promising solution, especially where an unobstructed line-of-sight (LoS) is possible. Table 1.1 compares three transmission techniques, which are cables, microwaves, and laser across several metrics, highlighting their suitability for lunar applications. Microwave power transmission requires bulky hardware and large antennas, making it less suitable for scalable lunar operations [9]. In contrast, the use of optical power beaming (OPB) allows for more lightweight and compact equipment [10]. It emerges as the best solution and furthermore offers several other advantages in the lunar context, compared to Earth-based systems. Indeed, the absence of an atmosphere eliminates issues such as turbulence and scintillation, atmospheric absorption and scattering, as well as weather related disruptions, all of which are significant challenges on Earth.

Table 1.1 Transmission Techniques Comparison (P: Poor, G: Good, E: Excellent).

Metrics	**Cables**	**Microwave**	**Laser**
Mass per Distance	P	G	E
Effort per Distance	P	G	E
Power per Volume	E	P	G
Mass per Power	G	P	G
Hardware Size	G	P	G
Other Concerns	Maintenance & Low mobility	Size & RF Interference	Thermal Management & Dust

However, implementing OPB on the Moon presents also several challenges. A key issue is thermal management, as the absence of an atmosphere prevents convective cooling, leaving

radiation as the only means of dissipating heat [11]. This creates difficulties for maintaining optimal operating temperatures, especially in high-power systems. One can also mention the challenge of beam misalignment, which occurs due to the Moon's irregular terrain or mechanical vibrations, affecting the accuracy of the laser beam [12].

Another significant challenge is the presence of lunar dust. Firstly, because it can stick to the surfaces of equipment, including optical components, potentially blocking or damaging them. This problem has been addressed, and solutions like electrodynamic dust shields have been proposed to help keep critical surfaces clear of dust [13]. Secondly, it can loft into the lunar exosphere and potentially disrupt laser transmission through mechanisms of scattering and absorption [14]. This phenomenon arises due to electrostatic processes and micrometeoroid impacts, which are unique to the lunar environment [15–17]. During the lunar day, tiny particles of lunar dust become positively charged through photoelectric effects from sunlight. At night, they are negatively charged due to bombardment by energetic electrons in plasma. Additionally, micrometeoroid impacts provide sufficient kinetic energy to eject particles from the lunar surface into the exosphere. These combined processes, coupled with the Moon's low gravity, facilitate the lofting of dust particles into the lunar exosphere [17, 18]. This phenomenon has been proposed to explain the lunar horizon glow observed during the Apollo missions [19].

1.2 Functional Architecture

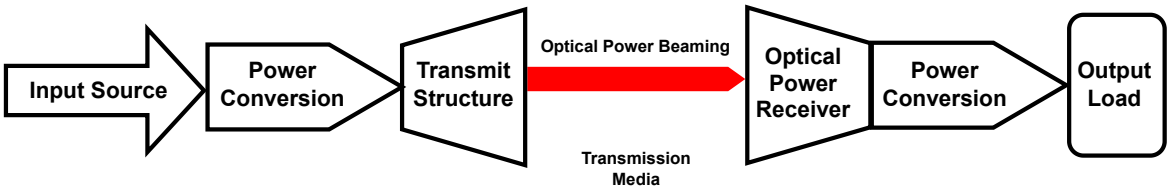

Figure 1.1 Functional blocks for an optical power beaming system.

The functional architecture of the OPB system is explained through its main components: the transmitter, the transmission media, and the receiver, as shown in Figure 1.1. The system starts with an energy source suitable for lunar conditions, which might include options like nuclear power generators and fission surface power systems, solar panels, hydrogen fuel cells and battery systems. This input energy goes through an initial power conversion process, which provides power not only for transmission to the final load but also for supporting

subsystems like thermal management and control units.

Next is the transmission structure, which connects the energy source to the transmission medium. This part includes devices like apertures, lenses, and gimbaling mechanisms to shape and direct the laser beam efficiently. Proper beam shaping and alignment are key to making sure the beam reaches the receiver collector well. After that, the beam will traverse the lunar environment, where it may interact with lunar dust, potentially resulting in efficiency losses.

After traveling through the transmission medium, the beam reaches the receiving collector, which captures it and sends it to the power conversion unit. The optical receiver changes the monochromatic laser light into electrical power, and the efficiency of this step determines how much energy is effectively captured. Proper thermal management is needed to keep the receiver at the right temperature, ensuring good efficiency and preventing overheating.

Once converted, the electrical energy is managed and sent to the output load, which could include various uses like powering rovers or other systems on the Moon. While this step is technically outside the power beaming system, it still affects how the earlier parts are designed, especially regarding the amount and reliability of the power needed by the load. The requirements of the output load can therefore set performance standards for the whole beaming system, making sure the delivered energy is practical for use on the Moon. Different technologies can be used for each of these main components, and later chapters will discuss how different choices can affect the overall system.

1.3 Research Objectives

This master's thesis presents an approach to analyzing OPB performance in the lunar environment. Specifically, the research objectives are threefold:

- To quantitatively evaluate the impact of lofted lunar dust (LLD) on optical power transmission.
- To optimize the OPB system to maximize transmission distance, while minimizing the aperture sizes and capturing most of the power (adhering to SWaP constraints).

- To evaluate the feasibility of OPB by quantitatively analyzing the harvested power under realistic, up-to-date conditions.

To do this, a theoretical and simulation-based study is conducted. We first build a LoS free-space optics (FSO) link model to assess size, weight, and power (SWaP) performance, and apply Mie theory to evaluate attenuation due to LLD. Recognizing the shortcomings of this approach, we then use Gaussian beam theory to further evaluate SWaP performance for optimum transmission distance and employ the T-matrix method to assess the effects of LLD. Following this, we investigate the effect of thermal management on the model to analyze its impact on SWaP. These objectives are analyzed for three scenarios: ground-to-ground OPB in both the illuminated and dark regions of the Moon, and orbit-to-ground OPB, using up-to-date and realistic data available in the literature.

1.4 Structure of the Master's Thesis

The remainder of this Master's thesis is organized into six chapters. Chapter 2 provides a review of the relevant literature. Chapter 3 presents the details of our initial problem approach and its shortcomings. Based on this, Chapter 4 presents our final approach, results and discussions. Chapter 5 extends our findings to analyze an orbit-to-ground configuration. Finally, Chapter 6 offers a conclusion, along with suggestions for future work.

1.5 Contributions

This section summarizes the main contributions, as well as the publications that resulted from this Master's thesis, and the poster presentations.

The main contributions are the following:

- We establish a LLD attenuation model based first on the Mie theory and radiative transfer theory. We then refine our results using the T-matrix method to provide a more accurate representation of dust particle shapes.
- We present a comprehensive system model for ground-to-ground OPB on the lunar surface, incorporating realistic and up-to-date data from existing literature and accounting for optical, thermal, and environmental considerations to optimize SWaP performance.

- We perform simulation studies to quantitatively assess the impact of LLD on laser transmission efficiency at various heights above the surface and transmission distances.
- We assess the harvested power under realistic conditions, considering varying transmitted powers and distances, and identify operating heights to minimize dust related losses.
- We discuss the design choices for transmitter and receiver apertures, while addressing optical and thermal constraints, to optimize the transmission distance.
- We extend our findings for an analysis of an orbit-to-ground scenario, using frozen orbits to optimize net harvested power (adhering to SWaP constraints).

The publications that resulted from this Master's thesis, and the external poster presentations are the following:

Conference paper (peer-reviewed)

C1. **Mohamed Naqbi**, Sébastien Loranger and Gunes Karabulut Kurt. *Impact of Lunar Dust on Free Space Optical (FSO) Energy Harvesting.* In: 2024 IEEE Aerospace Conference.

Journal paper (peer-reviewed)

J1. **Mohamed Naqbi**, Sébastien Loranger and Gunes Karabulut Kurt. *Optical Power Beaming in the Lunar Environment*, IEEE Transactions on Aerospace and Electronic Systems. October 2024. To be submitted.

Presentations

P1. *Lunar Laser Power Beaming (LPB) : Thermal Management (TM)*, Canadian Space Agency Lunar Workshop, Montréal, QC, Canada. June 2023.

P2. *Lunar Laser Power Beaming (LPB) : Thermal Management (TM)*, STARaCom AGM, Montréal, QC, Canada. June 2023.

CHAPTER 2 LITERATURE REVIEW

In this chapter, we present a literature review that begins with a broad overview of the challenges in the lunar environment, with particular emphasis on the issues associated with LLD and thermal management. Following this, we provide an overview of the evolution of wireless power transmission, gradually narrowing down to focus specifically on high intensity OPB.

2.1 Lunar Exploration and Environmental Challenges

Lunar exploration has undergone significant evolution since the initiation of space missions in the 1950s. The Apollo program, spanning from 1969 to 1972, marked a considerable achievement by returning lunar rock samples and precious data that significantly advanced scientific understanding of the Moon's composition and geological history [20]. Despite these accomplishments, the Apollo missions were primarily limited to near-equatorial regions on the near side of the Moon, leaving the polar areas and the far side largely unexplored.

In the decades following Apollo, enthusiasm for lunar exploration diminished. However, the early 2000s witnessed a resurgence of interest as the Moon was recognized as a crucial step for future space endeavors. Responding to this renewed focus, NASA commissioned the National Research Council (NRC) to develop a comprehensive report titled "The Scientific Context for Exploration of the Moon" [21]. This report outlined eight key scientific concepts and prioritized goals, emphasizing the importance of understanding the Moon's origin, geological evolution, and potential resources.

The NRC suggested focusing on the lunar south pole because of its unique environmental conditions and promising scientific opportunities [22]. The polar regions are particularly intriguing because they host permanently shadowed regions (PSRs) areas that have remained without direct sunlight for billions of years [23]. These PSRs, typically situated in deep craters near the lunar poles, maintain extremely low temperatures, dropping below -200 degrees Celsius. Such conditions enable the accumulation and preservation of volatiles like water ice [23]. The presence of these volatiles holds profound implications not only for understanding the history of volatile delivery to the Moon but also for their potential utilization as resources to support future lunar missions, including life support and propellant production.

Subsequent remote sensing missions have reinforced the evidence for water ice in these shadowed regions. Instruments aboard NASA's Lunar Reconnaissance Orbiter detected spectral signatures indicative of hydroxyl and water molecules, thereby affirming earlier hypotheses regarding lunar volatiles [24]. These discoveries have made the strategic importance of PSRs clear and have influenced the selection of landing sites for upcoming missions. Due to the presence of "peaks of eternal light" (zones which receive almost continuous sunlight) also present in these regions, the conditions are ideal for the application of OPB. Indeed, it could provide a continuous power supply in shadowed areas by transmitting energy wirelessly from illuminated regions [6].

While the prospects for exploration are promising, the lunar environment presents significant challenges, particularly concerning thermal management and lunar dust. Without an atmospheric medium, convective heat transfer is nonexistent on the lunar surface, making radiation the only way to dissipate heat [25]. This, coupled with extreme temperature fluctuations between lunar day and night, from 121°C during the day at the equator to -246°C in crater floors at night [8], impose thermal stresses on mission equipment, requiring robust solutions to maintain system integrity and functionality. This critical aspect is well-documented in the literature, where thermal control strategies often rely on high-emissivity radiators to enhance radiative cooling and multilayer insulation to limit thermal exchanges [26].

During early missions like Surveyor and Apollo, astronauts observed a phenomenon known as lunar horizon glow, which was attributed to the scattering of sunlight on suspended dust particles [27]. Observations from the Apollo 17 mission suggested that dust particles as small as 0.1 micrometers could ascend to considerable altitudes, leading to dust concentrations of tens of thousands of particles per cubic meter at higher elevations and up to 500,000 particles per cubic meter closer to the lunar surface [28, 29].

These findings indicated that electrostatic forces might be responsible for lofting dust particles above the lunar surface, potentially affecting both equipment functionality and scientific measurements. However, more recent data from the Lunar Dust Experiment (LDEX) aboard the Lunar Atmosphere and Dust Environment Explorer (LADEE) mission in 2013 provided new insights. LDEX investigated dust distribution between altitudes of 3 to 250 kilometers and observed lower dust levels than previously estimated. The experiment revealed that high-altitude dust particles were predominantly generated by high-velocity micrometeoroid

impacts and confirmed a decrease in dust density with increasing altitude [30]. Notably for this thesis, the mission found no evidence of dust being lofted electrostatically within this altitude range, suggesting that such lofting is primarily a near-surface phenomenon.

Theoretical investigations have continued to explore the dynamics of electrostatically lofted lunar dust and its implications for exploration activities. Lunar dust particles are present during both the lunar day and the lunar night, with their charging states varying due to environmental conditions. During the lunar day, they become positively charged through photoelectric effects from sunlight. At night, they are negatively charged due to bombardment by energetic electrons in plasma. These dynamic charging processes, coupled with the Moon's low gravity, facilitate the lofting of dust particles into the lunar exosphere, making them a persistent phenomenon throughout the lunar cycle [18]. Stubbs *et al.* [31] developed a model demonstrating that small dust particles could ascend to several kilometers above the surface due to electrostatic repulsion caused by the charging of dust particles through solar ultraviolet radiation. Popel *et al.* [32] expanded upon this by presenting a self-consistent description of the plasma-dust system over the illuminated lunar surface, integrating interactions among dust particles, solar wind, and photoelectrons, as illustrated in Figure 2.1. More recently, Zelenyi *et al.* [15] further examined the complexities of dusty plasma systems near the Moon, highlighting the challenges associated with modeling and measuring these phenomena. This near-surface phenomenon, known as electrostatic lofting, contrasts with high-altitude lofting caused by micrometeorite impacts, which can propel particles to significant altitudes, as depicted in Figure 2.1.

As a consequence, for ground-to-ground transmission, lunar dust creates challenges. One primary concern is that lunar dust sticks to equipment surfaces due to electrostatic charging, potentially causing damage [15]. To mitigate this problem, solutions like electrodynamic dust shields have been proposed. These systems employ electric fields to repel dust particles from critical surfaces, in order to maintain equipment functionality [13]. In this thesis, the challenge we will address is the potential interference of LLD with optical power transmission. Indeed, dust particles are of concern as they could scatter and absorb laser light, leading to energy loss. This specific problem was recently formulated by NASA [33] and, to the best of our knowledge, has not yet been addressed in the literature. We will therefore aim to answer it in this thesis.

For this, light interaction with particles needs to be studied. Mie theory, formulated by

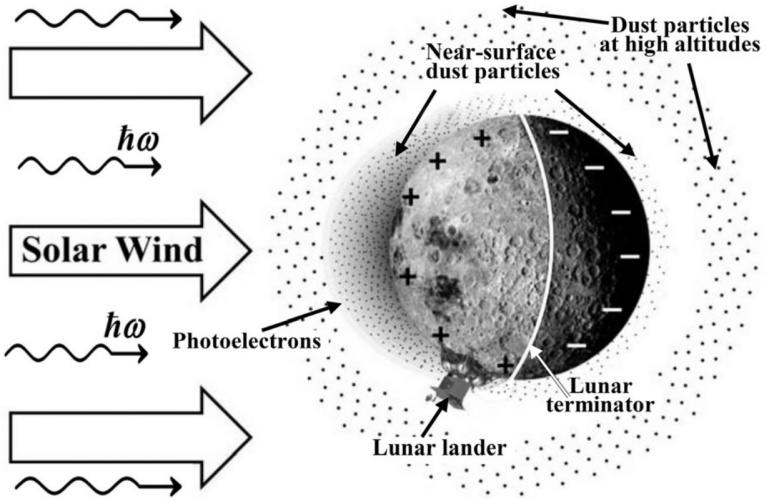

Figure 2.1 The main elements characterizing the dusty plasma system over the Moon (the terminator, the photoelectrons, the near-surface dust particles, dust particles at high altitudes, photons of solar radiation, and the solar wind). Reprinted from [1], with the permission of AIP Publishing.

Gustav Mie in 1908, provides an exact analytical solution to Maxwell's equations for light scattering and absorption by spherical particles of any size [34]. It accounts for complex refractive indices and helps calculate scattering efficiencies and other optical properties. For non-spherical particles, the T-matrix method generalizes scattering analysis. Introduced by Waterman in 1965 [35], it uses transition matrices (T-matrices) to compute scattering and absorption by particles of arbitrary shape [36].

Other scattering theories apply under specific conditions. Rayleigh scattering is used for very small particles compared to the wavelength, with intensity inversely proportional to the fourth power of the wavelength [37]. For much larger particles, ray-tracing methods are often used [38]. One can also mention the discrete dipole approximation (DDA) used to solve complex particle problem, including intricate internal structures, by representing them as polarizable points [39]. In this thesis, the wavelength of the optical beam will be on the same order of magnitude as the particle sizes being studied. For this reason and because of the specific geometry chosen to represent these particles, only Mie theory and the T-matrix method will be analyzed. These methods are more advantageous and far less complex than DDA, offering precise and less expensive solutions in terms of computational resources. On the other hand, radiative transfer theory will be studied to provide a framework for understanding electromagnetic radiation propagation through scattering and absorbing media [40].

2.2 Wireless Power Transmission (WPT)

WPT is an innovative technology that allows energy to be transmitted from a source to a target device without the need for physical connectors [41]. WPT has gained considerable attention in recent years, moving from an academic concept to a commercially viable solution. The growth of mobile devices and the increasing need for convenient and flexible power delivery have driven significant research into WPT technologies, including inductive coupling, magnetic resonance, radio frequency based power transfer, and optical WPT [42].

WPT methods, such as inductive coupling and magnetic resonance coupling, are effective over short distances, as seen in wireless charging pads for consumer electronics. However, these techniques are constrained by their limited range [43, 44]. RF-based power transfer can provide longer range solutions but also has its drawbacks, as discussed in the introduction. It is prone to electromagnetic interference, which can affect sensitive electronic devices, and requires larger antennas, limiting its scalability [45]. These limitations have paved the way for optical WPT as a promising alternative for both small and long range, particularly for applications involving mobile equipment.

2.2.1 Optical Wireless Power Transmission

Optical WPT is a subset of WPT that uses light sources, such as lasers or light-emitting diodes, to transmit power through free space, which is then converted to electrical energy by PV receivers. As mentioned before, this approach offers unique advantages over other WPT methods. In addition to those already highlighted, one can add that it provides enhanced security and, more importantly, the ability to transmit power over longer distances [46]. This is because optical WPT is less subject to diffraction, as it operates at shorter wavelengths compared to microwaves WPT for example. This makes it ideal for applications such as powering remote sensors, unmanned aerial vehicles (UAVs), and autonomous systems operating in hazardous or remote environments, such as underwater or on the lunar surface as it is the case in this thesis [47, 48].

Various optical WPT methods have been explored to optimize power transmission efficiency, safety, and practicality, particularly for low-intensity and short-distance applications. Techniques such as optical beamforming [49], distributed laser charging [50], adaptive distributed laser charging [51], and simultaneous lightwave information and power transfer [52] have enabled this precision, safety, and efficiency of power delivery enhancement. They are well

suited for charging consumer electronics and powering devices in line-of-sight conditions.

Despite these advancements, challenges remain in achieving long-range, high-power transmission suitable for both terrestrial and space applications. High-intensity OPB has been identified as a promising solution to these challenges and is the particular subject that will be treated in this thesis and in the following subsection of this chapter. In high-intensity OPB systems, high-power lasers are employed to convert electrical power into monochromatic light beams directed towards distant PV receivers. This method should enable the transmission of substantial amounts of power over significant distances, which differentiates it from previous methods, making it suitable for "larger-scale" applications such as powering UAVs, satellites, as well as lunar habitats [11].

It is important to clarify now the designations that will be used in this thesis. PV receiver and laser power converter (LPC) will be used, but they don't represent exactly the same thing. A LPC is specifically designed to convert laser energy with a defined wavelength, making it more efficient for OPB. In contrast, a PV receiver is a more general term for a device that converts light into electricity, but is not necessarily optimized for a specific wavelength. On the other hand, it's also worth mentioning that "high-intensity" will sometimes be omitted for the sake of brevity, but the reader should keep in mind that this thesis deals with high-intensity OPB systems. Lastly, since OPB encompasses laser power beaming, the term OPB will be used to remain more general.

2.2.2 High Intensity Optical Power Beaming

High-intensity OPB, the transmission of high-power via light over long free space distance, was conceptually established in the 1980s when researchers began exploring the use of lasers for various space applications. Initial proposals included utilizing lasers to launch rockets, power satellites, and facilitate energy transmission in space [53–55]. These early ideas showed the potential of laser-based energy transfer but also highlighted the need for efficient photovoltaic receivers to convert laser light into electrical power effectively.

A major advancement came with the development of gallium arsenide photovoltaic cells optimized for specific laser wavelengths. In 1991, Olsen *et al.* achieved photovoltaic efficiencies up to 53% at an incident light intensity of $0.4 W/cm^2$ by matching the cell bandgap to 800–840nm diode lasers [56]. This significant improvement in conversion efficiency demonstrated the feasibility of OPB for practical applications. Further progress was reported by van Riesen *et al.*

in 2002, who measured photovoltaic efficiencies exceeding 50% at higher incident light intensities, maintaining 44% efficiency even at 42W/cm² [57]. Of course, this intensity couldn't be increased as much as desired because of the system's limited heat dissipation capabilities. Indeed, when the intensity increases, more heat is generated in the photovoltaic cell. This rise in temperature can damage the cell and reduce overall efficiency. Nevertheless, these results indicated that high-efficiency energy conversion could be sustained at power levels suitable for more demanding applications, strengthening confidence in the scalability of OPB systems.

In 1999, Kare *et al.* conducted a hardware demonstration, transmitting 850 nm infrared light over a distance of 10 meters using non-coherent laser diode arrays [58]. Although operational constraints, such as beam non-uniformity, impacted overall efficiency, their work elevated expectations for end-to-end system efficiencies to approximately 10%, a notable improvement from previous systems, which often achieved efficiencies well below 1%. Practical demonstrations in the early 2000s further validated the concept. In September 2003, NASA's Marshall Space Flight Center, successfully powered a small-scale aircraft using energy from a ground-based laser [59]. A custom Spectrolab thin film photovoltaic panel, consisting of triple junction Ga:In:P2 cells, was used for this experiment. By focusing an adjustable 1.5kW laser beam at 940 nm onto this panel with an approximate distance of 15 meters, sufficient power was generated to drive a DC motor and propel the aircraft in an indoor environment, and this, with a 17.7% efficiency of the loaded cells [59]. An important takeaway from this experiment for what will be discussed in this thesis is that the energy density of the laser was too high for individual cells to handle safely due to the risk of damage or reduced efficiency. Therefore, the laser beam had to be spread across an array of 24 cells to distribute the power more evenly, allowing each cell to handle a smaller portion of the beam's energy density. This approach necessitated a larger receiver, as more cells required more surface area.

Advancements continued with the Space Elevator Power Beaming Challenge, part of NASA's Centennial Challenges program. In 2009, LaserMotive won by demonstrating a laser powered climber ascending a 1 kilometer cable suspended from a helicopter [60]. This achievement highlighted, for the first time, the feasibility of transmitting kilowatts of power over long distances using laser beams. Following this success, LaserMotive (later PowerLight Technologies) showcased several significant demonstrations. In 2012, they powered a Lockheed Martin Stalker UAV in flight tests [61]. The drone stayed airborne for 48 hours in a wind tunnel, and outdoor tests showed it could recharge its battery during flight. These results highlighted the potential of OPB to improve endurance and flexibility of unmanned systems.

In 2014, researchers from Beijing University of Technology developed a laser power transmission system with a wavelength of 793 nm and an output power of 24 W. Their experiment demonstrated an overall electric-to-electric efficiency of 11.6% over a 100 m distance [62]. This was followed by work carried out by the Japan Aerospace Exploration Agency (JAXA) in 2016, which achieved 74.7 W of electrical output from a 350 W laser over 200 m, demonstrating significant progress in OPB systems precision and power at mid-range distances. [63]. In 2017, a team from the China Electronics Technology Group Corporation developed an OPB system using an 808 nm laser with an output power of 100 W, reaching a laser-to-electricity conversion efficiency exceeding 28% at a 50 meters transmission distance. In 2019, the U.S. Naval Laboratory conducted experiments at the Naval Experimental Base in Maryland, successfully transmitting 2 kW of laser power over 325 m, receiving approximately 400 W of electrical power at the receiving end [64]. The reader should keep in mind that these orders of magnitude were for terrestrial experiments, where atmospheric effects can play a critical role, mostly over long distances. In space, better results are therefore expected.

In recent years, mainstream industry players have begun to explore high-intensity OPB. Ericsson, in collaboration with PowerLight Technologies, announced in October 2021 the successful demonstration of a wirelessly powered 5G radio base station using laser-based optical beaming [65]. The system safely transmitted hundreds of watts over distances of hundreds of meters, indicating the potential for high-intensity OPB to supplement or replace traditional power infrastructure in telecommunications. Recent work by the U.S. Naval Research Laboratory has also expanded high-intensity OPB capabilities to space-based applications. The Space Wireless Energy Link (SWELL) experiment, launched in 2023, operated in orbit for over 100 days, transmitting 1.5 W of laser power over 1.45 m with an end-to-end efficiency of 11%. To date, it's the longest, most powerful, and most efficient demonstration in orbit [66].

Laser Power Emitter

Over the past decade, significant advancements have been made in improving high-power laser systems for OPB applications. Initial efforts focused on diode lasers due to their compactness, high-efficiency and cost effectiveness, but they were limited by poor beam uniformity, low spectral purity and high divergence [67]. This type of laser is an optoelectronic device that uses a semiconductor as the amplifying medium to generate coherent light through stimulated emission. To overcome the limitations of diode lasers, researchers explored alternative laser architectures. Diode-pumped alkali-vapor lasers were introduced, delivering 2.5 kW of fiber-coupled power with a spectral concentration of 90%, thereby improving the spectral

purity essential for OPB [68]. Concurrently, Huang *et al.* reported an efficiency of 44% at an output of 4 kW for high-brightness diode lasers, demonstrating that diode lasers could still be optimized for high-power applications [69].

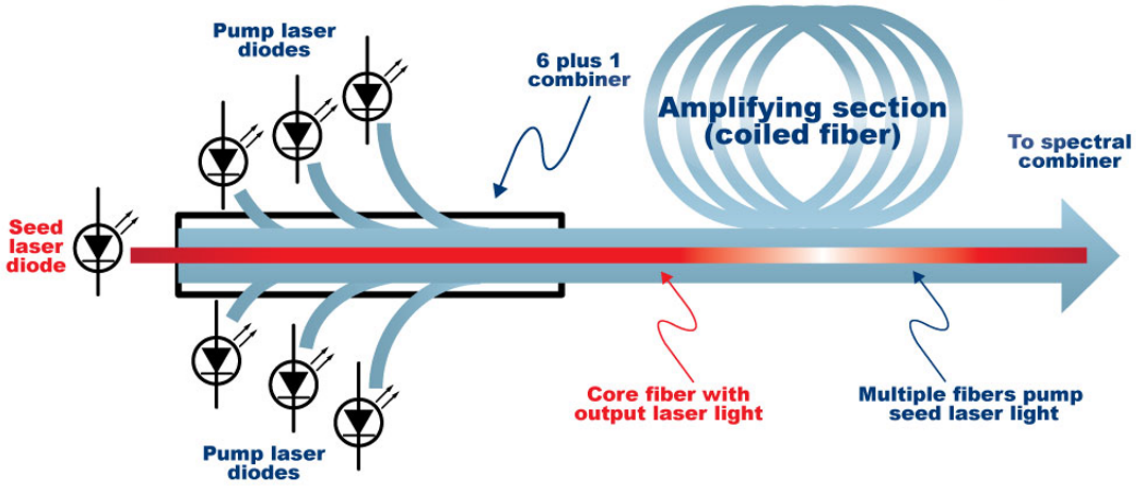

Figure 2.2 Diagram of a doped fiber laser [2].

Considerable progress has also been made in fiber laser technology. The rapid development of rare-earth-doped optical fibers has led to high-power fiber lasers with output powers reaching several kilowatts from a single fiber and with high beam quality. Fiber lasers are lasers in which the amplifying medium is an optical fiber doped with rare-earth ions such as ytterbium, erbium, or thulium. These lasers are pumped by diode lasers, as illustrated in Figure 2.2, and optical gain is generated within the fiber through interactions between the pump light and the dopant ions. Ytterbium-doped fiber lasers, in particular, offer high energy efficiency, excellent beam quality, robust power scalability, and minimal thermal effects, making them ideal for OPB applications. For instance, a 1.33 kW ytterbium fiber laser operating at 1018 nm with a beam quality factor M^2 less than 1.1 was reported by Platonov *et al.* [70]. Today, high power ytterbium fiber lasers are commercially available. Operating at wavelengths around 1007-1070 nm, they are well-suited to the absorption characteristics of InGaAs LPCs and offer excellent power stability and high efficiency, making them ideal for long-range, high-power transmission applications [71].

In terms of modeling, a high-power diode laser is often described using a far-field diffraction model, which characterizes the behavior of the beam at a certain distance from the source [72]. This approach is particularly useful as it simplifies modeling and accounts for the large beam

divergence angle typically seen in high-power diode lasers. On the other hand, fiber lasers, especially those in single-mode fibers, are effectively modeled using Gaussian beam theory, which provides solutions to the paraxial wave equation and describes the propagation of beams with Gaussian intensity profiles both in free space and within fiber optics. In single-mode optical fibers, the core is designed to support only the fundamental mode of light propagation, which has an intensity profile closely resembling a Gaussian distribution [73].

Laser Power Receiver

As already mentioned, LPCs, designed specifically to convert monochromatic light with high efficiency, often use silicon or gallium arsenide (GaAs) as the light-absorbing materials. The choice of laser wavelength for LPCs design has always been influenced by the terrestrial atmospheric window to ensure optimal transmission by reducing atmospheric losses. Nowadays, due to well-established production expertise and reliability, GaAs remains a mainstay for LPCs, with recent devices achieving power conversion efficiency (PCE) of 68.9% at 858 nm and 74.7% at 808 nm [74–77].

Efforts to enhance light absorption have included substituting GaAs lattice atoms with indium, allowing for precise bandgap tuning to match near-infrared wavelengths. Recently, InGaAs based LPCs achieved a PCE of 50.8% under a 1064 nm laser and under high-intensity illumination, as reported in a 2020 study [78]. This wavelength is particularly well suited for Ytterbium fiber lasers, and enables high end-to-end conversion efficiencies. Continued research aims to push efficiency beyond 50.8% by optimizing layer structures and reducing non-radiative recombination losses [78].

2.3 Research Gaps

Overall, high-intensity OPB technology has primarily advanced through government led research efforts, including those by NASA, DARPA, and JAXA, as well as through collaborations with emerging companies like Powerlight Technologies. When analyzing previous work and experimental reports, we can notice that none of these studies explained the theoretical background of these experiments or any kind of optimization. This can be explained by several factors: firstly, companies and agencies often keep such information confidential for competitive reasons. Secondly, in recent years, the focus has often been on proving the viability of the technology in practical applications rather than conducting in depth theoretical

analysis and optimization. Finally, OPB is inherently complex, involving many topics such as optics, thermal effects, environmental interactions, and power conversion. Developing theoretical models that consider these interdependent factors is challenging, making them difficult to generalize and, consequently, less likely to be published. Table 2.1 illustrates the main research topics related to OPB and identifies recent relevant studies, as well as the themes covered in this thesis.

Table 2.1 Overview of articles relevant to high intensity OPB.

References	**Tx-Rx components efficiency**	**Terrestrial atmospheric attenuation**	**Terrestrial weather/ water/sandstorms attenuation**	**Tx thermal management**	**Rx thermal management**	**Beam alignment**	**Optical optimization**	**Natural LLD attenuation**	**Artificial LLD attenuation**	**OPB performance evaluation**
Sprangle *et al.* [79]		X								
Gou *et al.* [80]	X									
Reich *et al.* [81]			X							
Su *et al.* [82]		X								
Long *et al.* [83]	X									
Kumar *et al.* [84]							X			X
Naidoo *et al.* [85]	X									
Ghassemlooy *et al.* [86]			X							X
Ando *et al.* [87]				X	X					
Cuco *et al.* [88]				X	X		X			
Fernandes *et al.* [89]						X				
Lolachi *et al.* [90]									X	
This thesis					X	X	X	X		X

In general, significant research gaps remain, both in improving the efficiency of individual components and in effectively integrating them to optimize the overall system performance. This thesis seeks to address this integration challenge, particularly within the context of a lunar space scenario. Specifically, it aims to first assess if natural LLD has an impact on power transmission, and then to optimize the OPB system's performance to efficiently harvest energy over long distances on the Moon, while adhering to SWaP constraints, considering optical, thermal and environmental aspects.

To achieve this, we will conduct a theoretical and simulation based study that will initially

assess transmission losses due to LLD using Mie theory and evaluate energy harvesting performance with a LoS FSO link model. The model will then be enhanced by employing Gaussian beam theory to assess energy harvesting performance and optimize beam propagation, while the T-matrix method will be used to model attenuation caused by LLD. After that, thermal management constraints will be integrated into the model, taking into account the limitations of radiative cooling in the lunar environment. Finally, simulations will be performed for both ground-to-ground and orbit-to-ground scenarios, optimizing key design parameters such as transmitter and receiver aperture sizes, and using up-to-date realistic data to assess the performance of OPB for lunar missions.

CHAPTER 3 OPB in the Lunar Environment : Initial Approach

This chapter first presents our initial approach, which was presented at the IEEE Aerospace conference 2024, and is derived from our previously published **peer-reviewed** conference paper [16]. The shortcomings of this approach, as well as the necessary improvements, will be discussed, with further developments addressed in the next chapter.

Our initial approach assesses transmission losses due to LLD using Mie theory and evaluates the energy harvesting performance using a LoS FSO link model under both illuminated and dark conditions. It will be presented in the following section, beginning with the system model section to maintain conciseness and avoid redundancy, and including minor modifications to ensure consistency throughout this thesis.

3.1 Impact of Lunar Dust on Free Space Optical (FSO) Energy Harvesting

3.1.1 System model

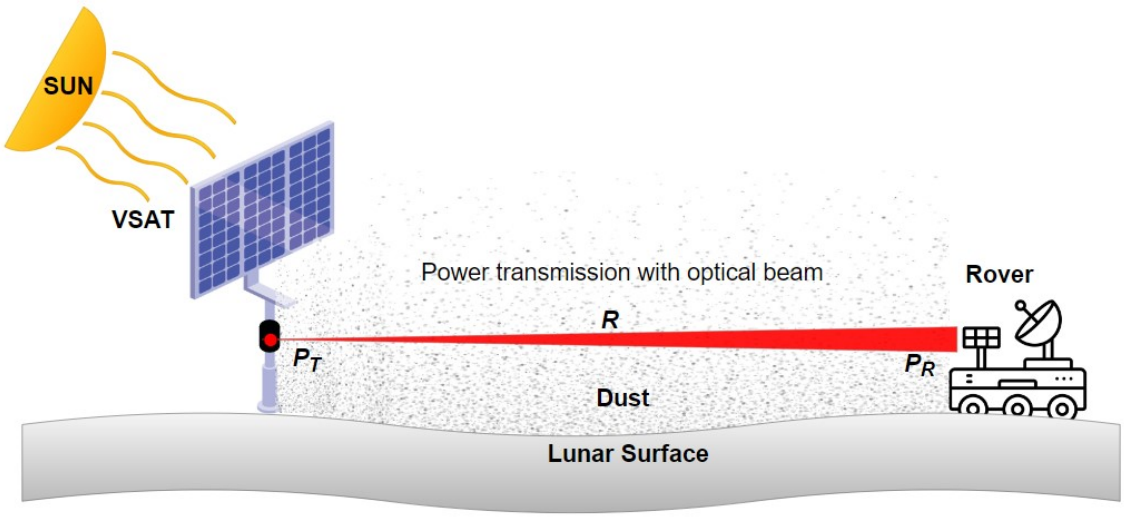

Figure 3.1 Lunar surface optical power transmission system.

Our proposed system model, as demonstrated in Figure 3.1, consists of a transmitter (e.g., lunar vertical solar array technology (VSAT) or nuclear fission reactors [7]) and a receiver unit (e.g., Amalia or Polaris rovers [91]) based on the lunar surface. In the proposed system, the receiver unit employs energy harvesting techniques from a remote laser diode featuring

adaptive beam divergence, as delineated in [92]. This mechanism ensures the maintenance of an optimal spot diameter as the separation between the transmitter and receiver increases. The system is designed to be self-sustaining and aims to utilize wavelength-dependent conversion efficiencies that are as high as feasible. It is imperative to note that the efficiency metrics must be consistent across the same wavelengths (λ) for both the transmitting and receiving units, as indicated in [93]. Consequently, meticulous selection of system components is essential for optimal performance.

Energy Harvesting and Beam Propagation Model

The harvested power of a free space LoS optical link in a far-field approximation is expressed as follows [94]

$$P_h = P_t \left(\frac{\lambda}{4\pi R}\right)^2 \eta_{e/o}(\lambda)\eta_h(\lambda)L_t(\psi_t)G_t L_r(\psi_r)G_r L_e L_s L_c, \tag{3.1}$$

where P_h is the harvested electrical power, P_t is the transmitted electrical power, $\eta_{e/o}(\lambda)$ and $\eta_h(\lambda)$ are the wavelength-dependent electrical-to-optical power conversion efficiency (PCE) and energy harvesting conversion efficiency (EHCE), respectively. In addition, $L_t(\psi_t)$ is the radial angle-dependent misalignment loss factor at the transmitter, G_t is the transmitter gain, $L_r(\psi_r)$ denotes the radial angle-dependent misalignment loss factor at the receiver, G_r is the receiver gain, L_e is the atmospheric extinction/attenuation loss, L_s is the scintillation loss, and L_c represents the fiber coupling loss.

For our lunar FSO energy harvesting scenario, we consider $L_e = L_s = L_c = 1$, as done in [94]. Moreover, in order to account for the influence of lunar dust on optical transmission, this study introduces the loss factor L_{dust}, which quantifies the loss attributed to the scattering and absorption effects of lunar dust. Therefore, the received power of the free space lunar LoS optical link becomes

$$P_h = P_t \left(\frac{\lambda}{4\pi R}\right)^2 \eta_{e/o}(\lambda)\eta_h(\lambda)L_t(\psi_t)G_t L_r(\psi_r)G_r L_{dust}. \tag{3.2}$$

The transmitter and receiver gains can be approximated as [95]

$$G_t \approx \left(\frac{\pi d_t}{\lambda}\right)^2, \tag{3.3}$$

$$G_r \approx \left(\frac{\pi d_r}{\lambda}\right)^2, \tag{3.4}$$

where d_t and d_r are the aperture diameter of the transmitter and receiver, respectively.

The loss factor due to misalignment at both the transmitter and receiver can be calculated as follows [95]

$$L_t = \exp(-G_t \psi_t^2), \tag{3.5}$$

$$L_r = \exp(-G_r \psi_r^2), \tag{3.6}$$

where ψ_t and ψ_r are the transmitter's and receiver's radial misalignment error angle. Its model is based on the methodology presented in [72]. In this work, ψ_t and ψ_r follow a Rayleigh distribution for both the transmitter and receiver. This comes from the fact that the radial misalignment error is derived from the independent elevation and azimuth misalignment angles, which are each modeled as zero-mean Gaussian distributions. The details of the methodology can be found in the appendices.

The adaptive beam divergence angle θ varies in relation to the spot radius and distance R using the small-angle approximation [96]

$$\theta \text{ [rad]} = \frac{\text{Spot radius at the receiver [m]}}{R \text{ [m]}}. \tag{3.7}$$

In addition, the appropriate transmitter aperture diameter, d_t (which will be referred to as the double of the beam waist in the next chapter), can be determined by

$$d_t \approx \frac{1.22\lambda}{\theta}, \tag{3.8}$$

based on Fraunhofer diffraction and the Rayleigh criterion for the diffraction limit, where λ is the laser wavelength [97]. In our study, we adjust the far-field beam divergence angle to guarantee that the diameter of the spot at the receiver perfectly matches the dimensions of the receiving unit. Consequently, we select the diameter of the transmitter aperture to align with the necessary divergence angle.

Lunar Dust Attenuation Model

The presence of lunar dust adversely affects laser transmission through mechanisms of scattering and absorption. The magnitude of this impact depends on variables such as the wavelength of the laser and specific lunar dust characteristics. This study introduces a lunar dust attenuation model, built upon realistic data collected from existing literature. More precisely, the model employs Mie theory to simulate the scattering and absorption characteristics of lunar dust particles [98].

Mie theory Lunar dust particles are angular and irregular in shape [99]. However, for the application of Mie theory, a spherical approximation is adopted. This approximation is particularly useful as it significantly simplifies the equations and associated calculations, making the analysis more manageable. Although this simplification may not capture all the complex details of the particles actual shapes, it provides a good initial approach for understanding their absorption and scattering properties.

In Mie theory, the scattering and absorption properties of a spherical particle are described by a set of complex mathematical equations that take into account the size and refractive index of the particle, as well as the wavelength of the incident light. Unlike Rayleigh scattering, which is applicable for particles much smaller than the wavelength of light, Mie theory is applicable for particles of any size, including those comparable to or larger than the wavelength. The theory provides a way to calculate the scattering and absorption cross-sections, which are critical for understanding how much light is scattered (redirected in various directions) or absorbed (converted into heat or other forms of energy within the particle) by the particle. These cross-sections provide a measure of the effective area that a particle presents for scattering or absorbing light, rather than the actual physical size of the particle [100].

The Mie theory is used to calculate the extinction cross-section C_{ext} of the particle as [98]

$$C_{ext} = \frac{2\pi}{k^2} \sum_{n=1}^{\infty} (2n+1) Re(a_n + b_n), \tag{3.9}$$

$$C_{ext} = C_{abs} + C_{scat}. \tag{3.10}$$

In this context, C_{ext} represents the sum of the absorption and scattering cross-sections. $k = \frac{2\pi}{\lambda} n'_{medium}$ denotes the wavenumber in the medium, where n'_{medium} is the refractive index

of the medium. In this case, the medium is the vacuum, so $n'_{medium} = 1$. Additionally, a_n and b_n are the Mie expansion coefficients.

The Mie expansion coefficients a_n and b_n are defined as follows [98]

$$a_n = \frac{m\psi_n(mx)\psi'_n(x) - \psi_n(x)\psi'_n(mx)}{m\psi_n(mx)\xi'_n(x) - \xi_n(x)\psi'_n(mx)}, \tag{3.11}$$

$$b_n = \frac{\psi_n(mx)\psi'_n(x) - m\psi_n(x)\psi'_n(mx)}{\psi_n(mx)\xi'_n(x) - m\xi_n(x)\psi'_n(mx)}, \tag{3.12}$$

where, $\psi_n(x)$ and $\psi'_n(x)$ refer to the Riccati-Bessel function of the first kind and its derivative, respectively. On the other hand, $\xi_n(x)$ and $\xi'_n(x)$ denote the Riccati-Bessel function of the third kind (also known as the spherical Hankel function of the first kind) and its derivative, respectively. Additionally, $m = \frac{n'_{particle}}{n'_{medium}}$ represents the relative refractive index of the particle to the surrounding medium, and $x = kr$ is the size parameter, where r is the radius of the spherical particle.

In the equations above, $\psi_n(x)$ and $\xi_n(x)$ are calculated as follows [98]

$$\psi_n(x) = \sqrt{\frac{\pi x}{2}} J_{n+\frac{1}{2}}(x), \tag{3.13}$$

$$\xi_n(x) = \sqrt{\frac{\pi x}{2}} H^{(1)}_{n+\frac{1}{2}}(x), \tag{3.14}$$

where $J_{n+\frac{1}{2}}(x)$ represents the Bessel function of the first kind, while $H^{(1)}_{n+\frac{1}{2}}(x)$ denotes the Hankel function of the first kind.

Of course, in order to numerically evaluate the infinite sums, we truncate the series at a sufficiently large number of terms, M, to ensure that the neglected terms have a minimal impact on the final result. Based on [98], this number is calculated as

$$M = \text{ceil}\left(\text{conv} \times \left(x + 4x^{1/3} + 2\right)\right), \tag{3.15}$$

where x is the size parameter, and conv is the convergence factor (by default set to 1), which can be adjusted to meet convergence. The results obtained in this subsection are for a single particle. In the following subsection, we will generalize this for a set of particles.

Radiative Transfer Theory While terrestrial applications of FSO technology are often hindered by atmospheric conditions such as fog, rain, or snow [101], the lunar environment introduces its own challenge in the form of LLD particles near the surface. With the results provided by Mie's theory, which has been used to quantify the extinction properties of a single particle, we will now extend the results using radiative transfer theory to quantify the attenuation of a whole "cloud" of particles. The Bouguer-Beer-Lambert law can be derived from the radiative transfer theory and will be performed in the next chapter, as the spherical case is a specific case of the following chapter.

Using the Bouguer-Beer-Lambert law, the attenuation coefficient, α_{ext}, which is an integrated measure of absorption and scattering in the medium [102] is defined as

$$\alpha_{ext} = n_0(h) \times C_{ext}, \tag{3.16}$$

where n_0 is the number density of particles in $particles/\mathrm{m}^3$ and C_{ext} is the particle extinction cross-section in m^2. The transmission efficiency, define as a loss factor L_{dust}, in this paper, for a path length R is given by [102]

$$L_{dust} = e^{-\alpha_{ext}R}. \tag{3.17}$$

It is important to note that for the derivation of this formula, the particle density is assumed to be uniform along the transmission path. Also, in general, the attenuation coefficient α_{ext} is often used to describe the loss in the electromagnetic field, but in this specific case, it refers to a power loss.

Lunar Dust Application In order to apply this model, data specific to the properties of lunar dust, such as particle size distribution, density, and refractive index are required. The particle size distributions of lunar dust from the Apollo 11 and 17 missions were analyzed using SEM techniques and quantified using equivalent circular diameters, calculated as $2\sqrt{\frac{\text{Particle Surface Area}}{\pi}}$ to facilitate a shape-independent comparison. The particle size distributions ranged from 20 μm to 20 nm and followed a log-normal pattern, with peak modes between 100 and 300 nm [99, 103].

In order to determine the density distribution of the dust grains at various heights above the lunar surface, the results presented in [1] are taken. According to this source, the number

density of charged dust grains in the near-surface layer over the illuminated part of the Moon is on the order of $10^3\,\mathrm{cm}^{-3}$. This high density is attributed to the large amount of photoelectrons, including those emitted from the surfaces of flying dust grains. The distribution of density of lunar dust particles by near-surface height in illuminated areas is shown in Figure 3.2, which is reproduced from [1].

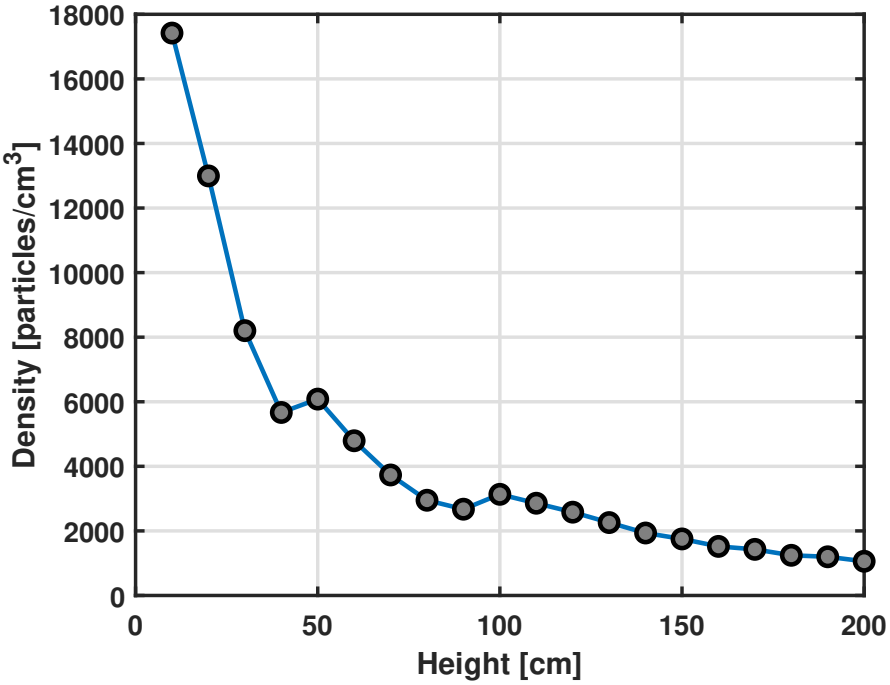

Figure 3.2 Lunar dust particle density as a function of the near-surface height over the illuminated part of the Moon from [1].

The distribution is determined using reference parameters specified in [1]: the subsolar angle is $\theta = 77°$, the density of photoelectrons emitted immediately at the lunar surface is $N_0 = 1.9 \times 10^5\,\mathrm{cm}^{-3}$, and the thermal energy of the electrons is $T_e = 0.1\,\mathrm{eV}$. A rather large value of θ was taken because the corresponding latitude region of interest is the polar regions of the Moon.

On the other hand, over the dark part of the Moon the photoelectrons are expected to be absent [1, 19]. The lunar surface is charged negatively under the influence of the solar wind electrons and the plasma of the terrestrial magnetosphere tail. Therefore, in those regions, the dust particle density is significantly lower, ranging between 10^{-2} and 10^{-1} cm^{-3} for dust particles of sizes $a \approx 100\,\mathrm{nm}$ [1]. As a consequence, for the dark regions of the Moon, we

postulate that the particle density follows the same distribution as in illuminated areas, albeit scaled by a factor of 10^{-4}.

Concerning the complex refractive index of lunar dust, it is expressed as

$$\tilde{n} = n^* + ik^*,$$

where the real part n^* describes the phase velocity of light as it propagates through the lunar dust medium. This real component primarily governs optical effects such as refraction. In contrast, the imaginary part k^* quantifies the absorption of electromagnetic waves as they travel through the medium, indicating how much light is absorbed.

In the current literature, the real part of the refractive index for lunar dust is typically reported to be between 1.58 and 1.78 [104, 105]. However, obtaining accurate values for the imaginary part k^* is more complex. For the purposes of this study, we approximate the refractive index by assuming that lunar dust particles are mostly composed of silicates. As a result, we base our refractive index values on those of 'astronomical silicate' [106]. This approach simplifies the modeling process, considering the variable composition of lunar dust and is a justified approximation as studies of lunar geology indicated that the regolith is rich in silicate minerals. Furthermore, the optical properties of astronomical silicates are well-documented, making them a suitable approximation for lunar dust in this context.

To determine the complex refractive index, we use the dielectric function, represented by the real part ϵ_1 and the imaginary part ϵ_2. Specifically, ϵ_1, represents the material's ability to store electrical energy, while ϵ_2 indicates the material's capacity to dissipate energy as heat, reflecting dielectric losses. Using these dielectric function values from the literature for a specified wavelength [106], we calculate the real and imaginary parts of the complex refractive index with the following equations

$$n^*(\lambda) = \sqrt{\frac{\sqrt{\epsilon_1^2 + \epsilon_2^2} + \epsilon_1}{2}}, \tag{3.18}$$

$$k^*(\lambda) = \sqrt{\frac{\sqrt{\epsilon_1^2 + \epsilon_2^2} - \epsilon_1}{2}}. \tag{3.19}$$

These expressions allow us to model the wavelength-dependent refractive index of lunar dust, using the dielectric properties of astronomical silicate.

3.1.2 Attenuation and Performance Evaluation

The impact of lunar dust on the system's performance is quantitatively assessed through simulation studies. Prior to calculating the average harvested power, the cross-sectional area of the lunar dust particles under consideration is determined. Subsequently, the attenuation coefficient and the loss factor L_{dust} are evaluated for two distinct lunar scenarios: the illuminated and the dark regions. The average harvested power is then computed for both scenarios. Statistical analyses of independent elevation and azimuth misalignment error angles for both the receiver and transmitter are conducted using Monte Carlo simulations, with pointing resolution parameters outlined in Table 3.1.

Simulation Parameters

As mentioned previously, the grain size of lunar dust adheres to a log-normal distribution with peak modes ranging between 100 and 300 nm. Upon an analysis of the distribution [107], this study opts for an average effective diameter of 150 nm for the simulation. On the other hand, based on the dielectric function data provided in [106] and the formulas (3.18) and (3.19), the complex refractive index for a wavelength of 1064 nm is determined to be $n = 1.733 + i0.05$. The value of the real part of the refractive index is within the range of values given in the literature for lunar dust, which solidifies the relevance of the chosen approach. Given the lunar space conditions, the refractive index of the medium surrounding the particle is set to 1.0.

In our analysis, the LoS distance range under consideration extends up to 100 km. Under this condition, the transmitter diameter is on the order of about ten centimeters at most. The judicious selection of the laser diode type is imperative for the system's efficacy. The operating wavelength must not only facilitate adequate energy harvesting but also be compatible with space mission requirements. In light of these considerations and the findings of [108], we employ a Nd: YVO4 1064 nm laser source with a PCE of 51% [109]. The transmitted energy is then harvested using solar cells matching the laser wavelength. Given that laser diodes predominantly operate in the infrared band, specifically at 1064 nm, solar cells are well-suited for FSO based energy harvesting [110]. Among the various types of solar cells capable of converting optical energy to electrical energy, InGaAsP-based solar cells, which offer a conversion efficiency of 26.4%, are compatible with our proposed system operating at a laser wavelength of 1064 nm [72, 111]. Concerning, the misalignment error, as a zero-mean Gaussian distributions for the misalignment angle was used, only the pointing resolution need

to be specified. For this one, a reasonable value of 2 µrad was taken based on [112].

Finally, various transmit powers P_t between 1 W and 10 kW are considered in our simulations. We then fix two constraints based on the Polaris rover, specifically its energy requirement of 250 W and the receiver size, which corresponds to an aperture area of 3.6 m^2, as referenced in [91], resulting in an aperture diameter of approximately 2.1 m. The summary of parameters is provided in Table 3.1.

Table 3.1 Summary of Parameters: Initial Approach.

Parameter	**Value**
Transmission Range	up to 100 km
Transmitted Power	up to 10 kW
Particle Average Effective Diameter	150 nm
Particles Density & Height	See Figure 3.2
Particle Complex Refractive Index	$1.733 + i0.05$
Medium Refractive Index	1.0
Laser Wavelength (λ)	1064 nm [95]
Laser Diode PCE (%)	51% [109]
Beam Divergence Angle (θ)	Adaptive
Polaris Rover Receiver Aperture Diameter (d_r)	2.1 m
Pointing Resolution	2 µrad [112]
EHCE (%)	26.4% [113]
Polaris Rover Power Requirement (W)	250 W [91]

Results and Discussions

Simulations were carried out to assess the influence of lunar dust on the average harvested power P_h by the Polaris rover, considering varying transmit powers and distances R within our proposed system model. Additionally, the study identifies the minimum transmit power necessary to fulfill the energy requirements of the rover at varying distances from the transmitting source.

Firstly, it should be reminded that an effective mean diameter of 150 nm was selected for simulations. However, the attenuation coefficient can vary significantly depending on the chosen diameter value. Specifically, it appears to vary exponentially as the particle radius increases, as can be observed in Figure 3.3. The density, on the other hand, will not be considered constant throughout the simulations; rather, it will vary with height as described in Figure 3.2. As can be deduced from equation (3.16), it will have a linear impact on the

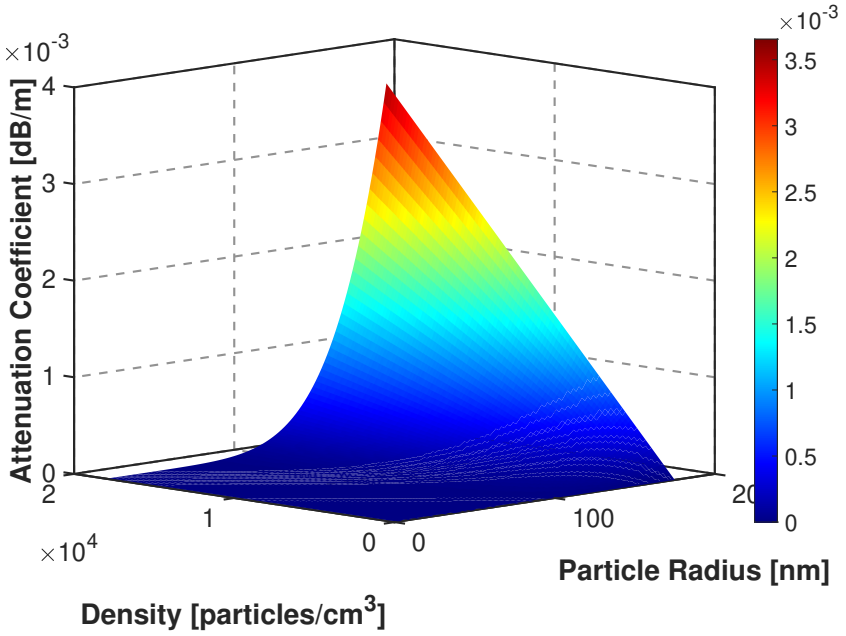

Figure 3.3 Attenuation coefficient as a function of density and particle radius.

attenuation coefficient, as shown in Figure 3.3.

The dust loss factor, which quantifies the laser transmission efficiency through a medium partially composed of lunar dust, was determined through simulations. These simulations employed the dust attenuation model outlined in the system model subsection, along with the data specified in the Table 3.1. This factor is presented as a function of both the transmission distance and the height above the lunar surface, for scenarios where the Moon is illuminated and where it is in darkness. The results are depicted in Figures 3.4 and 3.5.

In the scenario where the Moon is illuminated, it is observed that as the height above the lunar surface increases, the dust loss factor L_{dust}, also increases due to lower density at height. For these regions with a subsolar angle of 77°, we note that critical losses could be reached below a height of 1 meter, mostly for long transmission distances. This might suggest that installing the devices at a height greater than this, for that particular case, could greatly improve the system's overall efficiency. On the other hand, as the transmission distance increases, L_{dust} decreases, a result that aligns with expectations, as the laser light will experience greater attenuation over extended distances. In conclusion, Figure 3.4 reveals that below a certain critical height and beyond a specific critical distance, L_{dust} can lead to critical losses, and therefore have an impact on the transmission.

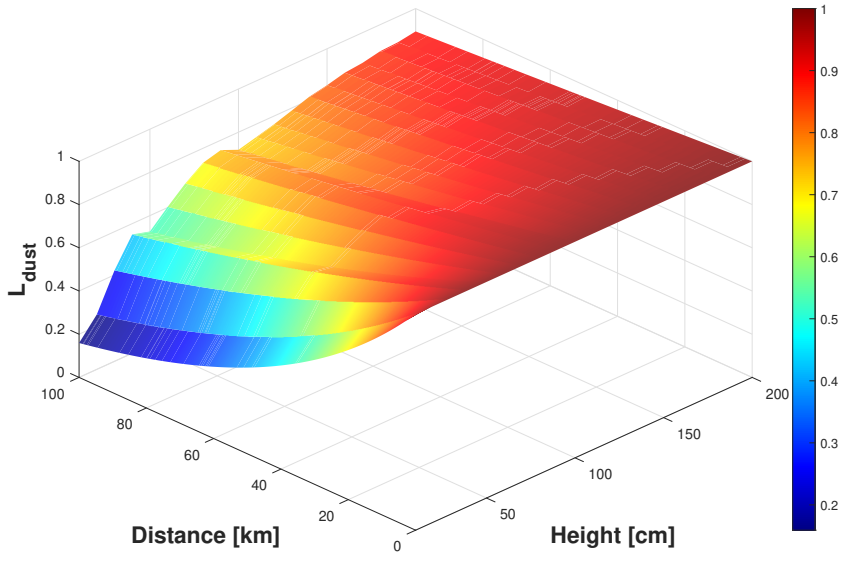

Figure 3.4 L_{dust} as a function of the transmission distance and the height above the lunar surface when the Moon is illuminated.

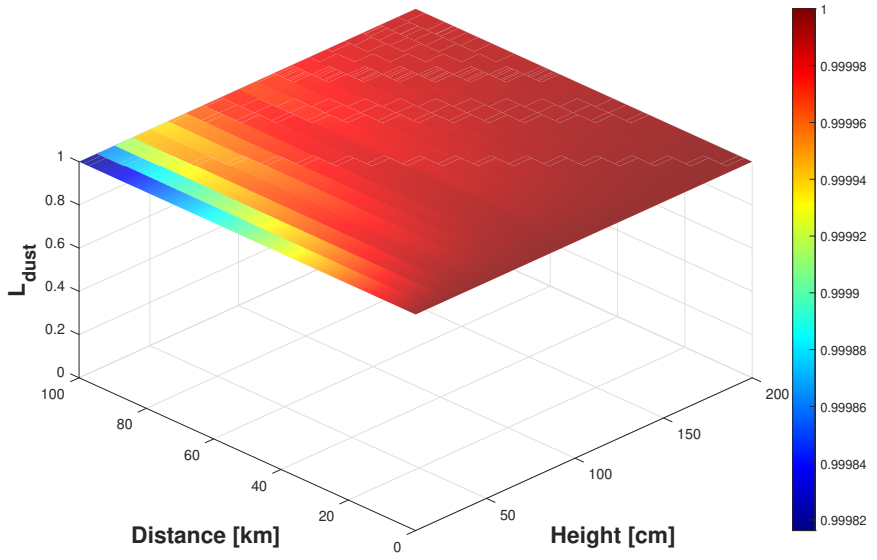

Figure 3.5 L_{dust} as a function of the transmission distance and the height above the lunar surface when the Moon is not illuminated.

In case where the Moon is in darkness, which can be the case in permanently shaded regions

or during the lunar nights, the situation differs as it can be observed in Figure 3.5. The variations of L_{dust} with respect to height and distance are negligible. In this case, the particles are not present in large enough numbers to be able to attenuate the beam.

Using the data presented in Table 3.1, the results of the average harvested energy as a function of transmitted power and transmission distance are shown in the Figure 3.6. Logically, the harvested power is greater over the considered ranges when the height above the lunar surface increases and when the transmission distance decreases. Both results are due to the lunar dust impact as the influence of R-squared simplifies in (3.2).

Considering the power requirements of the Polaris rover, which amount to 250 W, and taking into account a transmission distance of 20 km [91], we find that a minimum transmission power of 4210 W is required for a height of 20 cm above the ground, 3480 W for a height of 50 cm, and 2760 W for a height of 100 cm, to meet the rover needs. These results are consistent with the fact that at increased heights, the L_{dust} coefficient has a smaller influence, meaning that less power to transmit is needed.

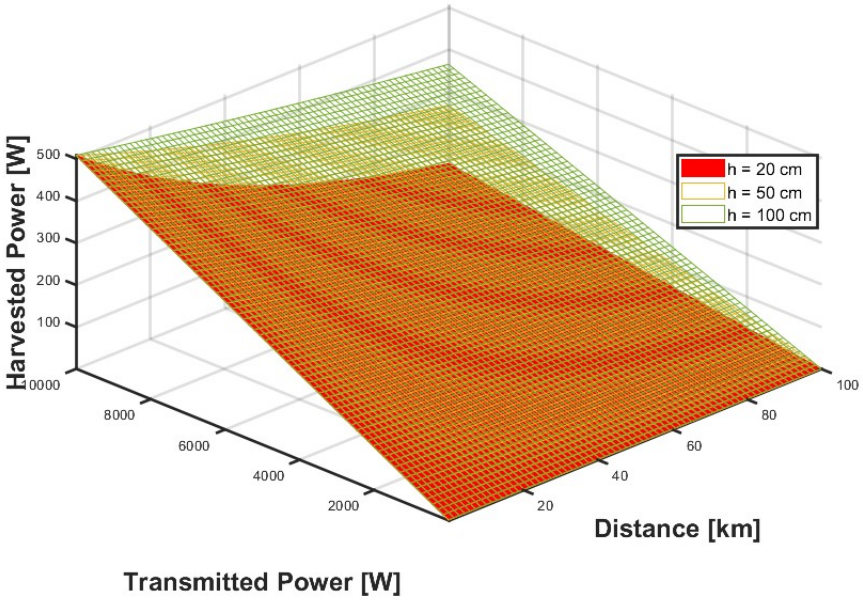

Figure 3.6 Average harvested power for various heights when the Moon is illuminated, with data from Table 3.1.

Regarding the scenario where the rover is in a dark region, Figure 3.5 illustrates that the influence of lunar dust is negligible. Therefore, height no longer matters and the 3 planes

coincide, as can be seen in Figure 3.7. Considering the L_{dust} coefficient equal to 1, we find for a distance of 20 km that a transmission power of 2050 W is sufficient to meet the 250 W requirement of the rover. This confirms the feasibility of the system, although high-power lasers are needed to provide sufficient energy, which is feasible nowadays.

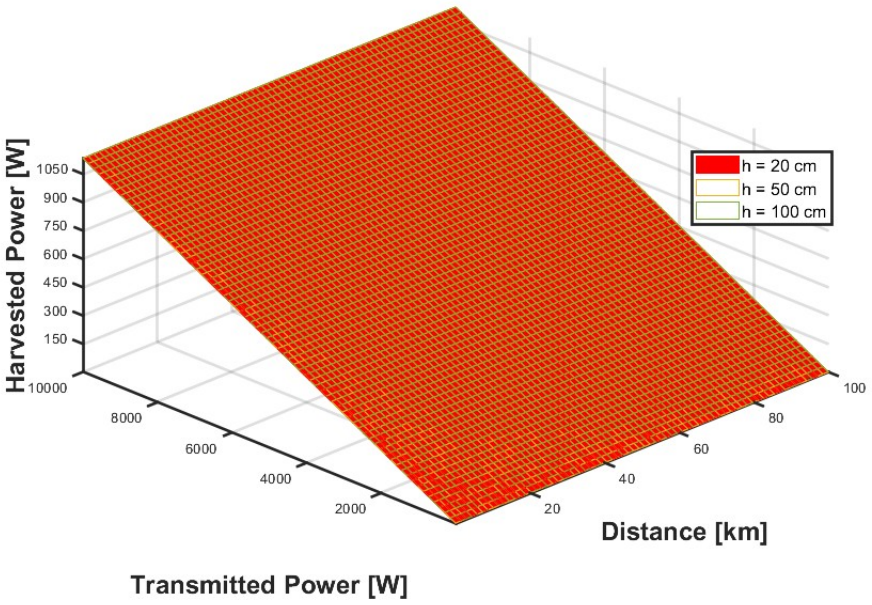

Figure 3.7 Average harvested power for various heights when the Moon is not illuminated, with data from Table 3.1.

3.1.3 Conclusions

This section has explored the impact of lunar dust on FSO energy harvesting on the lunar surface. Utilizing known mathematical models and numerical simulations, we assessed transmission losses and the performance of FSO energy harvesting under 2 different scenarios: illuminated and the dark regions. Our findings indicate that the choice of the height above the lunar surface and the transmission distance are key factors in evaluating both losses and energy harvesting efficiency. We have observed that in the darker regions of the Moon, the impact of lunar dust on transmission is negligible, which is not the case in the illuminated areas where the losses could be significant for near ground transmission. We therefore conclude that dark regions a better option for conducting FSO energy harvesting. We also assessed the power required to power a lunar rover, and concluded the feasibility of the system, even over long distances, by using high-power, multi-kilowatt lasers.

3.2 Shortcomings and Improvements

Although our study provides valuable insights, it does have certain shortcomings. This section aims to identify these shortcomings and propose improvements, which will therefore serve as a basis for the presentation of our final approach.

Energy Harvesting and Beam Propagation Model:

A concern that may arise when looking at equation (3.2) is that OPB can never be highly efficient due to the inverse square law. This principle states that quantities like electric field intensity diminish proportionally to the square of the distance [114]. However, this law specifically applies to isotropic point sources or cases where sources can be effectively approximated as points, meaning the law is valid in far-field conditions. While it is true that at sufficiently large distances this law can be applied to all practical sources (which is often the case in FSO system), OPB can operates within a range in the near-field regime before beam divergence occurs.

Similarly, we have assumed $d_t \approx \frac{1.22\lambda}{\theta}$ for beam propagation, following the diffraction limit typically used in imaging to resolve a spot. In imaging, this approach defines the Airy disk and the location of the first intensity minimum, with θ representing the beam divergence angle, which is often small enough to apply the small-angle approximation, and d_t referring to the transmitter diameter. This model is generally employed to distinguish between two separate points based on the uncertainty principle applied to photons [115]. However, OPB can present several distinctions. First, it might not operate in the "far field", where Fraunhofer diffraction applies, as assumed by the prior formula. Second, the focus is more on capturing the maximum power, requiring an understanding of the beam profile's shape and extent. For this purpose, the next chapters will focus on Gaussian Beam theory to describe the energy harvesting model and the beam propagation. While the previous modelisation gives a good initial approach, Gaussian beam theory provides a more accurate representation of beam behavior in OPB systems. This approach allows us to account for critical aspects such as beam waist, beam divergence, Rayleigh range, and intensity distribution, even when operating outside the far-field region.

Overall, the approach previously used is valid in cases where the receiver is sufficiently distant from the source. In our case, this isn't necessarily the case, especially as we assume that the lunar dust attenuation model is based on a flat surface and constant density along the LoS,

which is typically valid when the receiver is close enough to the source. This "close enough" refers to the Rayleigh range, which will be defined in the next chapter.

Lunar Dust Attenuation Model:

One major limitation of Mie theory is its assumption that particles are perfect spheres, which fails to capture the irregular and angular shapes characteristic of lunar dust. This simplification can lead to inaccuracies in modeling the scattering and absorption of light by these particles. To overcome this shortcoming, the T-matrix method provides a more sophisticated approach by allowing for particles with arbitrary shapes, such as prolate spheroids that more closely resemble the actual form of lunar dust grains. By incorporating the particle's elongation into the calculations, the T-matrix method enhances the accuracy of predictions.

Simulation Parameters:

We need also to adopt slightly more realistic values, for example, reduce the transmission distance, use typical values for high-power lasers currently available commercially, and take a more realistic value for average particle size based on cross-section extinction. In addition, the particle size range selected must be representative of the particle sizes lifted and not of the samples described above, which are in fact samples taken from the ground. We will also remove the constraints of receiver size and receiver power requirement, for a more complete analysis. Instead, we will set the beam divergence angle on the basis of realistic values currently possible. With these changes, the LPC analysis becomes important and is the subject of the next subsection.

Laser Power Converter:

A major challenge when designing the LPC is to ensure that the receiver is thermally managed. Effective thermal management is a critical concern for the receiver, particularly when dealing with high power system, as it is the case with high-intensity OPB. As these systems operate, LPC convert only a portion of the incoming laser energy into electrical power, while the rest becomes waste heat. This excess of heat raises the temperature of the LPC, which can significantly reduce their efficiency due to the temperature dependence of their performance. If the cells become too hot, not only does their efficiency decline, but their operational lifespan may also be compromised.

To mitigate this issue, various cooling methods can be used to dissipate the waste heat.

However, these cooling solutions consume additional energy, which reduces the net power output of the system. Therefore, it's essential to utilize thermal management strategies that are both energy efficient and low in complexity to minimize their impact on overall system efficiency.

The link between temperature and PV efficiency is such that even small increases in temperature can significantly reduce efficiency. Trying to fix this by increasing the input laser power only makes things worse, as it creates more heat, which raises the temperature even more, leading to a cycle that reduces the system's performance. Thus, maintaining the PV cells below a certain critical temperature is generally advisable to prevent these issues. As we are dealing with high beam intensity, and in space conditions, where convection is not an option (radiative cooling being the only feasible method), thermal aspects dictate the design of receiver.

CHAPTER 4 OPB in the Lunar Environment : Final Approach

This Chapter presents our final approach. It evaluates transmission losses due to LLD using T-matrix method and quantitatively assesses the energy harvesting performance of the system using Gaussian beam theory, while ensuring a design that minimizes size and weight, thereby meeting SWaP constraints. This approach is derived from our journal paper, which is to be submitted, and will be presented in the following section, starting with the system model to ensure conciseness and avoid redundancy.

4.1 System Model

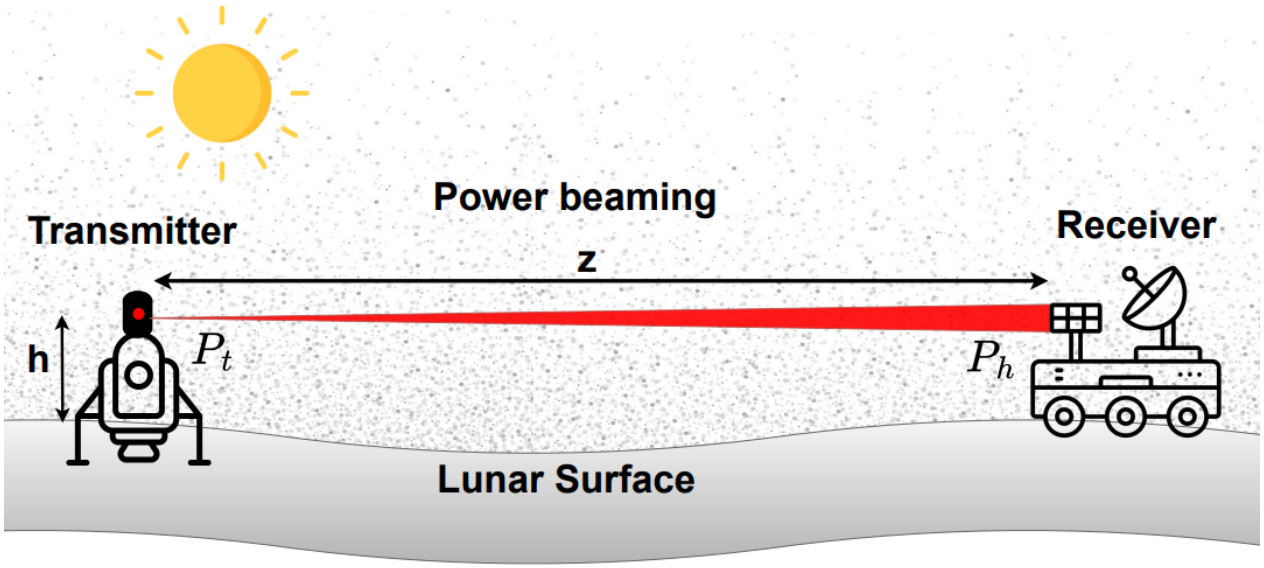

Figure 4.1 Ground-to-ground OPB on the lunar surface. Here, P_t denotes the transmitted power, P_r represents the received power, h is the height of the transmitter and receiver above the lunar surface, and z is the distance between the transmitter and receiver.

In our system model, we analyze a ground-to-ground power transmission, with a range spanning from a few meters to tens of kilometers, as illustrated in Figure 4.1. This approach primarily aims to supply energy to rovers, vehicles, sensors, and habitats on the lunar surface, as already mentioned. The system operates under the assumption of a clear LoS between the power transmitter and receiver located near the lunar pole, with this time, perfect beam alignment. It is important to note two key aspects of this scenario. First, the transmitter

and receiver are positioned at the same height h above the ground. Second, the system accounts for the presence of a dust cloud, where the particle density increases gradually as we approach the lunar surface.

4.1.1 Energy Harvesting and Beam Propagation Model

In this study, we aim to assess the amount of power that can be collected using realistic up-to-date data from the literature. The total harvested power, P_h, is calculated by integrating the irradiance over the receiver area, taking into consideration the efficiency of the conversion processes from the laser power output to the electrical power received, and is expressed as

$$P_h = \eta_{\text{Rx}} \cdot \eta_{\text{dust}}(h, z) \cdot \int_A I(r, z)\, dA, \tag{4.1}$$

where η_{Rx} denotes the efficiency of the receiver converting laser energy into electrical power, while $\eta_{\text{dust}}(h, z)$ accounts for the attenuation of laser intensity due to scattering and absorption by lunar dust particles. The irradiance $I(r, z)$ at a point on the receiver laser collector follows a 2D Gaussian distribution, given by [97]

$$I(r, z) = \frac{2P_t}{\pi w_R(z)^2} \cdot e^{-\frac{2r^2}{w_R(z)^2}}, \tag{4.2}$$

where P_t is the total transmitted power, r is the radial distance from the beam center, and $w_R(z)$ is the beam radius at the propagation distance z from its waist (narrowest point of focus). This beam radius represents the distance at which the optical intensity drops to $\frac{1}{e^2}$ (approximately 13.5%) of the peak intensity at the plane z [97]. These parameters describe the propagation of a Gaussian beam and are illustrated in Figure 4.2.

For a circular receiver laser collector with radius R, an analytical expression for the harvested power can be derived (see derivation in appendices) as follows

$$P_h = \eta_{\text{Rx}} \cdot \eta_{\text{dust}} \cdot P_t \cdot \left(1 - e^{-\frac{2R^2}{w_R(z)^2}}\right). \tag{4.3}$$

This equation relates the harvested power to the transmitted power P_t, the receiver radius R, and the beam radius $w_R(z)$ at the distance z from the beam waist. There is clearly a trade-off between maximizing the amount of collected power and minimizing the receiver size. Capturing all the transmitted power would theoretically require an infinitely large receiver radius, which is, of course, impractical as we aim to maintain a compact and efficient design.

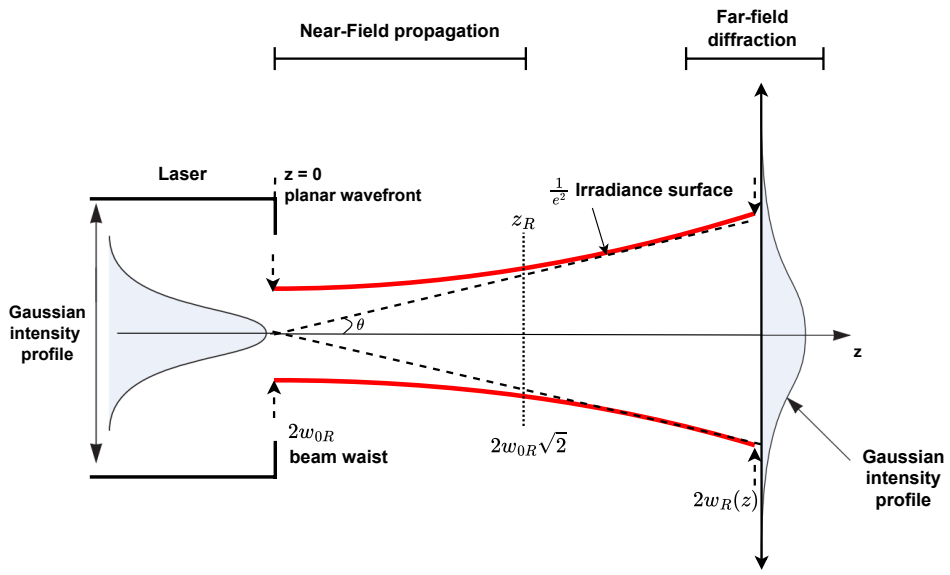

Figure 4.2 Parameters of real beam propagation, based on Gaussian theory.

To quantitatively assess the harvested power and facilitate the Gaussian beam analysis, we consider the receiver laser collector radius matching the laser beam radius at the receiver location, such that $R = w_R(z)$, meaning that the receiver is designed to capture approximately 87% of the total power. This point is chosen because beyond it, the power gains become less and less significant compared to the required increase in receiver diameter. However, this implies that a substantial portion of the beam's power, around 13%, spills over the edges of the receiver and is lost. Nevertheless, the reader should keep in mind that this is an arbitrary assumption to minimize size and weight while capturing most of the power (to meet SWaP constraints), and that the size can be arbitrarily choose to meet for example other product specification points such as the full width at half maximum (FWHM), 95%, $1/e^4$, and possibly others. Under this specific case, equation (4.3) becomes

$$P_h = \eta_{\text{Rx}} \cdot \eta_{\text{dust}} \cdot P_t \cdot \left(1 - e^{-2}\right). \tag{4.4}$$

The Rayleigh range is the distance along the propagation axis of the Gaussian beam from its waist to the point where the cross-sectional area of the beam has doubled, corresponding to an increase in the beam's radius by a factor of $\sqrt{2}$, as defined in Figure 4.2. This distance represents the range over which the beam remains nearly collimated before diffraction causes significant divergence [97]. Mathematically, it is defined as follows

$$z_R = \frac{\pi w_{0R}^2}{M^2 \lambda}, \tag{4.5}$$

where w_{0R} represents the beam waist of the real beam, M^2 represents the beam quality factor, and λ is the laser wavelength. With appropriate optics, the beam waist can be positioned at the laser output for a perfectly collimated beam, in front of it for focusing, or behind it for defocusing.

Diffraction imposes a natural limit on how tightly a beam can be focused. Even with perfect optics, a beam cannot be concentrated into a point smaller than what diffraction allows. Using lenses with excessively long focal lengths at the emitter won't improve beam focus over long distances (beyond the Rayleigh range), as they have no effect on the natural divergence caused by diffraction. To optimize beam performance over long distances (beyond the Rayleigh range) with a given emitter diameter, the best option is to launch the beam as a perfectly collimated, parallel beam directly from the emitter, meaning the waist should be located at the emitter itself [116].

The M^2 parameter, mentionned in equation (4.5), accounts for the deviation from the ideal Gaussian beam and is defined as follows [117]

$$M^2 = \frac{w_{0R}\theta_R}{w_0\theta}, \tag{4.6}$$

with θ_R, representing the far-field divergence of the real beam. It is important to consider this factor in the modeling process, as for high-power or multimode laser operations, the M^2 value can significantly exceed 1. For example, currently available terrestrial high-power fiber lasers from IPG include single-mode lasers with power outputs up to 3 kW and beam quality factors of $M^2 < 1.1$ (YLR series). On the other hand, multi-mode lasers offer power outputs ranging from 1 kW to over 125 kW (YLS series), but with higher M^2 values, typically ranging from 6 to 50 [71].

Considering the significance of the M^2 factor in assessing beam quality, it is also important to introduce the Beam Parameter Product (BPP) to provide a more comprehensive understanding of a laser beam's characteristics. The BPP is defined as

$$BPP = w_{0R} \cdot \theta_R = M^2 \cdot \frac{\lambda}{\pi}. \tag{4.7}$$

This product provides a metric for both the beam's spatial dimensions and angular divergence, typically expressed in millimeter-milliradians (mm-mrad). A low BPP indicates a high-quality beam that can be focused to a smaller spot or remain collimated over a greater distance.

The required receiver diameter (based on our $\frac{1}{e^2}$ criterion defined previously) is related to the transmitter diameter through Gaussian beam propagation. As stated previously, our design choice for the receiver diameter is $d_{\mathrm{Rx}} = 2R = 2w_R(z)$. Following the same idea, the transmitter diameter is $d_{\mathrm{Tx}} = 2w_{0R}$. Therefore, based on the propagation equation, the relationship between both is expressed with the following equation

$$d_{\mathrm{Rx}} = d_{\mathrm{Tx}} \sqrt{1 + \left(\frac{zM^2\lambda}{\pi \left(\frac{d_{\mathrm{Tx}}}{2}\right)^2} \right)^2}. \tag{4.8}$$

This equation establishes the link between the transmitter and receiver diameters, based on our criterion of 87% light collection, for a collimated laser beam at the transmitter output. Thus, for a transmitter diameter larger than the receiver diameter, this equation has no solution (for z), as we don't focalize. To remedy this and to study the real theoretical limit of the system, that is, the maximum transmission distance for a certain transmitter and receiver diameter, we will place a focusing system at the output of our laser. For details on the changes introduced by adding this focusing system, the reader is referred to Appendix C. Under these conditions, the maximum transmission distance $z_{\max}$ is determined by the equation

$$z_{\max}(\alpha_{\mathrm{opt}}) = \frac{\alpha_{\mathrm{opt}}}{\alpha_{\mathrm{opt}}^2 + 1} \cdot \frac{\pi d_{\mathrm{Tx}}}{4\lambda M^2} \left[\sqrt{d_{\mathrm{Rx}}^2 + (d_{\mathrm{Rx}}^2 - d_{\mathrm{Tx}}^2)\alpha_{\mathrm{opt}}^2} + d_{\mathrm{Tx}} \right], \tag{4.9}$$

where $\alpha = \frac{f}{z_R}$ with f being the focal length of the lens and α_{opt} is the α that maximizes z. This maximum cannot be determined analytically and will therefore be determined numerically for each d_{Tx} and d_{Rx} combination.

Unlike terrestrial systems, where convection contribute significantly to heat rejection, space-based systems rely solely on radiation, resulting in less efficient heat dissipation [118]. For a typical radiator operating at 300K with a high-emissivity material, the heat dissipation is

only about 400W/m². To maintain the receiver within its optimal operating temperature, it is critical to efficiently dissipate heat, especially during the lunar day and for multi-kilowatt systems.

In a simplified design, to analyze the thermal effects on receiver size, we assume that the optical acceptance aperture of the receiver is the same size as its heat rejection aperture. This approach will reduce the heat flux density by distributing the incoming energy over a greater surface area, which simplifies thermal management and prevents component overheating. Additionally, it eliminates the need for heat pipes and avoids consuming extra energy, which would otherwise reduce the net power output of the system. Equation (5.1) can be rewritten as

$$P_{\mathrm{h}} = \eta_{\mathrm{Rx}} P_{\mathrm{in}}, \tag{4.10}$$

where P_{in} is the input power at the receiver. The power dissipated as heat, P_{heat}, is the difference between the input and harvested power

$$P_{\mathrm{heat}} = P_{\mathrm{in}} - P_{\mathrm{h}}. \tag{4.11}$$

Substituting P_{in} gives the heat dissipated as

$$P_{\mathrm{heat}} = P_{\mathrm{h}} \left(\frac{1}{\eta_{\mathrm{RX}}} - 1 \right). \tag{4.12}$$

We define the admissible thermal flux, J_{heat}, as a characteristic of the system, indicating how much heat it can dissipate effectively per unit area (in $\mathrm{W/m^2}$) before reaching a critical point where it could overheat, lose efficiency, or suffer damage. The thermal flux (generated heat) must therefore not exceed J_{heat}. Mathematically, this is expressed as

$$\frac{P_{\mathrm{heat}}}{A} \leq J_{\mathrm{heat}}. \tag{4.13}$$

Solving for the area, we have

$$A \geq \frac{P_{\mathrm{h}} \left(\frac{1}{\eta_{\mathrm{Rx}}} - 1 \right)}{J_{\mathrm{heat}}}. \tag{4.14}$$

For a circular receiver laser collector, this leads to

$$\pi \left(\frac{d_{\mathrm{Rx}}}{2} \right)^2 \geq \frac{P_{\mathrm{h}} \left(\frac{1}{\eta_{\mathrm{Rx}}} - 1 \right)}{J_{\mathrm{heat}}}. \tag{4.15}$$

Then, solving for the diameter, d_{Rx}, we obtain

$$d_{\mathrm{Rx}} \geq 2 \sqrt{\frac{P_{\mathrm{h}} \left(\frac{1}{\eta_{\mathrm{RX}}} - 1 \right)}{\pi J_{\mathrm{heat}}}}. \tag{4.16}$$

We have therefore obtained a constraint on the minimum required diameter, which depends on the harvested power P_{h}, the efficiency η_{Rx}, and the maximum allowable thermal flux J_{heat}. The reader should note that this constraint arises from our design choices and does not take into account the possibility of heat storage or utilization, which might be applicable during the lunar night.

4.1.2 Lunar Dust Attenuation Model

The presence of lunar dust adversely impacts laser transmission due to scattering and absorption. The extent of this effect depends on variables such as the laser wavelength and the specific properties of lunar dust. We aim to introduce a lunar dust attenuation model, based on realistic up-to-date data from currently existing literature. Specifically, the model uses the T-matrix method to simulate the scattering and absorption behavior of lunar dust particles [119]. This method is used because it allows to calculate the scattering and absorption properties of particles with more sophisticated shapes.

It should be mentioned that the interaction of the laser with lunar dust particles deposited on the receiver is neglected, assuming the use of a perfect lunar electrodynamic dust shield, generating a perfect dynamic electric field to repel dust and keep the surface clean [13].

Particle Shape Characterization

Yang Liu *et al.* [99] conducted a comprehensive study on the texture and shape characteristics of lunar dust, focusing on parameters such as aspect ratio and complexity factor. Their analysis revealed that lunar dust particles exhibit irregular, angular shapes, distinguishing them from simpler geometric models such as spheres. They demonstrated that lunar dust can be well approximated by an elongated spheroid, also known as a prolate spheroid, as shown in Figure 4.3. Using the least-squares method, they determined the distribution of aspect ratios (defined as the ratio of the minor axis to the major axis) and the complexity

factor (a measure of particle angularity, defined as the ratio of the measured perimeter to the calculated ellipse perimeter) for the lunar samples analyzed. Their results indicated a peak aspect ratio around 0.7 and a complexity factor centered around 1.15. While the prolate spheroid model may not capture every jagged edge or surface feature, it effectively represents the overall elongation, reflected in the aspect ratio, and provides a useful framework for studying the optical properties of lunar dust.

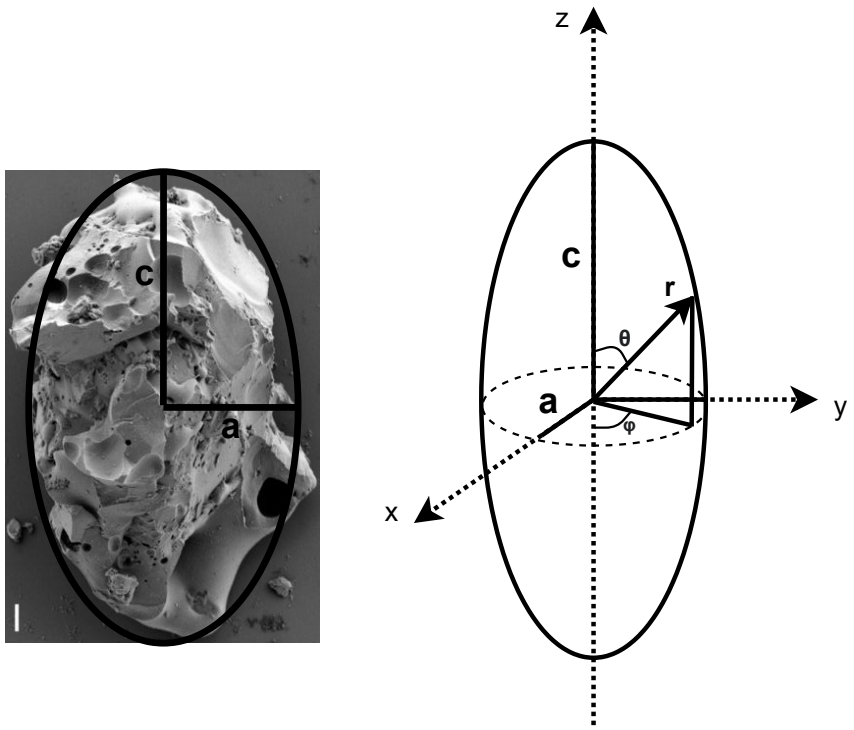

Figure 4.3 3D illustration of particle shape characterization by a prolate spheroid and its geometrical parameters along z, the axis of revolution. Picture credit : Chiaramonti Debay/NIST [3].

In this analysis, we will specifically focus on prolate spheroids, which are described in spherical coordinates, as shown in Figure 4.3. Due to the symmetry of the prolate spheroid around the z-axis, the radial distance r depends only on the polar angle θ, and is given by the following expression

$$r(\theta) = \frac{ac}{\sqrt{a^2 \cos^2\theta + c^2 \sin^2\theta}}, \tag{4.17}$$

where a is the semi-axis length along the x- and y-axes, and c is the semi-axis length along the z-axis, which serves as the axis of revolution.

The aspect ratio, AR, is defined as the ratio between the maximum and minimum distances from the origin, where $c > a$ for elongated spheroids. This definition differs slightly from that of Yang Liu *et al.*:

$$AR = \frac{r_{\max}}{r_{\min}} = \frac{c}{a}. \tag{4.18}$$

We also assume that the particles in the dust cloud are randomly oriented and non-interacting. As will be discussed below, the T-matrix formalism enables the analytical calculation of the average optical properties across all possible orientations [119]. This is achieved by integrating the contributions from different orientations, weighted by their probability, which is uniform for completely random orientations. In the radiative transfer theory paragraph, we will further discuss that particles in a lunar dust cloud are considered non-interacting due to their low density and small size. This implies that their electromagnetic fields and scattering interactions do not significantly affect one another. In fact, in our case, τ (the optical depth of the cloud over a distance L) is much less than 1, indicating that the cloud is optically thin, and multiple scattering can be neglected.

T-matrix Method

Unlike the assumptions made in Mie theory, where lunar dust particles are approximated as spherical, the T-matrix method allows for a more accurate representation of their actual angular and irregular shapes [119] [120]. Indeed, this method is a powerful technique used to calculate the scattering and absorption properties of particles with arbitrary shapes, such as prolate spheroids. It is especially useful for determining the orientation-averaged extinction cross-section, which quantifies the total amount of light blocked by particles (both absorbed and scattered). More precisely, it allows for efficient calculation by computing the T-matrix for one orientation and applying rotational transformations to derive properties for other orientations.

A comprehensive explanation of the T-matrix method is provided in [119], and the key con-

cepts, notations, and specifics of the algorithm used are discussed in detail in [121]. Rather than restating all this information, we will summarize the most relevant points, focusing on how the wavenumber, particle size, aspect ratio, and refractive index play roles in the T-matrix calculation for prolate spheroidal particles. For the complete methodology and additional equations, the reader is referred to [121].

This method involves solving Maxwell's equations for electromagnetic fields in the presence of a particle, using expansions in terms of vector spherical wave functions (VSWFs). The incident, scattered, and internal electric fields are expressed as series expansions involving these functions, as following

$$\mathbf{E}_{\text{inc}} = E_0 \sum_{n=1}^{\infty} \sum_{m=-n}^{n} \left(a_{nm} \mathbf{M}_{nm}^{(1)}(kr) + b_{nm} \mathbf{N}_{nm}^{(1)}(kr) \right), \tag{4.19}$$

$$\mathbf{E}_{\text{sca}} = E_0 \sum_{n=1}^{\infty} \sum_{m=-n}^{n} \left(p_{nm} \mathbf{M}_{nm}^{(3)}(kr) + q_{nm} \mathbf{N}_{nm}^{(3)}(kr) \right), \tag{4.20}$$

$$\mathbf{E}_{\text{int}} = E_0 \sum_{n=1}^{\infty} \sum_{m=-n}^{n} \left(c_{nm} \mathbf{M}_{nm}^{(1)}(k_2 r) + d_{nm} \mathbf{N}_{nm}^{(1)}(k_2 r) \right), \tag{4.21}$$

where E_0 is the amplitude of the incident electric field (assumed to be unity for linearity), $k = \frac{2\pi}{\lambda}$ is the wavenumber of the incident light in the surrounding medium, as defined in the previous Chapter (with λ being the wavelength), and $k_2 = \frac{2\pi n'_{particle}}{\lambda}$ is the wave number inside the particle, with $n'_{particle}$ being the complex refractive index of the lunar dust particle. The functions $\mathbf{M}_{nm}^{(1)}$ and $\mathbf{N}_{nm}^{(1)}$ are the magnetic and electric regular (finite at the origin) VSWFs, while $\mathbf{M}_{nm}^{(3)}$ and $\mathbf{N}_{nm}^{(3)}$ are the irregular magnetic and electric VSWFs that satisfy the radiation condition for outgoing spherical waves. $a_{nm}, b_{nm}, p_{nm}, q_{nm}, c_{nm}, d_{nm}$ represents the expansion coefficients [122].

The size and shape of the particle are incorporated through the boundary conditions applied at the particle's surface, which depend on the particle's geometry, defined by its overall size and aspect ratio. The overall size of the particle is characterized by the size parameter x, given by

$$x = kr, \tag{4.22}$$

where r is a characteristic length scale of the particle, define as the radius of an equivalent

sphere.

Applying the boundary conditions leads to a set of linear equations relating the expansion coefficients of the incident, scattered, and internal fields. These relationships can be represented using matrices

$$\begin{pmatrix} p \\ q \end{pmatrix} = -P \begin{pmatrix} c \\ d \end{pmatrix}, \quad \begin{pmatrix} a \\ b \end{pmatrix} = Q \begin{pmatrix} c \\ d \end{pmatrix}, \tag{4.23}$$

$$\begin{pmatrix} p \\ q \end{pmatrix} = T \begin{pmatrix} a \\ b \end{pmatrix}, \quad \begin{pmatrix} c \\ d \end{pmatrix} = R \begin{pmatrix} a \\ b \end{pmatrix}, \tag{4.24}$$

where P, Q, T, and R are matrices derived from the boundary conditions and depend on the particle's size, shape (aspect ratio), and refractive index $n'_{particle}$. Our focus is on the matrix T, which encapsulate the particle's scattering properties and are functions of the wavenumber k, the size parameter x, the aspect ratio AR, and the refractive index $n'_{particle}$.

The orientation-averaged extinction cross-section $\langle C_{\text{ext}} \rangle$ for randomly oriented particles, such as those in a lunar dust cloud, is calculated using the T-matrix elements and can be computed as [119]

$$\langle C_{\text{ext}} \rangle = \frac{-2\pi}{k^2} \sum_{n=1}^{\infty} \sum_{m=0}^{n} (2 - \delta_{m,0}) \text{Re} \left(T^{11}_{nn|m} + T^{22}_{nn|m} \right), \tag{4.25}$$

where $T^{11}_{nn|m}$ and $T^{22}_{nn|m}$ are elements of the T-matrix that describe the scattering behavior of the particles for various n and m. The indices m and n correspond to the projected angular momentum along the z-axis and total angular momentum, respectively, with $|m| \leq n$ and $n = 1 \ldots \infty$. The Kronecker delta δ_{m0} ensures proper weighting for $m = 0$ [119] [122]. We have also

$$\langle C_{\text{ext}} \rangle = \langle C_{\text{abs}} \rangle + \langle C_{\text{sca}} \rangle. \tag{4.26}$$

Here, $\langle C_{\text{abs}} \rangle$ and $\langle C_{\text{sca}} \rangle$ designate the orientation-averaged absorption cross-section and scattering cross-section, respectively.

The calculation of the T-matrix involves integrating over the particle's surface, which re-

quires knowledge of the particle's geometry (define previously, for a prolate spheroid). The angular functions used in these integrals are derived from the associated Legendre functions $P_n^m(\cos\theta)$, where θ is the polar angle. The Legendre polynomials $P_n(\cos\theta)$ and associated functions incorporate the particle's aspect ratio and size parameters.

Due to the complexity of the particle shape, Gauss-Legendre quadrature are employed to compute the necessary integrals over the variable $\cos\theta$. For further details, the detailed procedures of the T-matrix calculation, including the specific algorithms for matrix inversion and handling of numerical issues, the reader is referred to [121].

Radiation Transfer Equation

This subsection models the transmission efficiency of laser light as it interacts with a lunar dust particle cloud. By employing the vector radiative transfer equation (VRTE) and considering the unique properties of coherent laser light, we derive an expression for the transmission efficiency and discuss its implications [123].

For the analysis, the Stokes vector I_c is introduced, which represents the intensity and polarization state of the laser light. The Stokes vector is express as follows

$$I_c = \frac{1}{2}\sqrt{\frac{\epsilon_1}{\mu_0}}\begin{bmatrix} E_{\theta 0}E_{\theta 0}^* + E_{\phi 0}E_{\phi 0}^* \\ E_{\theta 0}E_{\theta 0}^* - E_{\phi 0}E_{\phi 0}^* \\ 2\,\mathrm{Re}(E_{\theta 0}E_{\phi 0}^*) \\ 2\,\mathrm{Im}(E_{\theta 0}E_{\phi 0}^*) \end{bmatrix}, \tag{4.27}$$

where $E_{\theta 0}$ and $E_{\phi 0}$ are the components of the electric field in the θ and ϕ directions. ϵ_1 and μ_0 are the permittivity and the permeability of free space, respectively.

The evolution of the Stokes vector as the laser light propagates through the dust cloud is governed by the radiative transfer equation

$$\frac{dI_c(z)}{dz} = -n_0 K(\hat{z}) I_c(z), \tag{4.28}$$

where z is the path length along the propagation direction $\hat{z}$, n_0 is the number density of particles in $particles/m^3$, and $K(\hat{z})$ is the extinction matrix.

Assuming a uniform particle density along the LoS and neglecting scattering paths involving multiple interactions with the same particle (Twersky approximation), the formal solution to the transfer equation is

$$I_c(z) = \mathcal{H}[\hat{z}, z] I_c^{inc}, \tag{4.29}$$

where I_c^{inc} is the incident Stokes vector, and $\mathcal{H}[\hat{z}, z]$ is the attenuation matrix defined by

$$\mathcal{H}[\hat{z}, z] = \mathrm{e}^{-n_0 z K(\hat{z})}. \tag{4.30}$$

Due to the random orientations of the dust particles, the scattering environment becomes effectively isotropic, similar to that of spherical particles. For spherically symmetric and optically isotropic particles, the extinction matrix simplifies to a scalar times the identity matrix

$$\langle K(\hat{z}) \rangle = \langle C_{ext} \rangle \Delta, \tag{4.31}$$

where $\langle C_{ext} \rangle$ is the average extinction cross-section, and Δ is the identity matrix.

Substituting this into the previous equation, the Stokes vector simplifies to

$$I_c(z) = \mathrm{e}^{-\alpha_{\mathrm{ext}} z} I_c^{\mathrm{inc}}, \tag{4.32}$$

where the extinction coefficient α_{ext} is

$$\alpha_{ext} = n_0 \langle C_{ext} \rangle = n_0 \left(\langle C_{sca} \rangle + \langle C_{abs} \rangle \right). \tag{4.33}$$

This expression indicates that all components of the Stokes vector attenuate exponentially with distance, while the polarization state remains unchanged since the attenuation is uniform across all components. This behavior follows the Bouguer-Beer-Lambert law [123].

The transmission efficiency η_{dust} due to the dust cloud is then defined as

$$\eta_{\mathrm{dust}} = \frac{I_c(z)}{I_c^{\mathrm{inc}}} = e^{-\alpha_{\mathrm{ext}} z}. \tag{4.34}$$

The hypotheses that led to this derivation are listed below:

- **Illumination by quasi-monochromatic light**: This is justified in our case because lasers are designed to have a very narrow bandwidth, meaning the light is quasi-monochromatic.
- **Each particle in the scattering medium is assumed to be located in the far-field zone with respect to other particles**: Given the micrometer size of the particles, the wavelength of the laser light and the average distance between particles from low density, this approximation is justified. This essentially means that our optical thickness is sufficiently low to consider this hypothesis.
- **Neglecting multiple scattering paths involving the same particle (Twersky approximation)**: Although the dust cloud contains a large number of particles, the density is sufficiently low such that the probability of a wave scattered by a particle returning to interact with the same particle is negligible. Ignoring these paths greatly simplifies the calculations without introducing significant errors in the results. This again essentially means that our optical thickness is sufficiently low to consider this hypothesis.
- **Ergodicity hypothesis**: The particles are in constant motion, and their positions and orientations change over time. Thus, the time-averaged properties of the system are equivalent to an average over all possible positions and states.
- **Statistical independence of particles and uniform distribution along the optical path**: Each particle is considered independent of the others. Additionally, on spatial scales relevant to the interaction with the laser, the dust cloud can be considered to have a uniform density along the optical path. In reality, since the density varies with the subsolar angle, this holds for relatively short optical path distances.
- **Convex scattering medium**: By assuming the scattering medium is convex, we eliminate the possibility that light, after leaving the medium, can re-enter it, which is justified in our case.

Particle size, refractive index and particles density distribution

To account for the distribution of particle sizes, the rigorous approach would be to calculate the average extinction, $\langle C_{\text{ext}} \rangle$, by integrating the orientation-averaged extinction over all possible sizes, weighted by the normalized distribution of equivalent-sphere radii $n(r)$.

However, for electrostatically lofted particles, such a distribution is currently unknown [19]. Therefore, we define r_{average}, referred to as "The Midpoint", as the radius at which $\langle C_{\text{ext}}(r)\rangle$ equals its mean value. So, we assume that the particles are evenly distributed and we take an average value for the particle size corresponding to the mean extinction cross-section. Mathematically, we solve the equation

$$\langle C_{\text{ext}}(r_{\text{average}})\rangle = \langle C_{\text{ext}}\rangle_{\text{mean}} \tag{4.35}$$

where the mean extinction cross-section $\langle C_{\text{ext}}\rangle_{\text{mean}}$ over the given range $r_{\min}$ to $r_{\max}$ is

$$\langle C_{\text{ext}}\rangle_{\text{mean}} = \frac{1}{r_{\max} - r_{\min}} \int_{r_{\min}}^{r_{\max}} \langle C_{\text{ext}}(r)\rangle \, . \tag{4.36}$$

Concerning the complex refractive index of lunar dust, the methodology is the same of the one presented in Chapter 3. For convenience, most important points are repeated here. It is expressed as

$$\tilde{n} = n^* + ik^*, \tag{4.37}$$

where the real part n^* describes the phase velocity of light as it propagates through the lunar dust medium. This real component primarily governs optical effects such as refraction. In contrast, the imaginary part k^* quantifies the absorption of electromagnetic waves as they travel through the medium, indicating how much light is absorbed.

To determine the complex refractive index, we use the dielectric function, represented by the real part ϵ_1 and the imaginary part ϵ_2. Specifically, ϵ_1, represents the material's ability to store electrical energy through polarization, while ϵ_2 indicates the material's capacity to dissipate energy as heat, reflecting dielectric losses. Using these dielectric function values from the literature for a specified wavelength [106], we calculate the real and imaginary parts of the complex refractive index with the following equations

$$n^*(\lambda) = \sqrt{\frac{\sqrt{\epsilon_1^2 + \epsilon_2^2} + \epsilon_1}{2}}, \tag{4.38}$$

$$k^*(\lambda) = \sqrt{\frac{\sqrt{\epsilon_1^2 + \epsilon_2^2} - \epsilon_1}{2}}. \tag{4.39}$$

These expressions allow us to model the wavelength-dependent refractive index of lunar dust,

using the dielectric properties of astronomical silicate.

The dust grain density distribution above the lunar surface is determined based on the assumption that our scenario takes place in the polar regions under a high subsolar angle. For the ground-to-ground scenario, we focus on the near-surface dust density resulting from electrostatic levitation, while neglecting the contribution from meteorite impacts that eject lunar dust into the exosphere, as the LADEE experiment has shown this effect to be negligible [124].

The phenomenon of electrostatic dust lofting is observed in the illuminated regions of the Moon, where dust particles are lifted due to electrostatic forces [19], [125]. According to the results from [19], the number density of charged dust grains in the near-surface layer of the Moon's illuminated side is approximately $10^3\,\mathrm{cm}^{-3}$, though this value can vary depending on the subsolar angle. This high density is attributed to the abundance of photoelectrons, including those emitted directly from the surfaces of the dust grains themselves. The particles involved in this lofting process typically range in size from 0 to 0.2 micrometers.

The particle density distribution as a function of height above the lunar surface is given by the following equation, which is derived from [19] using the least-squares fitting method

$$n(h) = -4.166 \times 10^8 \cdot \ln\left(\frac{h}{868}\right), \tag{4.40}$$

valid for $0 \leq h \leq 868\,\mathrm{cm}$, where $n(h)$ is in particles/m^3 and h in centimeters. The parameters used in this distribution are sourced from [19], with a subsolar angle set at $\theta = 87°$, corresponding to the polar regions of the Moon. Additionally, the photoelectron density at the lunar surface is $N_0 = 1.3 \times 10^2\,\mathrm{cm}^{-3}$, the thermal energy of the electrons is $T_e = 1.3\,\mathrm{eV}$, and the quantum yield is based on data from the cited source. It should be noted that, although this distribution corresponds to a subsolar angle of 87 degrees, the density tends to vary only slightly with the subsolar angle [19].

4.2 Performance Evaluation

The impact of lunar dust on the system's performance is quantitatively assessed through simulation studies. Before calculating the harvested power, the extinction cross-sectional area of the lunar dust particles is determined. Next, the attenuation coefficient and the

efficiency factor η_{dust} are evaluated in our ground-to-ground link on the lunar surface. The harvested power is then calculated under realistic conditions and assuming perfect tracking with no losses due to beam misalignment. After that, design consideration for the transmitter and receiver aperture are discussed based on our system model. Finally, we discuss practical consideration and the validity of the chosen approach.

4.2.1 Simulation Parameters

The selection of the laser must optimize several criteria: high power, good beam quality, a wavelength that matches the photovoltaic cell, and high electrical-to-optical conversion efficiency. For this reason, we choose a single-mode high-power fiber laser operating at a wavelength of 1064 nm. Current high-power lasers are typically ytterbium-doped (Yb) fiber lasers and have operating wavelength that varies from approximately 1007nm to 1070nm, depending on the design. Choosing 1064nm is acceptable and aligns with the peak efficiency of most PV receivers. Consequently, we set the wavelength at 1064 nm for our simulation, meaning that the system must select a photovoltaic cell to match the laser, rather than the other way around. The transmitted power P_t is assumed to range between 1 kW and 10 kW. For this laser, we assume a reasonably low Beam Parameter Product of 2 mm·mrad, which corresponds to an M^2 parameter of approximately 5.9, based on terrestrial fiber laser performance.

Among the available photovoltaic cells, indium-gallium-arsenide (InGaAs) is selected. $In_{0.24}Ga_{0.76}As$ cells are optimized for a bandgap around 1.08 eV, which closely aligns with the laser wavelength of 1064 nm. These cells have demonstrated a maximum conversion efficiency of 45.5% under high-intensity illumination over small areas [126].

Considering our receiver design, explained in the system model section, a reasonable maximum admissible thermal flux J_{heat} needs to be chosen. As explained previously, in space environments, the J_{heat} values for radiators are generally much lower than in terrestrial applications. Although materials such as carbon composites can withstand temperatures above 1000 K, allowing J_{heat} to exceed $1000\,\text{W/m}^2$ under optimal conditions, these materials are not typically used in standard space applications. However, for this study, we still assume an optimistic value of $J_{\text{heat}} = 1000\,\text{W/m}^2$.

Based on the dielectric function data provided in [106] and the formulas (4.38) and (4.39), the complex refractive index for a wavelength of 1064 nm is determined to be $n = 1.733 + i0.05$.

The value of the real and imaginary part of the refractive index is within the range of values given in the literature for lunar dust, which solidifies the relevance of the chosen approach. Given the space conditions, the refractive index of the medium surrounding the particle is set to 1.0.

Below is a table summarizing the parameters for our considered scenario.

Table 4.1 Summary of Parameters: Final Approach.

Parameter	**Value**
Transmission Range	up to 20 km
Transmitted Power	1 to 10 kW
Particle Size Range	up to 200 nm
Particle Complex Refractive Index	$1.733 + i\,0.05$
Particle Average Aspect Ratio	1.4286
Particles Density	From $2.76628 \cdot 10^9$ to 0 particles/m^3
Particle Height	0 to 8.68 m
Medium Refractive Index	1.0
Laser Wavelength (λ)	1064 nm
BPP	2 mm·mrad
M^2	5.9
J_{heat}	1 kW/m^2
EHCE (%)	45.5% [126]

4.2.2 Results and Discussions

First of all, simulations were carried out to assess the influence of lunar dust on laser power transmission for our ground-to-ground link scenario. Then, the results of these simulations were used to determine the power harvested by a receiver, considering varying transmit powers and distances z within our proposed system model. Finally, design choices for the receiver and transmitter aperture are presented.

Firstly, the average extinction cross-section was determined using the methodology outlined in Section 2, in conjunction with the data specified in Table 4.1. The results are presented as a function of particle radius and aspect ratio, and are illustrated in Figures 4.4 and 4.5.

One of the key observations is the significant influence of particle size on the extinction

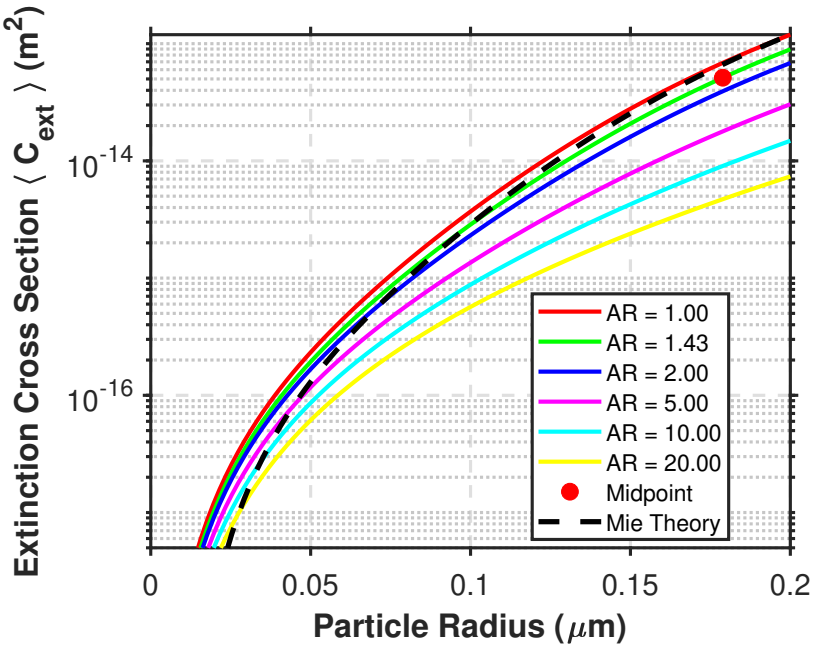

Figure 4.4 Averaged extinction cross-section as a function of particle radius for various particle aspect ratios.

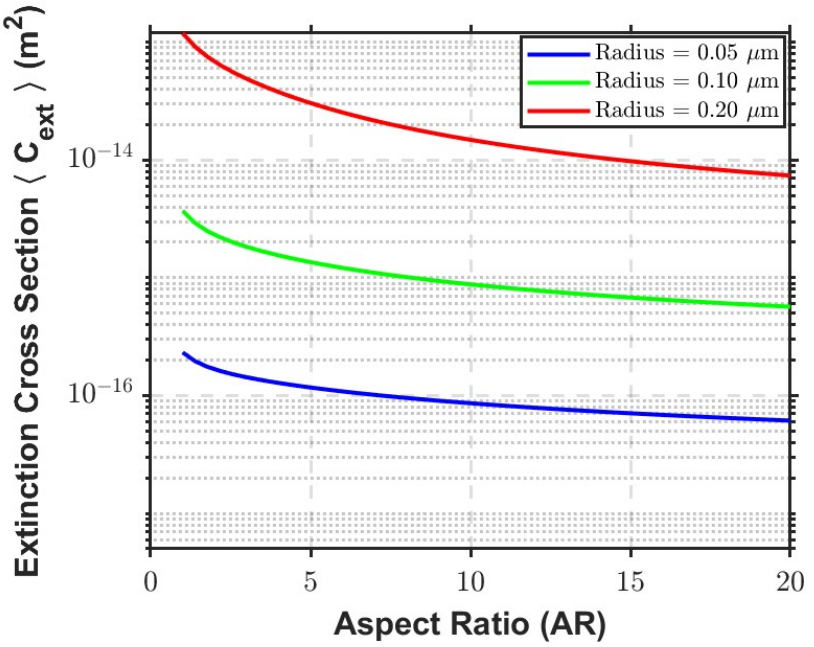

Figure 4.5 Averaged extinction cross-section as a function of particle aspect ratio for different particle radii.

cross-section. Although it might be expected that larger particles show an increased ability to absorb or scatter laser light, this increase appears to follow an exponential trend (as it is Log-scale), clearly demonstrating that particle size plays a crucial role. We can also observe that when comparing Mie theory and the T-matrix method for the spherical case, the results are not exactly identical, particularly for very small particle sizes. This discrepancy arises primarily due to numerical truncation and the use of the Gauss-Legendre approximation in the T-matrix method. However, since our midpoint is selected at a location where both theories yield comparable results, the deviation in this case does not impact our analysis.

Furthermore, the curves corresponding to different aspect ratios reveal that as the particle aspect ratio increases, the extinction cross-section decreases. This suggests that more elongated particles tend to scatter or absorb less laser light on average. Figure 4.5 further highlights this influence and shows that increasing the aspect ratio leads to a decrease in the extinction cross-section. Importantly, the midpoint defined in the system model section is identified in Figure 4.4 for the considered average aspect ratio, dividing the area equally and providing a representative marker for the overall behavior of the extinction cross-section over the particle range.

An important feature to show is the attenuation coefficient as a function of height. This is shown in Figure 4.6. We can note that in our case, the attenuation coefficient takes the form of our density, since our $\langle C_{\text{ext}} \rangle$ has been set to a mean size and aspect ratio.

We then analyze the effect of lunar dust as a function of transmission distance for different heights. Figure 4.7 clearly demonstrates that lunar dust can have a significant impact on transmission efficiency near the surface under illuminated conditions. This phenomenon is influenced by the electrostatic lofting of lunar dust in a ground-to-ground link, which is the dominant effect considered in the graph, as already mentioned. Naturally, the greater the transmission distance, the more lunar dust interferes with the laser beam, through absorption and scattering mechanisms. For a realistic transmission distance of 5 km, the losses are estimated.

Figure 4.8 illustrates the harvested power as a function of transmission distance and transmitted power at various heights, based on equation 5.1 which is independent of the transmitter and receiver size. The graph shows that close to the lunar surface, due to the influence of lunar dust, the amount of energy that can be harvested is reduced. To minimize these

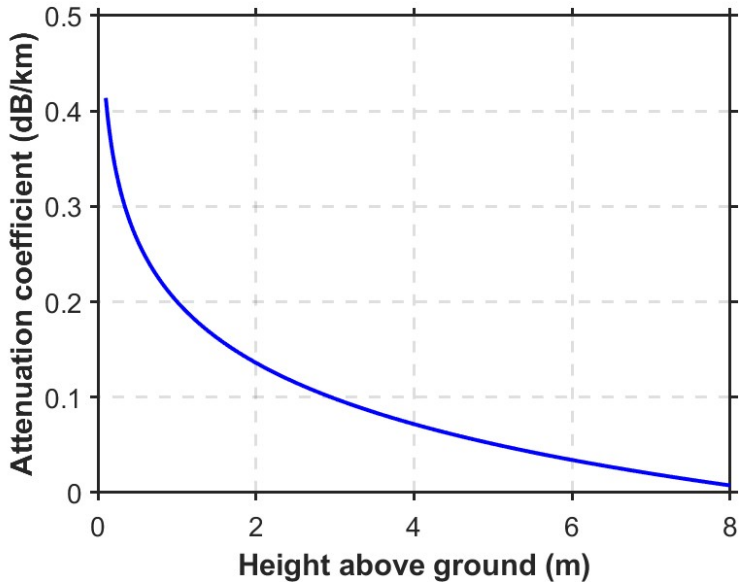

Figure 4.6 Attenuation coefficient as a function of height above the lunar surface.

losses, it becomes advantageous to position transmitters and receivers at a height of around 10 meters, where the dust's impact becomes negligible, for this location. In this case, the primary source of energy loss is due to the conversion efficiency of the collector panel, which converts laser energy into electrical energy, as well as the attenuation from the $\frac{1}{e^2}$ factor of the Gaussian beam, in our case. For instance, if we aim to transmit 5 kW over a distance of 15 km, the harvested power would be 774 W at 0.5 meters, 1211 W at 2 meters, 1629 W at 5 meters, and 1947 W at 9 meters above the surface, where the influence of lunar dust becomes negligible. These orders of magnitude confirm the feasibility of the system for powering receivers of several kilowatts.

In practice, the transmission distances shown in Figure 4.8, which extend up to 20 km, may be challenging to achieve near the surface due to the curvature of the Moon and its smaller size compared to Earth. Such line-of-sight distances are, therefore, only realistic at higher altitudes to overcome the horizon, as demonstrated in Figure 4.9. The equation that describes this (see the derivation in the appendix) is the following

$$TxRxRange(h_t, h_r) = \sqrt{h_t^2 + 2h_tR} + \sqrt{h_r^2 + 2h_rR} \tag{4.41}$$

where h_t represents the height of the transmitter, h_r represents the height of the receiver, and R is the radius of the Moon (considered perfectly spherical). In our system model shown

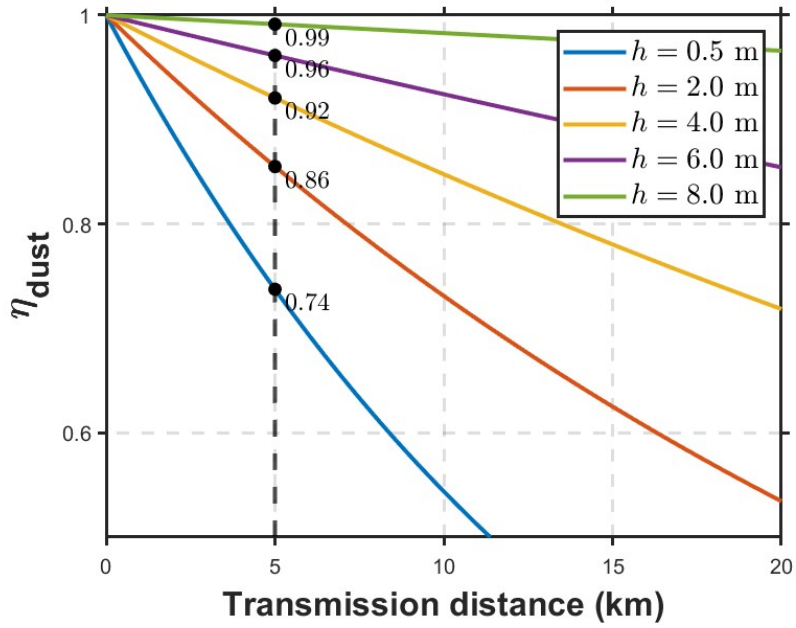

Figure 4.7 Dust transmission efficiency (η_{dust}) as a function of transmission distance for different heights.

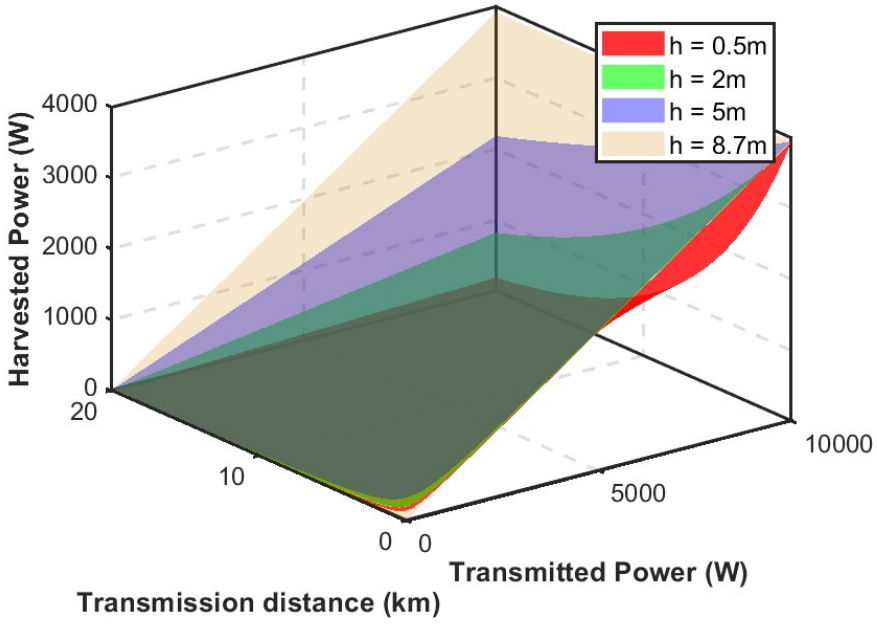

Figure 4.8 Harvested power as a function of transmitted power and transmission distance for different transmission heights in a ground-to-ground link, and for adapted receiver diameter, based on equation (5.1).

in Figure 4.1, we assume $h_t = h_r$ for the simplicity of the analysis, and the consistency of our model. Indeed, in our lunar dust attenuation model, we assume a flat lunar surface between the transmitter and receiver, and based on Figure 4.9, this assumption holds true for sufficiently small distances, typically below 5 km. Beyond this, the accuracy of our lunar dust attenuation model tends to decrease, as the dust density tends to vary along the LoS. It should also be noted that near-surface beam propagation at lower altitudes can be affected by the lunar surface topology, including crater walls, hills, and ridges, which can affect the optical propagation along the lunar surface depending on the specific location where OPB is taking place. However, our simplified scenario does not take these topographical variations into account, as it assumes a flat lunar surface. Incorporating topographical details would require a more complex model, introducing the need to know the specific topology of the analyzed location.

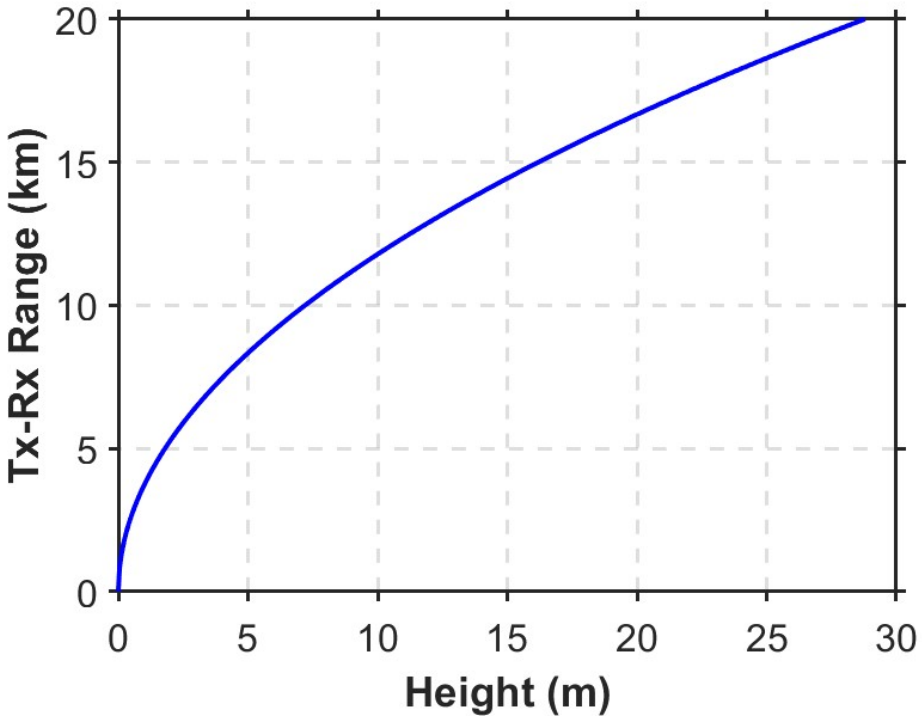

Figure 4.9 Possible transmitter-receiver range on the Moon as a function of transmission height.

In general, the applicability and accuracy of our ground-to-ground model are limited to short transmission distances, typically a few kilometers at most. Several factors contribute to this limitation. Firstly, as the transmission distance increases, the curvature of the Moon becomes

more significant, making the optical path more complex. Secondly, multiple scattering effects tend to become more pronounced over longer distances, further affecting the attenuation of the transmitted laser light. Lastly, while the variation in particle density due to changes in the subsolar angle is expected to have a minor effect, it may still contribute to slight variations in the model's predictions. These factors collectively restrict the validity of the model to shorter transmission ranges.

Before designing such a system, it is prudent to analyze whether it meets the constraints for space applications and adheres to SWaP considerations. If we decouple thermal management and focus solely on analyzing the size of the transmitter and receiver while maximizing the transmission distance and power, the optimal design would depend on the receiver size compared to transmitter size, as shown in Figure 4.10. In the case without a lens, the laser is launched perfectly collimated, and as long as the receiver diameter is larger than that of the transmitter, a solution can be found. In this scenario, for a fixed receiver diameter, we observe that to maximize the transmission distance, the transmitter diameter should be designed such that the beam reaches the receiver's size at the Rayleigh range. Adding an optimal focusing lens allows us to further optimize this distance and enables a solution even in cases where the transmitter diameter is larger than the receiver one as the lens allows to focus the beam. We can also observe that for distances far away beyond the Rayleigh range, the optimal configuration with a lens is the same as without a lens. It is because diffraction imposes a limit on how tightly a beam can be focused.

The Figure 4.11 gives us more insight about the behavior of the system. The 3 curves correspond to the 3 possible scenarios. When we are far from the Rayleigh range (blue curve), diffraction dominates, and adding a focusing system with extremely long focal lengths does not improve performance, as the beam's natural divergence cannot be overcome. When we are near the Rayleigh range (red curve), adding an optimized focusing system slightly extends the maximum range and shifts the optimal point, improving system efficiency. When we are within the Rayleigh range (yellow curve), a focusing system is essential to efficiently reach the target, but not all focal lengths provide a solution due to limits in beam concentration and spot size.

If, however, we decide to account for the thermal management constraints of the receiver that we have establish previously, and that is mostly relevant during the lunar day and for multi-kilowatt systems, we notice that making compact receiver becomes challenging. Assuming

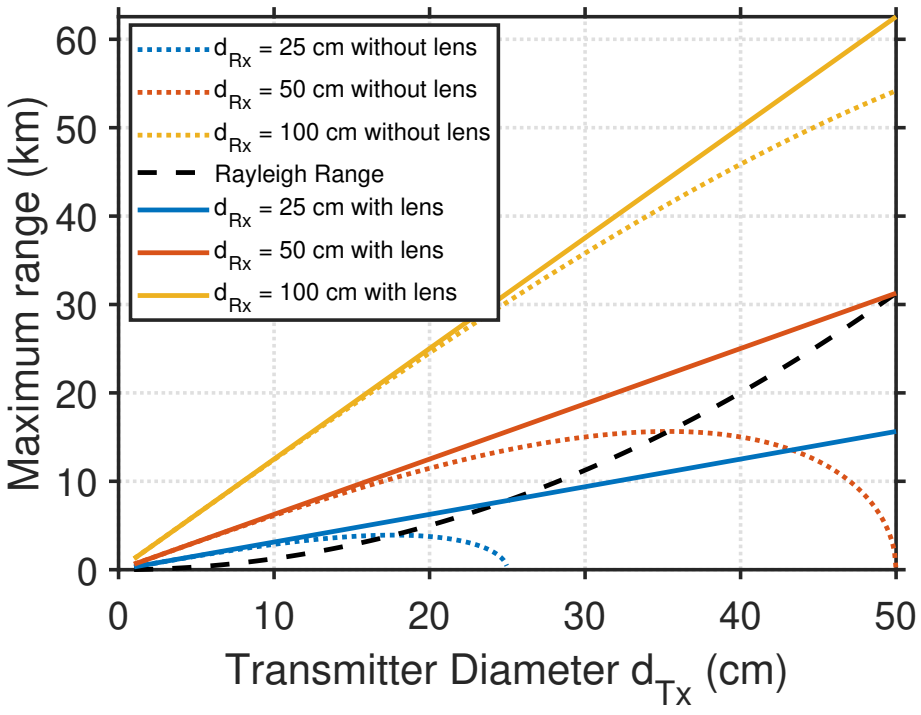

Figure 4.10 Maximum transmission distance as a function of transmitter diameter for different receiver diameter, to maintain 87% of the collected light, without lens (collimated) and with optimal lens.

an optimistic heat rejection capacity of 1 kW/m^2, as outlined in the simulation parameters section, Figure 4.12 illustrates that the receiver size increases rapidly, reaching several meters in diameter to deliver just a few kilowatts of power.

On the other hand, as power output increases, the transmitter aperture can be reduced. This is because a larger receiver does not require the beam to be as precisely collimated, making beam divergence less critical. With a larger target area, the receiver can be placed beyond the Rayleigh range, allowing for smaller transmitter optics. As a result, the transmitter can remain relatively small, on the order of tens of centimeters in diameter, as shown in Figure 4.12. While it is technically feasible to build larger optics, cost and practicality make it advantageous to keep the transmitter optics within commercially available sizes, ideally in the range of a few tens of centimeters. Beyond this size, costs and engineering complexity increase dramatically.

If the heat rejection intensity can be enhanced by new improvement in thermal management

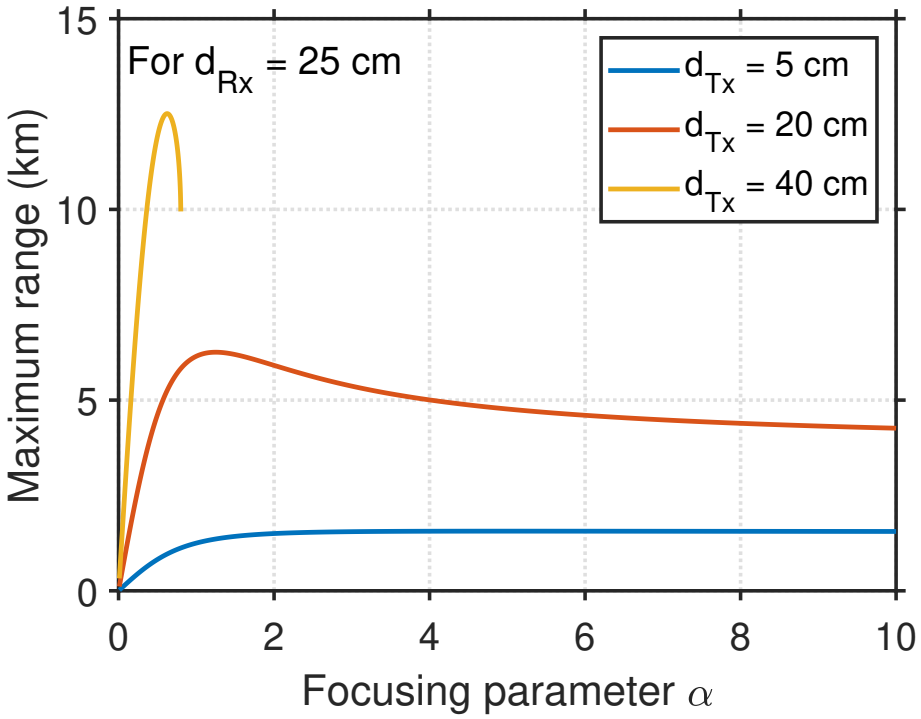

Figure 4.11 Maximum transmission distance as a function of the focusing parameter for three different transmitter diameters, while fixing the receiver diameter to 25 cm.

techniques, the receiver size can be reduced to more manageable dimensions, as shown in Figure 4.13. In this improved scenario, for an electrical output power of one kilowatt and increased heat rejection intensity, receivers could be designed to be around half a meter in size. Such a compact receiver would be suitable even for small lunar rovers, expanding the possibilities for mobile exploration units. However, this reduction in receiver size necessitates a slight increase in the transmitter aperture to maintain beam collimation and efficiency, ensuring that the smaller receiver still captures the majority of the transmitted power.

4.3 Conclusions

In this study, we have analyzed the feasibility and performance of a ground-to-ground laser power transmission system on the lunar surface, taking into account the impact of LLD on laser transmission. By employing the T-matrix method and radiative transfer theory, we modeled the scattering and absorption effects of lunar dust particles on a 1064 nm laser, considering their non-spherical shapes, sizes, and refractive indices. Our simulations demonstrated that lunar dust can notably attenuate laser transmission near the surface due to electrostatic dust lofting, but this effect tends to diminishes with height becoming negligible

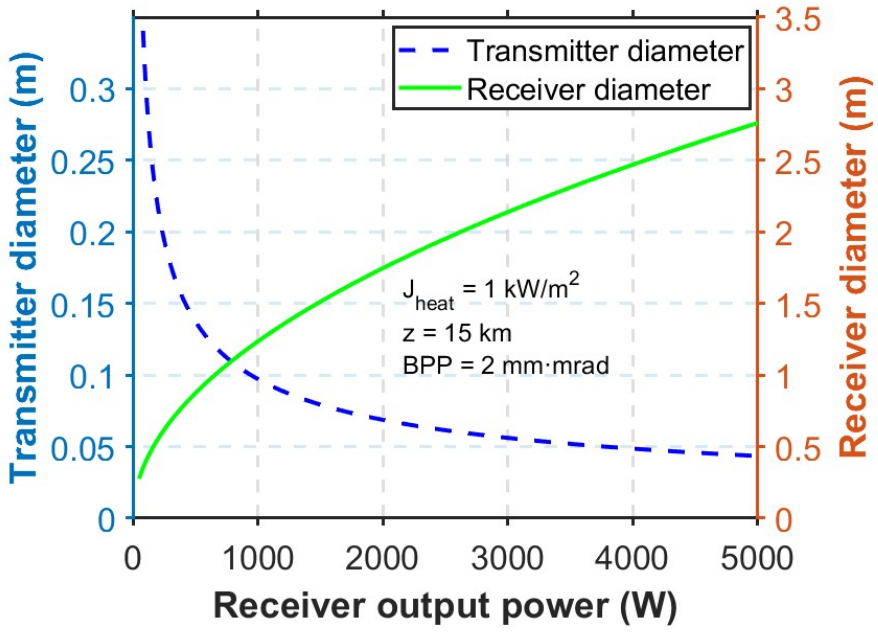

Figure 4.12 Transmitter and receiver diameter as a function of receiver output power, for different fix parameters, based on equation 4.8 and 4.16, for a collimated beam, to maintain 87% of the collected light.

at approximately 8 meters, for our near polar scenario under illuminated condition.

Additionally, we discussed design considerations for the transmitter and receiver apertures, highlighting the importance of selecting carefully the parameters to meet SWaP requirements. Our findings underscore the importance of carefully considering the trade-offs between receiver size and thermal rejection capabilities, mostly during the lunar day and for multi-kilowatt systems. To conclude, this work provides valuable insights into optimizing OPB systems in dusty lunar environments, contributing to reliable energy solutions for future lunar exploration missions.

4.4 Additional Comments

When analyzing the beam propagation model from Chapter 3, we confirm that our initial propagation model is actually a special case of the Gaussian one. Indeed, based on equation (4.7) and equation (3.7), we have:

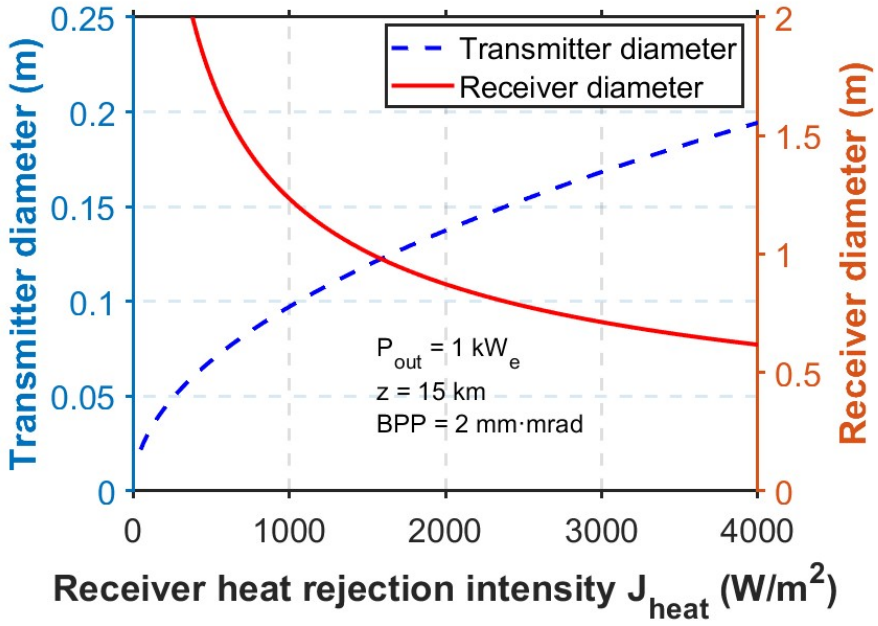

Figure 4.13 Transmitter and receiver diameter as a function of receiver heat rejection intensity, for different fix parameters, based on equation 4.8 and 4.16, for a collimated beam, to maintain 87% of the collected light.

$$d_t = \frac{4R \cdot BPP}{d_R}. \tag{4.42}$$

On the other hand, by considering the Gaussian propagation equation (4.8) and assuming we are well beyond the Rayleigh range such that $z >> z_r$, the equation also simplifies to

$$d_t = \frac{4R \cdot BPP}{d_R}. \tag{4.43}$$

Thus, our initial approach was indeed a specific case of the Gaussian model when far from the Rayleigh range, which may not always apply for an OPB system.

CHAPTER 5 Orbit-to-ground Lunar Optical Power Beaming

Building upon the ground-to-ground OPB system discussed in Chapter 4, this chapter transitions to an orbit-to-ground scenario, adapting the design considerations to accommodate the increased transmission distances and unique challenges associated with lunar orbital dynamics.

As mentioned in the literature review, high-intensity OPB has emerged when studying the energy transmission between SPS in orbit and ground-based stations. In the context of the Moon, this approach is particularly relevant because it provides a solution for continuous power supply during the lunar night. Solar photovoltaics can only operate during the day, requiring 336 hours of energy storage to cover the long lunar night [6]. Power beaming from a solar-powered orbiter, would therefore drastically reduce the need for energy storage technologies such as batteries or regenerative fuel cells.

In this Chapter, we will keep the same system model as in Chapter 4, but with some modifications in the optimization for this scenario. More specifically, we will present the changes in the overall design, as well as discuss the choice of orbit around the Moon.

5.1 System Model

In our system model, we analyze an orbit-to-ground power transmission, with distances ranging from hundreds of kilometers to several thousand kilometers, as illustrated in Figure 5.1. This approach aims to supply energy to lunar habitats, mostly during the long lunar night.

5.1.1 Energy Harvesting and Beam Propagation

The system model from Chapter 4 for energy harvesting and beam propagation will be kept, assuming a clear line of sight between the power transmitter and receiver. Therefore, the fundamental difference will be in our optimization, as the distances we are dealing with, here, are much greater than before. This increase of transmission distance will dictate our design choices. For the energy harvesting model, because of the long transmission distances, we include in our model the losses due to beam misalignment, as done in chapter 3, as

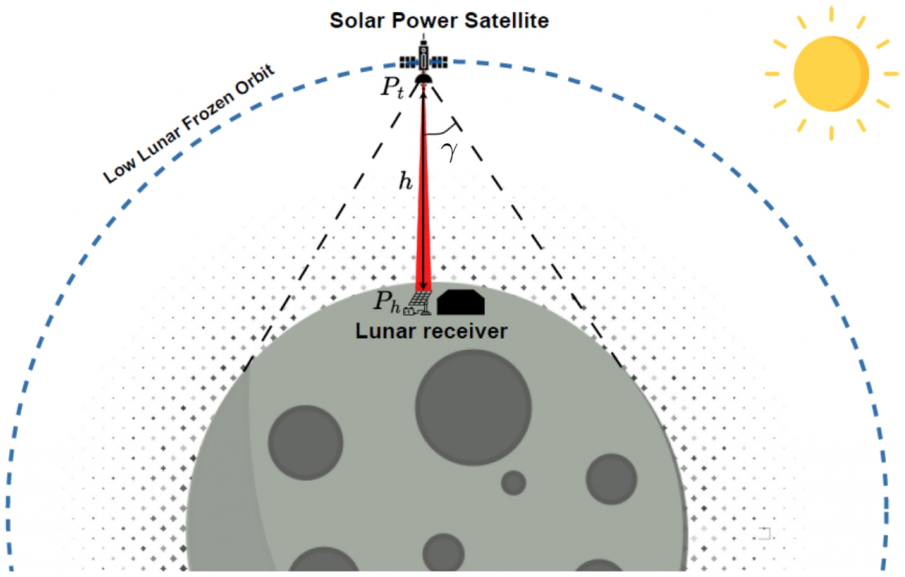

Figure 5.1 Orbit-to-ground lunar OPB. Here, Pt denotes the transmitted power, Pr represents the received power, h is the transmission distance, and γ is the half-opening angle.

$$P_h = \eta_{\text{Rx}} \cdot \eta_{\text{dust}} \cdot P_t \cdot \left(1 - e^{-2}\right) L_t(\psi_t) L_r(\psi_r). \tag{5.1}$$

with,

$$L_t = \exp(-G_t \psi_t^2), \tag{5.2}$$

$$L_r = \exp(-G_r \psi_r^2), \tag{5.3}$$

where the gain can be linked to the beam divergence angle.

Based on equation (4.8) and the parameters used in the previous section, namely an M^2 of 5.9 and a wavelength of 1064 nm, the graph linking the transmitter diameter to the receiver diameter for different distances is shown in Figure 5.2.

Due to spatial constraints on satellites, it is undesirable to have excessively large aperture sizes. Therefore, the primary focus in optimizing such systems is on minimizing the dimensions of both the transmitter and the receiver and, because of the fact that we are dealing with very long transmission distances, in most of the cases the optimal design would be to launch the beam as a perfectly collimated beam at the transmitter side.

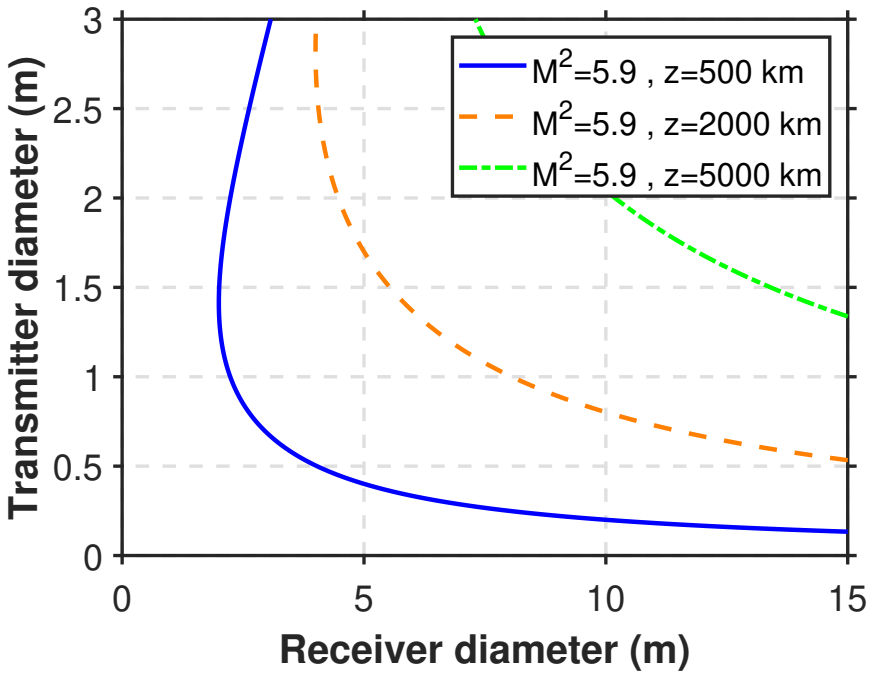

Figure 5.2 Transmitter diameter as a function of receiver diameter for various orbital distances, based on equation (4.8), for a collimated launched beam.

However, even if we don't need to focalize, we'll still need to use a telescope for beam expansion. The expansion can be achieved using metallic mirrors, equipped with optical coatings for the near-infrared (NIR) spectra. These coatings should exhibit very low scattering and absorption losses, approximately in the range of 10^{-5} to 10^{-4} [127]. Although lenses are commonly used, the telescope should be designed with mirrors instead, as they are better suited to the space environment. Lenses, besides being difficult to scale, would undergo significant degradation due to the high radiation levels in space, making mirrors a more appropriate choice for this application.

A good option found for this task is an unobstructed (off-axis) Cassegrain telescope, as illustrated in Figure 5.3, for beam expansion and collimation [128]. By eliminating the central obstruction and secondary mirror supports typical of traditional Cassegrain telescopes, the off-axis design yields a cleaner and more uniform beam profile, which is essential for efficient long-distance energy transfer. Moreover, this configuration minimizes scattered light and optical aberrations, thereby optimizing the collimation and intensity of the beam required for OPB [97]. Additionally, it allows for significant magnification while maintaining a compact

instrument design [129].

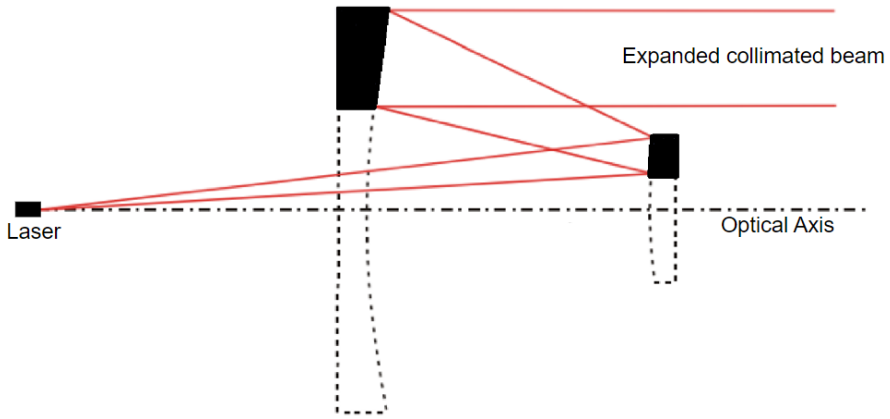

Figure 5.3 Unobscured cassegrain telescope configuration.

The magnification, which quantifies the desired expansion of the laser beam, is defined as follows

$$magnification = \frac{f_2}{f_1} = \frac{d_{tx}}{2r_o}, \tag{5.4}$$

where r_o is the output beam radius of the laser. Generally, it is recommended that the mirror diameters be slightly larger than the incident beam diameter to minimize aberrations and losses [130]. However, in theory, the mirrors must have a diameter at least equal to that of the incident beam.

5.1.2 Lunar Dust Attenuation Model

The same model, from the previous Chapter, will be taken with minor modifications that will be described in this section. The LLD studied in this section are high-altitude dust particles ejected by micrometeoroid impacts, as the phenomenon of electrostatically lifted particles is a near-surface phenomenon and can be neglected on this new optical path. First of all, the Bouguer-Beer-Lambert law is slightly modified to take account of the new optical path and is expressed as follows

$$\eta_{\text{dust}} = \exp\left(-\int_0^L \alpha(h)\, dh\right). \tag{5.5}$$

On the other hand, in this case, unlike the previous Chapter, normalized distribution of

equivalent-sphere radii is known for this phenomenon. Therefore, to account for the distribution of particle sizes, the average extinction per particle $\langle C_{\text{ext}} \rangle$ is calculated by integrating the orientation-averaged extinction over all possible sizes, weighted by the normalized distribution of equivalent-sphere radii $p(r)$. The formula is given by

$$\langle C_{\text{ext}} \rangle = \int_{r_{\min}}^{r_{\max}} dr\, p(r) \langle C_{\text{ext}}(r) \rangle, \tag{5.6}$$

where $\langle C_{\text{ext}}(r) \rangle$ is the orientation-averaged extinction cross section for a particle of radius r, and $p(r)$ is the normalized distribution of equivalent-sphere radii, satisfying the normalization condition

$$\int_{r_{\min}}^{r_{\max}} dr\, p(r) = 1. \tag{5.7}$$

To model the vertical distribution of dust particles ejected by micrometeoroid impacts, we apply an exponential decay model, which is commonly used in planetary exospheres [131] [17]. This model is based on data from the Lunar Dust Experiment (LDEX) aboard the LADEE mission, and it describes dust particle distributions for particles larger than 0.3 micrometers [124]. Using the upper limit of 142 particles/m^3 from the LADEE-UVS (Ultraviolet and Visible Spectrometer) for the surface density, we model the dust density distribution as a function of altitude. The scale height of 1000 meters is selected to reflect the decrease in dust density with altitude, as suggested by previous studies [132] [17].

For this phenomenon, the normalized distribution of particle sizes is given by the following equation [124]

$$p(r) = \frac{3\alpha}{r_{\min}^{-3\alpha} - r_{\max}^{-3\alpha}} r^{-(1+3\alpha)}, \tag{5.8}$$

where $\alpha = 0.9$. The particle radius ranges from $0.3\,\mu$m (the minimum size detected by the LDEX experiment) to $10\,\mu$m (beyond which the probability presence of particles is negligible) [124].

5.1.3 Lunar Frozen Orbit

A lunar frozen orbit is a special type of orbit where key orbital parameters, such as eccentricity and argument of periapsis, remain nearly constant over time. These orbits are particularly valuable because they offer natural stability, minimizing the need for station-keeping maneu-

vers, which can be costly and complex for satellite missions. However, such orbits are not easy to find, only a limited number of stable frozen orbits exist around the Moon due to its uneven gravitational field, heavily influenced by mascons (mass concentrations beneath the lunar surface).

As mentioned previously, for the purpose of designing a feasible power transmission system meeting SWaP constraints, keeping the sizes of both the transmitter and the receiver within reasonable limits is essential. To achieve this, we aim to find a low-altitude lunar frozen orbit that balances stability with proximity to the lunar surface. Indeed, a lower altitude allows for shorter transmitter and receiver aperture diameter. While frozen orbits at lower altitudes are more sensitive to perturbations from lunar mascons, they provide a practical solution for optimizing the overall system design. This is why studies such as [133] and [134] have focused on identifying these orbits, despite the added complexity of their dynamic models at lower altitudes.

In our research, we have identified a frozen orbit at approximately 100 km altitude, which we will further analyze. The parameters of this orbit are as follows [134]:

$$a = 1860.52\,\text{km}, \quad e = 0.0359457, \quad i = 90^\circ, \quad \omega = 270^\circ, \quad \Omega = 0^\circ, \quad \nu = 0^\circ.$$

where a represents the semi-major axis of the orbit, e is the orbital eccentricity, i denotes the orbital inclination relative to the lunar equator, ω is the argument of perigee, Ω is the right ascension of the ascending node, and ν is the true anomaly at epoch. This orbit provides a stable configuration while keeping transmitter and receiver sizes manageable.

5.2 Performance Evaluation

5.2.1 Simulations Parameters

In our scenario, we consider a fixed distance of approximately 100 km based on the orbit parameters presented in the previous section. Moreover, we will maintain the laser parameters used in the previous Chapter, namely a BPP of 2 mm·mrad (corresponding to an M^2 of 5.9), a wavelength of 1064 nm, and fix the transmitted power at 5 kW. The design choices will be presented, followed by the calculation of the harvested power during each revolution of the transmitter SPS satellite in a low lunar frozen orbit using Ansys STK. The parameters are summarized in Table 5.1.

Table 5.1 Summary of Parameters: Orbit-to-Ground Scenario.

Parameter	**Value**
Transmission Range	100 km
Transmitted Power	5 kW
Particle Size Range	0.3 to 10 μm
Particle Complex Refractive Index	$1.733 + i\,0.05$
Particle Average Aspect Ratio	1.4286
Medium Refractive Index	1.0
Laser Wavelength (λ)	1064 nm [135]
BPP	2 mm·mrad ($M^2 = 5.9$)
EHCE	45.5% [126]

5.2.2 Results and Discussions

For this scenario, we assume the receiver is placed at a sufficient height to neglect the influence of electrostatic dust lofting. Thus, only the effect of dust ejecta in the lunar exosphere is taken into account. Although the studied particle size range is larger and contributes more significantly to the extinction cross-section, the particle density from this phenomenon is not enough to attenuate the laser intensity, as shown in Figure 5.4. Therefore, to evaluate the harvested power, we will assume $\eta_{\text{dust}} \approx 1$. we will also assume no losses due to beam misalignment, because of the relatively short transmission distance used ($\approx$ 100km).

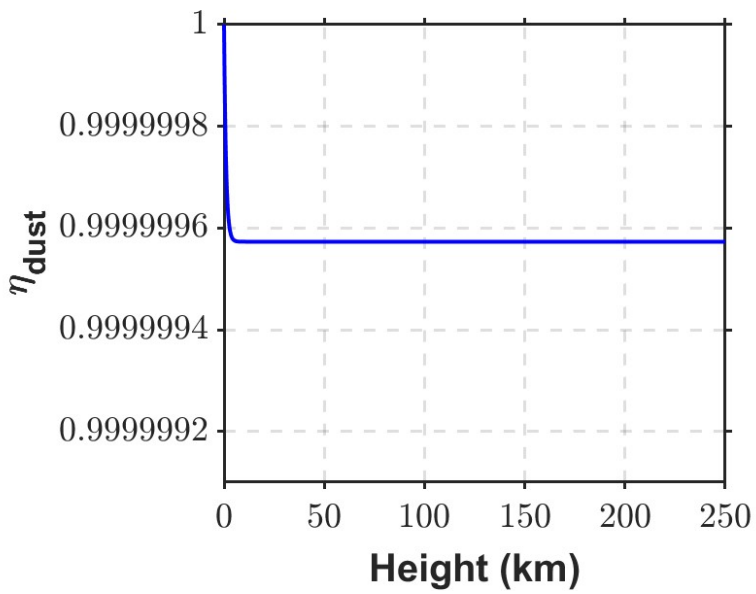

Figure 5.4 Dust-related optical transmission efficiency as a function of height in the orbit-to-ground scenario.

With this result, we will now study a constellation of three SPS in low lunar frozen orbits around the Moon. Using ANSYS STK software, we evaluated the amount of energy that can be harvested to assess feasibility, as shown in Figure 5.5. In this simulation, we assume a transmission cone designed to maximize coverage without exceeding the lunar surface. For the selected orbit, the half-opening angle γ is set at 75 degrees. The system operates based on the parameters summarized in Table 5.1.

We analyze a scenario of energy harvesting on the Moon, where an SPS constellation transmits power every two hours (corresponding to one full revolution). The harvested power per orbit is illustrated in Figure 5.6. The objective is to evaluate the total amount of energy harvested over the course of one Earth day and a full lunar revolution, assess feasibility, and explore potential system improvements to increase the harvested power.

Considering the 3 SPS constellation evenly distributed such as

$$\nu_k = \nu_1 + \frac{2\pi(k-1)}{N_{\text{satellites}}}, \tag{5.9}$$

where k indicates the k-th satellite and ν represents the true anomaly. The average power harvested per Earth day is 0.37 kW, resulting in a total of 8.88 kWh of energy collected

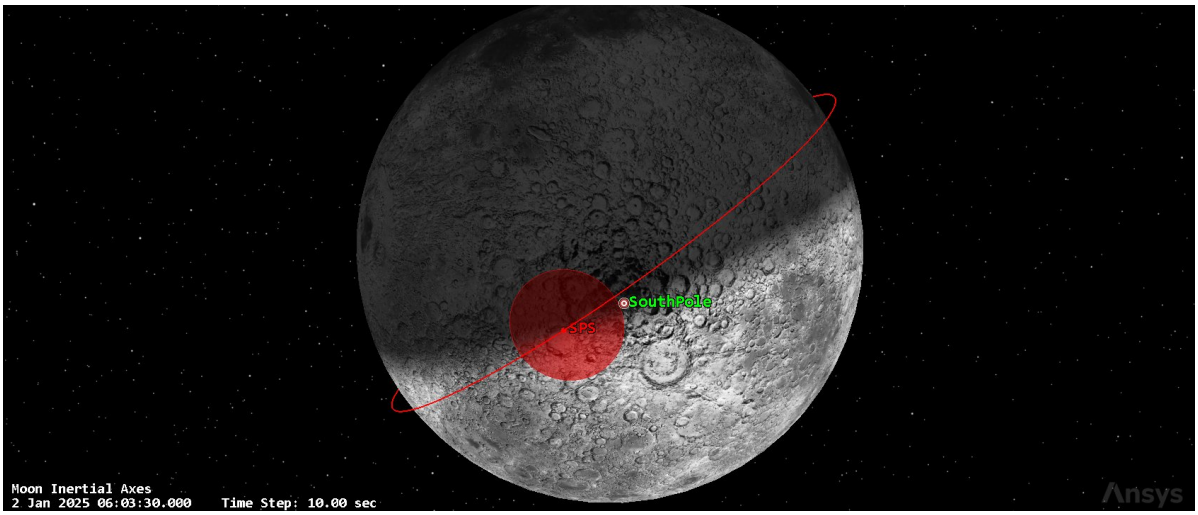

(a) Low lunar frozen orbit : 3D view

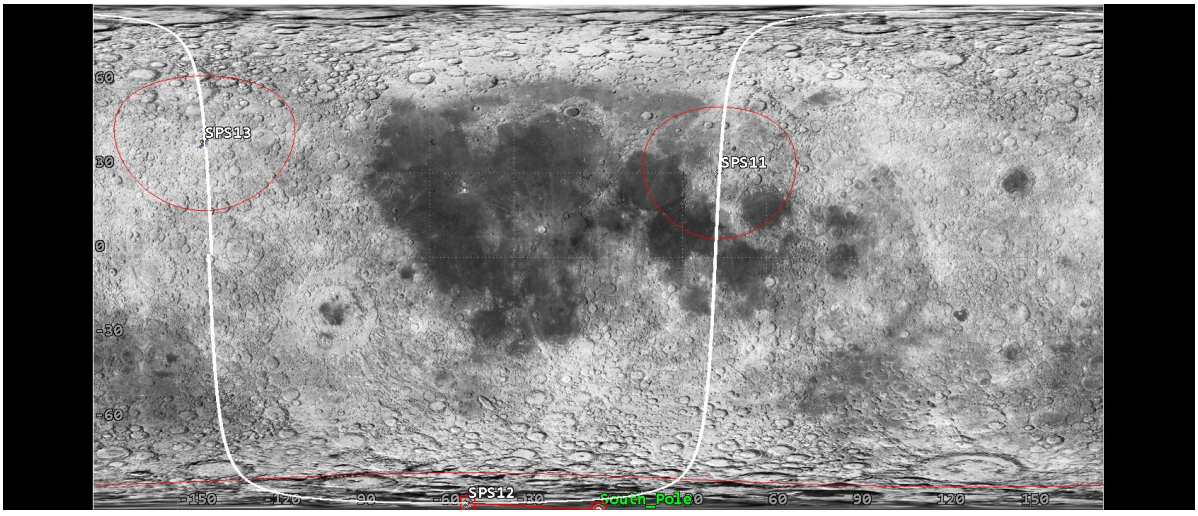

(b) 2D view

Figure 5.5 Constellation of three SPS in low lunar frozen orbit, with a half-opening angle α of 75°.

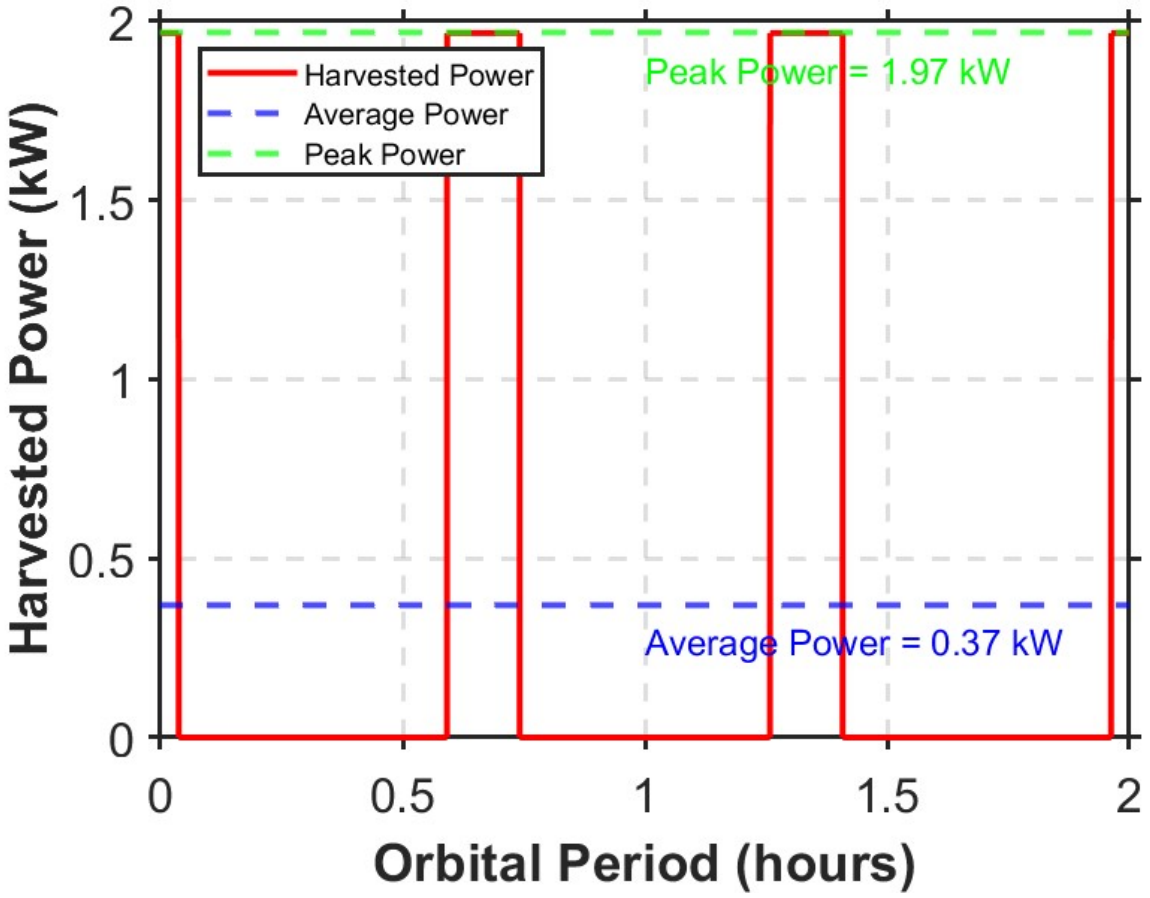

Figure 5.6 Harvested power by a receiver in the lunar south pole as a function of orbital period for a 3-SPS constellation in a low lunar orbit.

daily. Over the course of a full lunar revolution (approximately 29.53 Earth days), this accumulates to 262.6 kWh. While this amount of energy is sufficient to power basic systems such as low-power LED lighting, communication devices, and small electronics, it falls short of supporting critical life-sustaining systems, such as heating, oxygen production, systems necessary for a sustained human presence on the Moon.

In order to increase the harvested power, we could enhance beam coverage by either increasing the number of satellites or raising the orbital altitude of the satellite. Indeed, continuous coverage would provide a more consistent and higher energy supply, but this improvement involves trade-offs. Elevating satellites to higher orbits requires larger receiver and transmitter apertures to maintain efficiency over greater distances, as previously discussed. This necessity leads to an increase in the physical dimensions of satellite components, which subsequently

adds weight and demands more robust structural support. The added mass can push the satellite beyond payload limitations, necessitating more powerful launch vehicles and thus escalating mission costs. Similarly, increasing the number of satellites to achieve enhanced coverage results in higher aggregate size and weight for the satellite constellation. Each additional satellite, though potentially smaller on its own, contributes to the cumulative material used, affecting the overall weight and complexity of the system. This not only increases manufacturing and launch expenses but also adds to operational costs over the satellite's lifespan. Thus, while improving beam coverage can boost the harvested power and provide a more reliable energy supply, it must be balanced against SWaP constraints when designing.

In our scenario, if continuous coverage is achieved, the average harvested power would increase to 1.97 kW. This would result in 47.28 kWh of power harvested per Earth day, and over a full lunar revolution, the total power would amount to 1396 kWh. This substantial increase in power capacity would enable the operation of life support systems, such as thermal regulation, oxygen production, and power support for larger scientific infrastructures.

5.3 Conclusions

This study highlights the potential of OPB for providing continuous power during the prolonged lunar night. By analyzing an orbit-to-ground transmission system, the research identifies the non-influence of lunar dust and the necessity of optimizing transmitter and receiver sizes to maintain manageable beam diameters and minimal beam spread, as well as the need for orbital stability using a low-altitude lunar frozen orbit. Moreover, simulations using Ansys STK software evaluate the performance of a constellation of three SPS at approximately 100 km. The findings reveal that, under this design constraints, the average power harvested per Earth day is 0.37 kW, totaling 8.88 kWh daily insufficient for supporting essential life-sustaining systems on the lunar surface.

To enhance the harvested power, we could increase beam coverage by adding more satellites or by carefully selecting higher orbital altitudes that offer better coverage while keeping aperture sizes within practical limits. Achieving continuous coverage could raise the average harvested power to 1.97 kW and the daily harvested energy to 47.28 kWh, amounting to 1396 kWh over a full lunar revolution. This increase would enable the operation of life support systems and support extended exploration missions. However, these solutions involve trade-offs concerning SWaP constraints, potentially escalating mission complexity and cost.

As a conclusion, the research underscores the feasibility of orbit-to-ground OPB as a means to reduce reliance on extensive energy storage during the lunar night. Nevertheless, it also highlights the challenges posed by technical limitations and the need for careful balancing of design parameters to optimize system performance while managing practical constraints.

CHAPTER 6 CONCLUSIONS

6.1 Summary

The central questions of this thesis were to determine whether lunar lofted dust significantly affects high-power optical transmissions in optical power beaming systems on the Moon, and how to optimize these systems to deliver power efficiently while adhering to size, weight, and power constraints in the lunar environment. These questions were analyzed for two specific scenarios: ground-to-ground and orbit-to-ground transmissions.

Through comprehensive theoretical analysis and simulation-based studies, we have demonstrated that, although LLD can attenuate optical power transmission near the lunar surface, particularly in illuminated regions for ground-to-ground links, suitable design choices could effectively mitigate these impacts. In contrast, in dark regions, LLD tends to have a negligible impact, making optical power beaming more suitable in these areas. Additionally, we observed that multiple kilowatts of energy harvesting are possible with current technology. By carefully selecting the focal length, we have shown that it is possible to optimize the transmission distance, further enhancing system performance.

For orbit-to-ground scenarios, our findings indicate that the impact of lofted lunar dust is also negligible. We observed that achieving good orbital coverage is essential for efficient energy harvesting performance. For beam propagation in these scenarios, we demonstrated that launching a collimated beam at the transmitter is sufficient in most cases; however, a telescope is still required for beam expansion to ensure optimal energy delivery.

The research process involved iterative modeling and simulation, reflecting on the limitations of initial approaches and progressively refining the system model. The model was improved by incorporating Gaussian beam theory for energy harvesting and beam propagation, and the T-matrix method for dust attenuation. Thermal management considerations were also addressed, given that radiative cooling is the only viable heat dissipation mechanism on the Moon. By integrating these considerations together, we were able to provide recommendations for optimizing the system's SWaP.

In conclusion, this research fills a critical gap in understanding the interplay between lunar

dust and OPB systems. It confirms that, with optimized design and strategic planning, OPB is a viable and efficient solution for providing reliable power on the Moon. By addressing SWaP constraints, our work contributes valuable insights to the field. This lays a foundation for future advancements in OPB technology, supporting sustained human and robotic presence on the Moon for exploration and habitation in space.

6.2 Limitations and Future Work Suggestions

The first area of improvement in this work would be to consider a more complex and realistic scenario for the optical path. In the current model, the surface between the transmitter and receiver is assumed to be flat, with the optical path at a height h parallel to this surface. While this assumption is accurate for relatively short transmission distances, as the transmission distance increases, the curvature of the Moon becomes more significant, introducing a dependency of the optical path on h.

Next, in terms of optics, several improvements could be made. First, it would be relevant to explore other beam profiles, such as super-Gaussian or Bessel-Gauss beams. Super-Gaussian beams would allow for a more uniform beam distribution on the receivers, reducing losses and improving energy harvesting efficiency, while Bessel-Gauss beams, known for their resistance to diffraction, could maintain beam quality over longer distances. Additionally, it could also be relevant to study the coherent and incoherent combination of multiple lasers to create a single higher-power beam that would further increase the transmitted power.

On the other hand, future work could also focus on improving heat dissipation techniques. Current research includes improving the surfaces of cooling components with specific geometric patterns to enhance heat transfer efficiency, as demonstrated by ongoing studies like [136]. Such innovations could lead to more effective thermal management solutions, enabling the design of more compact receivers suitable for lunar applications.

Additionally, the lunar dust model employed in this study could be refined by considering more sophisticated shapes of lunar dust particles and utilizing finite element methods for more accurate representation. However, given the random nature of dust particle shapes and the increasing complexity of advanced computational methods, this approach may have practical limitations. We therefore recommend that subsequent research focus on experimental validation of OPB systems under lunar-like conditions. Conducting experiments using

lunar dust simulant in controlled environments that mimic the lunar exosphere could provide empirical data to quantify the attenuation of laser beams due to dust lofting.

Finally, the safety and planetary protection issues of high-power optical beam transmission must also be addressed. For instance, if a high-power laser misaligns and misses its target in a Permanently Shadowed Region (PSR), it could vaporize the very volatiles being sought in that region. To mitigate such risks, precise tracking systems and robust safety mechanisms are essential. Notably, PowerLight Technologies has demonstrated a safety system capable of shutting off the laser when an object enters the line of sight, providing a potential solution to prevent unintended harm. Future research should also explore the development of comprehensive guidelines and regulations to manage the ethical and practical challenges of deploying high-power optical systems in extraterrestrial environments.

REFERENCES

[1] S. I. Popel, L. M. Zelenyi, and B. Atamaniuk, "Dusty plasma sheath-like structure in the region of lunar terminator," *Physics of Plasmas*, vol. 22, no. 12, 2015.

[2] S. i. Army, Official Web-site of the United States, "Combined-fiber laser," feb 2018. [Online]. Available: https://commons.wikimedia.org/wiki/File:Combined-fiber_laser_diagram.jpg

[3] A. C. Debay. (2017) Mooning over measurement. NIST - National Institute of Standards and Technology. [Online]. Available: https://www.nist.gov/blogs/taking-measure/mooning-over-measurement

[4] Y. Lin *et al.*, "Return to the Moon: New perspectives on lunar exploration," *Science Bulletin*, vol. 69, no. 13, pp. 2136–2148, Jul. 2024.

[5] F. Lopez *et al.*, "Wireless power transmission: A new frontier for lunar colonisation development," in *2024 11th International Workshop on Metrology for AeroSpace (MetroAeroSpace)*, 2024, pp. 303–308.

[6] J. Grandidier *et al.*, "Power beaming for deep space and permanently shadowed regions," in *The 2nd Optical Wireless and Fiber Power Transmission Conference (OWPT2020)*, April 2020, pp. 21–23.

[7] A. Marcinkowski *et al.*, "Lunar surface power architecture concepts," in *2023 IEEE Aerospace Conference*, Mar. 2023, pp. 1–19.

[8] NASA. (2024) Weather on the moon. [Online]. Available: https://science.nasa.gov/moon/weather-on-the-moon/

[9] M. W. Stavnes, "An analysis of power beaming for the moon and mars," in *27th Intersociety Energy Conversion Engineering Conference*, Aug. 1992.

[10] T. J. Nugent, Jr. and J. T. Kare, "Laser power beaming for defense and security applications," in *SPIE Defense, Security, and Sensing*, D. W. Gage *et al.*, Eds., May 2011, p. 804514.

[11] T. Nayfeh *et al.*, "High intensity laser power beaming architecture for space and terrestrial missions," in *Advanced Space Propulsion Workshop*, no. NASA/TM-2011-217009, March 2011.

[12] M. Qaraqe *et al.*, "Power hotspots in space: Powering cubesats via inter-satellite optical wireless power transfer," *IEEE Internet of Things Magazine*, vol. 5, no. 3, pp. 180–185, 2022.

[13] M. Tisdale *et al.*, "Design of a modular and orientable electrodynamic shield for lunar dust mitigation," in *AIAA SCITECH Forum*, 2022, p. 2623.

[14] M. Horányi, J. R. Szalay, and X. Wang, "The lunar dust environment: concerns for moon-based astronomy," *Philosophical Transactions of the Royal Society A*, vol. 382, no. 2271, p. 20230075, 2024.

[15] L. M. Zelenyi, S. I. Popel, and A. V. Zakharov, "Dusty plasma at the moon. challenges of modeling and measurements," *Plasma Physics Reports*, vol. 46, pp. 527–540, 2020.

[16] M. Naqbi, S. Loranger, and G. Karabulut Kurt, "Impact of lunar dust on free space optical (fso) energy harvesting," in *2024 IEEE Aerospace Conference*. IEEE, March 2024, pp. 1–9.

[17] J. R. Szalay *et al.*, "Impact ejecta and gardening in the lunar polar regions," *Journal of Geophysical Research: Planets*, vol. 124, no. 1, pp. 143–154, 2019.

[18] J. E. Colwell *et al.*, "Lunar surface: Dust dynamics and regolith mechanics," *Reviews of Geophysics*, vol. 45, no. 2, 2007.

[19] S. Popel *et al.*, "Lunar dust and dusty plasmas: Recent developments, advances, and unsolved problems," *Planetary and Space Science*, vol. 156, pp. 71–84, Jul. 2018.

[20] R. A. Parker *et al.*, "Apollo 17 Preliminary Science Report," Jan. 1973, patent number: LC-73-600152, NTRS document ID: 19740010315.

[21] National Research Council *et al.*, Eds., *The scientific context for exploration of the Moon*. Washington, D.C.: National Academies Press, 2007.

[22] D. B. J. Bussey *et al.*, "Illumination conditions of the south pole of the moon derived using kaguya topography," *Icarus*, vol. 208, no. 2, pp. 558–564, August 2010.

[23] S. Nozette *et al.*, "The Clementine Bistatic Radar Experiment," *Science*, vol. 274, no. 5292, pp. 1495–1498, nov 1996.

[24] I. G. Mitrofanov *et al.*, "Hydrogen mapping of the lunar south pole using the lro neutron detector experiment lend," *Science*, vol. 330, no. 6003, pp. 483–486, 2010.

[25] R. L. Fergason, P. R. Christensen, and H. H. Kieffer, "High-resolution thermal inertia derived from the thermal emission imaging system (themis): Thermal model and applications," *Journal of Geophysical Research: Planets*, vol. 111, no. E12, 2006.

[26] R. G. Schunk, S. D. Babiak, and B. W. Evans, "Thermal Control System Architecture and Technology Challenges for a Lunar Surface Habitat," in *IEEE Aerospace Conference (AERO)*, Big Sky, MT, USA, mar 2022, pp. 1–8.

[27] J. J. Rennilson and D. R. Criswell, "Surveyor observations of lunar horizon-glow," *The Moon*, vol. 10, no. 2, pp. 121–142, 1974.

[28] J. E. McCoy and D. R. Criswell, *Evidence for a high altitude distribution of lunar dust.* Pergamon Press, 1974.

[29] D. A. Glenar *et al.*, "A reanalysis of the apollo light scattering observations, and implications for lunar exospheric dust," *Planetary and Space Science*, vol. 59, no. 14, pp. 1695–1707, 2011.

[30] M. Horányi *et al.*, "A permanent, asymmetric dust cloud around the moon," *Nature*, vol. 522, no. 7556, pp. 324–326, 2015.

[31] T. J. Stubbs, R. R. Vondrak, and W. M. Farrell, "A dynamic fountain model for lunar dust," *Advances in Space Research*, vol. 37, no. 1, pp. 59–66, jan 2006.

[32] S. I. Popel *et al.*, "Dusty plasma at the surface of the moon," *Solar System Research*, vol. 47, no. 6, pp. 419–429, nov 2013.

[33] P. B. Abel *et al.*, "Lunar dust mitigation: A guide and reference," Tech. Rep. E-20102, 2023.

[34] T. Wriedt, "Mie theory: a review," in *The Mie theory: Basics and applications*, 2012, pp. 53–71.

[35] P. C. Waterman, "Matrix formulation of electromagnetic scattering," *Proceedings of the IEEE*, vol. 53, no. 8, pp. 805–812, 1965.

[36] M. I. Mishchenko, L. D. Travis, and D. W. Mackowski, "T-matrix computations of light scattering by nonspherical particles: A review," *Journal of Quantitative Spectroscopy and Radiative Transfer*, vol. 55, no. 5, pp. 535–575, 1996.

[37] J. W. S. B. Rayleigh, *On the scattering of light by small particles*, 1871.

[38] H. C. Hulst and H. C. van de Hulst, *Light scattering by small particles*. Courier Corporation, 1981.

[39] B. T. Draine and P. J. Flatau, "Discrete-dipole approximation for scattering calculations," *JOSA A*, vol. 11, no. 4, pp. 1491–1499, 1994.

[40] S. Chandrasekhar, *Radiative Transfer*. Dover Publications, 1960.

[41] X. Lu *et al.*, "Wireless charging technologies: Fundamentals, standards, and network applications," *IEEE Communications Surveys & Tutorials*, vol. 18, no. 2, pp. 1413–1452, 2016.

[42] A. Costanzo *et al.*, "Electromagnetic energy harvesting and wireless power transmission: A unified approach," *Proceedings of the IEEE*, vol. 102, no. 11, pp. 1692–1711, 2014.

[43] A. Kurs *et al.*, "Wireless power transfer via strongly coupled magnetic resonances," *Science*, vol. 317, no. 5834, pp. 83–86, 2007.

[44] S. Li and C. C. Mi, "Wireless power transfer for electric vehicle applications," *IEEE Journal of Emerging and Selected Topics in Power Electronics*, vol. 3, no. 1, pp. 4–17, 2014.

[45] N. Shinohara, "Beam efficiency of wireless power transmission via radio waves from short range to long range," *Journal of Electromagnetic Engineering and Science*, vol. 10, no. 4, pp. 224–230, 2010.

[46] D. H. Rhee and S. M. Kim, "Study on a laser wireless power charge technology," *The Journal of the Korea Institute of Electronic Communication Sciences*, vol. 11, no. 12, pp. 1219–1224, 2016.

[47] W. Jaafar and H. Yanikomeroglu, "Dynamics of laser-charged UAVs: A battery perspective," *IEEE Internet of Things Journal*, vol. 8, no. 13, pp. 10 573–10 582, 2020.

[48] C. R. Teeneti *et al.*, "Review of wireless charging systems for autonomous underwater vehicles," *IEEE Journal of Oceanic Engineering*, vol. 46, no. 1, pp. 68–87, 2019.

[49] S. M. Kim and S. M. Kim, "Wireless optical energy transmission using optical beamforming," *Optical Engineering*, vol. 52, no. 4, pp. 043 205–043 205, 2013.

[50] Q. Zhang *et al.*, "Distributed laser charging: A wireless power transfer approach," *IEEE Internet of Things Journal*, vol. 5, no. 5, pp. 3853–3864, 2018.

[51] ——, "Adaptive distributed laser charging for efficient wireless power transfer," in *IEEE Vehicular Technology Conference (VTC-Fall)*, September 2017, pp. 1–5.

[52] P. D. Diamantoulakis, G. K. Karagiannidis, and Z. Ding, "Simultaneous lightwave information and power transfer (slipt)," *IEEE Transactions on Green Communications and Networking*, vol. 2, no. 3, pp. 764–773, 2018.

[53] M. D. Williams and E. J. Conway, "Space laser power transmission system studies," NASA, Tech. Rep. L-15030, 1982.

[54] R. J. De Young, "Preliminary design and cost of a 1-megawatt solar-pumped iodide laser," Space-to-Space Transmission Station, Tech. Rep., 1987.

[55] J. T. Kare, "Program and applications for a near-term laser launch system," Lawrence Livermore National Lab. (LLNL), Livermore, CA, United States, Tech. Rep. UCID-21718, 1989.

[56] L. C. Olsen *et al.*, "Gaas solar cells for laser power beaming," in *NASA. Lewis Research Center, Space Photovoltaic Research and Technology Conference*, August 1991.

[57] S. Van Riesen, U. Schubert, and A. W. Bett, "Gaas photovoltaic cells for laser power beaming at high power densities," in *Proc. 17th Eur. PV Solar Energy Conf*, October 2001, pp. 18–21.

[58] J. T. Kare, F. Mitlitsky, and A. Weisberg, "Preliminary demonstration of power beaming with non-coherent laser diode arrays," in *AIP Conference Proceedings*, vol. 458, no. 1. American Institute of Physics, January 1999, pp. 1641–1646.

[59] D. E. Raible, "High-intensity laser power beaming for long-range wireless power transmission," in *Proceedings of SPIE*, vol. 7005, 2008, p. 70051F.

[60] NASA Administrator. (2009) Lasermotive wins $900,000 from nasa in space elevator games. NASA. [Online]. Available: http://www.nasa.gov/centers/dryden/status_reports/power_beam.html

[61] (2012) Laser powers lockheed martin's stalker uas for 48 hours. Lockheed Martin. [Online]. Available: https://news.lockheedmartin.com/2012-07-11-Laser-Powers-Lockheed-Martins-Stalker-UAS-For-48-Hours

[62] T. He *et al.*, "High-power high-efficiency laser power transmission at 100 m using optimized multi-cell gaas converter," *Chinese Physics Letters*, vol. 31, no. 10, p. 104203, 2014.

[63] M. C. York and S. Fafard, "High efficiency phototransducers based on a novel vertical epitaxial heterostructure architecture (vehsa) with thin p/n junctions," *Journal of Physics D: Applied Physics*, vol. 50, no. 17, p. 173003, 2017.

[64] U.S. Naval Laboratory, "Researchers transmit energy with laser in historic power beaming demonstration," https://www.nrl.navy.mil/Media/News/Article/2504007/researchers-transmit-energy-with-laser-in-historic-power-beaming-demonstration/, 2019.

[65] Ericsson and PowerLight Technologies, "Ericsson and powerlight base station wireless charging breakthrough," https://www.ericsson.com/en/news/2021/10/ericsson-and-powerlight-achieve-base-station-wireless-charging-breakthrough, 2021.

[66] U.S. Naval Research Laboratory, "First in-space laser power beaming experiment," https://www.nrl.navy.mil, 2023.

[67] M. Röhner *et al.*, "Fiber-coupled high-power diode-lasers with highest radiance," in *2013 High Power Diode Lasers and Systems Conference (HPD)*. IEEE, October 2013, pp. 36–37.

[68] D. McCormick *et al.*, "Ultra-narrow spectral linewidth diode lasers for the pumping of alkalis," in *2015 IEEE High Power Diode Lasers and Systems Conference (HPD)*. IEEE, October 2015, pp. 25–26.

[69] R. K. Huang *et al.*, "Recent progress on high-brightness kw-class direct diode lasers," in *2015 IEEE High Power Diode Lasers and Systems Conference (HPD)*. IEEE, Oct. 2015, pp. 29–30.

[70] N. Platonov *et al.*, "High-efficient kw-level single-mode ytterbium fiber lasers in all-fiber format with diffraction-limited beam at wavelengths in 1000-1030 nm spectral range," in *Fiber Lasers XVII: Technology and Systems*. SPIE, 2020, p. 1126003.

[71] I. Photonics, "High power fiber lasers," https://www.ipgphotonics.com/products/lasers/industrial-cw-fiber-lasers/high-power-fiber-lasers, 2024.

[72] B. Donmez, I. Azam, and G. Karabulut Kurt, "Mitigation of misalignment errors over inter-satellite FSO energy harvesting," Jul 2023.

[73] B. E. A. Saleh and M. C. Teich, *Fundamentals of Photonics*. John Wiley & Sons, 2019.

[74] J. L. Merz *et al.*, "Gaas double-heterostructure photodetectors," *Journal of Applied Physics*, vol. 48, no. 8, pp. 3580–3587, 1977.

[75] L. C. Olsen *et al.*, "High efficiency monochromatic gaas solar cells," in *The Conference Record of the Twenty-Second IEEE Photovoltaic Specialists Conference-1991.* IEEE, October 1991, pp. 419–424.

[76] H. Helmers *et al.*, "68.9% efficient gaas-based photonic power conversion enabled by photon recycling and optical resonance," *physica status solidi (RRL)–Rapid Research Letters*, vol. 15, no. 7, p. 2100113, 2021.

[77] S. Fafard and D. P. Masson, "74.7% efficient gaas-based laser power converters at 808 nm at 150 k," *Photonics*, vol. 9, no. 8, 2022.

[78] N. A. Kalyuzhnyy *et al.*, "Optimization of photoelectric parameters of ingaas metamorphic laser ($\lambda = 1064$ nm) power converters with over 50% efficiency," *Solar Energy Materials and Solar Cells*, vol. 217, p. 110710, 2020.

[79] P. Sprangle *et al.*, "High-power lasers for directed-energy applications," *Applied Optics*, vol. 54, no. 31, pp. F201–F209, 2015.

[80] Y. Gou *et al.*, "High-performance laser power converts for direct-energy applications," *Optics Express*, vol. 30, no. 17, pp. 31 509–31 517, 2022.

[81] S. Reich *et al.*, "Continuous wave high-power laser propagation in water is affected by strong thermal lensing and thermal blooming already at short distances," *Scientific Reports*, vol. 11, no. 1, p. 22619, 2021.

[82] A. Su *et al.*, "Analytical study on the steady-state thermal blooming effect of high-power ytterbium-doped fiber lasers propagating through the atmosphere," *Optics Express*, vol. 31, no. 9, pp. 13 640–13 653, 2023.

[83] M. Xian-long *et al.*, "Multi-field coupling characteristics of photovoltaic cell under non-uniform laser beam irradiance," *Sustainable Energy Technologies and Assessments*, vol. 52, p. 101963, 2022.

[84] M. Kumar, A. Khandelwal, and S. Azeemuddin, "Performance evaluation of incoherent beam combination system based on different beam directing mechanisms," *Optical and Quantum Electronics*, vol. 55, no. 12, p. 1034, 2023.

[85] D. Naidoo, I. A. Litvin, and A. Forbes, "Brightness enhancement in a solid-state laser by mode transformation," *Optica*, vol. 5, no. 7, pp. 836–843, 2018.

[86] Z. Ghassemlooy, J. Perez, and E. Leitgeb, "On the performance of fso communications links under sandstorm conditions," in *Proceedings of the 12th International Conference on Telecommunications*. IEEE, June 2013, pp. 53–58.

[87] M. Ando *et al.*, "On-orbit demonstration of oscillating heat pipe with check valves for space application," *Applied Thermal Engineering*, vol. 130, pp. 552–560, 2018.

[88] A. P. C. Cuco *et al.*, "Multi-objective design optimization of a new space radiator," *Optimization and Engineering*, vol. 12, pp. 393–406, 2011.

[89] M. A. Fernandes *et al.*, "Adaptive optical beam alignment and link protection switching for 5g-over-fso," *Optics Express*, vol. 29, no. 13, pp. 20 136–20 149, 2021.

[90] R. Lolachi, D. A. Glenar, and T. J. Stubbs, "Optical monitoring of the dust environment at lunar surface exploration sites," *Planetary and Space Science*, vol. 234, p. 105709, 2023.

[91] K.-J. Kim and K.-H. Yu, "Multidisciplinary design optimization for a solar-powered exploration rover considering the restricted power requirement," *Energies*, vol. 13, no. 24, p. 6652, January 2020. [Online]. Available: https://www.mdpi.com/1996-1073/13/24/6652

[92] R. Harada *et al.*, "Adaptive beam divergence for expanding range of link distance in fso with moving nodes toward 6g," *IEEE Photonics Technology Letters*, vol. 34, no. 20, pp. 1061–1064, 2022.

[93] G. Pan *et al.*, "Space simultaneous information and power transfer: An enhanced technology for miniaturized satellite systems," *IEEE Wireless Communications*, vol. 30, no. 2, pp. 122–129, 2023.

[94] H. Kotake *et al.*, "Link budget design of adaptive optical satellite network for integrated non-terrestrial network," in *IEEE International Conference on Space Optical Systems and Applications (ICSOS)*, 2022, pp. 240–247.

[95] A. Polishuk and S. Arnon, "Optimization of a laser satellite communication system with an optical preamplifier," *J. Opt. Soc. Am. A*, vol. 21, no. 7, pp. 1307–1315, Jul 2004.

[96] A. G. Alkholidi and K. S. Altowij, "Free Space Optical Communications — Theory and Practices," in *Contemporary Issues in Wireless Communications*, M. Khatib, Ed., Rijeka, 2014.

[97] M. Born and E. Wolf, *Principles of Optics: Electromagnetic Theory of Propagation, Interference and Diffraction of Light*, 7th ed. Cambridge: Cambridge University Press, 1999.

[98] C. F. Bohren and D. R. Huffman, "Absorption and scattering by a sphere," in *Absorption and Scattering of Light by Small Particles*. John Wiley & Sons, Ltd, 1998, pp. 82–129.

[99] Y. Liu *et al.*, "Characterization of lunar dust for toxicological studies. II: Texture and shape characteristics," *Journal of Aerospace Engineering*, vol. 21, no. 4, pp. 272–279, October 2008.

[100] T. Wriedt, "Mie theory: A review," in *The Mie Theory: Basics and Applications*, ser. Springer Series in Optical Sciences, W. Hergert and T. Wriedt, Eds. Berlin, Heidelberg: Springer, 2012, pp. 53–71.

[101] O. B. Yahia *et al.*, "Haps selection for hybrid RF/FSO satellite networks," *IEEE Transactions on Aerospace and Electronic Systems*, vol. 58, no. 4, pp. 2855–2867, August 2022.

[102] B. Lacaze, "Gaps of free-space optics beams with the beer-lambert law," *Applied Optics*, vol. 48, no. 14, p. 2702, May 2009.

[103] A. Vidwans *et al.*, "Size and charge distribution characteristics of fine and ultrafine particles in simulated lunar dust: Relevance to lunar missions and exploration," *Planetary and Space Science*, vol. 210, p. 105392, Jan. 2022.

[104] A. Fearnside, P. Masding, and C. Hooker, "Polarimetry of moonlight: A new method for determining the refractive index of the lunar regolith," *Icarus*, vol. 268, pp. 156–171, Apr. 2016.

[105] J. D. Goguen *et al.*, "A new look at photometry of the moon," *Icarus*, vol. 208, no. 2, pp. 548–557, Aug. 2010.

[106] B. T. Draine and H. M. Lee, "Optical properties of interstellar graphite and silicate grains," *The Astrophysical Journal*, vol. 285, p. 89, Oct. 1984.

[107] J. Park *et al.*, "Characterization of lunar dust for toxicological studies i: Particle size distribution," *Journal of Aerospace Engineering*, vol. 21, no. 4, pp. 266–271, oct 2008.

[108] H. Kaushal and G. Kaddoum, "Optical communication in space: Challenges and mitigation techniques," *IEEE Communications Surveys & Tutorials*, vol. 19, no. 1, pp. 57–96, jan 2017.

[109] H.-Y. Lin *et al.*, "Compact Nd:YVO4 laser 1087.5 nm pumped by an edge-emitting LD," *Optik*, vol. 185, pp. 414–417, jan 2019.

[110] A. Luque and S. Hegedus, *Handbook of Photovoltaic Science and Engineering*, 2nd ed. Chichester, West Sussex, U.K.: Wiley, 2011.

[111] C. Algora *et al.*, "Beaming power: Photovoltaic laser power converters for power-by-light," *Joule*, vol. 6, no. 2, pp. 340–368, 2022.

[112] J. Grandidier *et al.*, "Laser power beaming for lunar night and permanently shadowed regions," *Jet Propulsion*, vol. 818, pp. 354–1566, 2021.

[113] R. Jomen *et al.*, "Conversion efficiencies of single-junction III–V solar cells based on InGaP, GaAs, InGaAsP, and InGaAs for laser wireless power transmission," *Japanese Journal of Applied Physics*, vol. 57, no. 8S3, jul 2018.

[114] H. T. Friis, "A note on a simple transmission formula," *Proceedings of the IRE*, vol. 34, no. 5, pp. 254–256, May 1946.

[115] J. L. Miller and E. Friedman, *Photonics Rules of Thumb: Optics, Electro-Optics, Fiber Optics, and Lasers*, 3rd ed. Bellingham, Washington: SPIE Press, 1996.

[116] B. E. A. Saleh and M. C. Teich, *Fundamentals of Photonics*, 3rd ed. John Wiley & Sons, 2019.

[117] A. E. Siegman, "Defining and Measuring Laser Beam Quality," in *Solid State Lasers: New Developments and Applications*, M. Inguscio and R. Wallenstein, Eds. Boston, MA: Springer US, 1993, pp. 13–28.

[118] D. G. Gilmore, *Spacecraft Thermal Control Handbook, Volume I: Fundamental Technologies*. The Aerospace Corporation, 2002.

[119] M. I. Mishchenko, L. D. Travis, and A. A. Lacis, *Scattering, Absorption, and Emission of Light by Small Particles*. Cambridge, UK: Cambridge University Press, 2002. [Online]. Available: http://www.giss.nasa.gov/~crmim/books.html

[120] A. Quirantes, "A T-matrix method and computer code for randomly oriented, axially symmetric coated scatterers," *Journal of Quantitative Spectroscopy and Radiative Transfer*, vol. 92, pp. 373–381, may 2005.

[121] W. R. C. Somerville, B. Auguié, and E. C. Le Ru, "Smarties: User-friendly codes for fast and accurate calculations of light scattering by spheroids," *Journal of Quantitative Spectroscopy and Radiative Transfer*, vol. 174, pp. 39–55, 2016.

[122] W. Somerville, B. Auguié, and E. Le Ru, "A new numerically stable implementation of the T-matrix method for electromagnetic scattering by spheroidal particles," *Journal of Quantitative Spectroscopy and Radiative Transfer*, vol. 123, pp. 153–168, jul 2013.

[123] M. I. Mishchenko *et al.*, *Multiple scattering of light by particles: radiative transfer and coherent backscattering*, 1st ed. Cambridge: Cambridge Univ. Press, 2006.

[124] J. R. Szalay and M. Horányi, "Lunar meteoritic gardening rate derived from in situ LADEE/LDEX measurements," *Geophysical Research Letters*, vol. 43, no. 10, pp. 4893–4898, 2016.

[125] A. P. Golub' *et al.*, "Dusty plasma system in the surface layer of the illuminated part of the moon," *JETP Letters*, vol. 95, no. 4, pp. 182–187, apr 2012.

[126] N. A. Kalyuzhnyy *et al.*, "Ingaas metamorphic laser ($\lambda = 1064$ nm) power converters with over 44% efficiency," in *AIP Conference Proceedings*, vol. 2012, no. 1. AIP Publishing, September 2018.

[127] H. A. MacLeod and H. A. MacLeod, *Thin-Film Optical Filters*, 4th ed. Boca Raton: CRC Press, jul 2010.

[128] D. J. Schroeder, *Astronomical Optics*. Elsevier Science, 2000, google-Books-ID: v7E25646wz0C.

[129] R. N. Wilson, *Reflecting Telescope Optics I*, ser. Astronomy and Astrophysics Library, I. Appenzeller *et al.*, Eds. Berlin, Heidelberg: Springer, 1996.

[130] W. J. Smith, *Modern Optical Engineering: The Design of Optical Systems*, 4th ed. McGraw-Hill Education, 2008.

[131] K. Yang *et al.*, "Review of research on lunar dust dynamics," *Astrophysics and Space Science*, vol. 367, no. 7, p. 67, 2022.

[132] H. Sharma *et al.*, "Constraining Low-Altitude Lunar Dust Using the LADEE-UVS Data," *Journal of Geophysical Research: Planets*, vol. 126, no. 11, p. e2021JE006935, 2021.

[133] T. Nie and P. Gurfil, "Lunar frozen orbits revisited," *Celestial Mechanics and Dynamical Astronomy*, vol. 130, no. 10, p. 61, sep 2018.

[134] M. Lara, S. Ferrer, and B. De Saedeleer, "Lunar Analytical Theory for Polar Orbits in a 50-Degree Zonal Model Plus Third-Body Effect," *The Journal of the Astronautical Sciences*, vol. 57, no. 3, pp. 561–577, jul 2009.

[135] G. A. Landis, "Laser power beaming for lunar polar exploration," in *AIAA Propulsion and Energy 2020 Forum*, 2020, p. 3538.

[136] X. L. Meng *et al.*, "Enhanced heat transfer characteristics using dimples in the receiving end of laser wireless power transmission system," *Applied Thermal Engineering*, vol. 252, p. 123619, 2024.

[137] Y. Li and J. Katz, "Optimum focusing of gaussian laser beams: beam waist shift in spot size minimization," *Optical Engineering*, vol. 33, no. 4, pp. 1152–1155, 1994.

APPENDIX A MISALIGNMENT ERROR ANGLE MODEL

This methodology is based on [72]. The elevation misalignment error angle ψ_e and the azimuth misalignment error angle ψ_a can be statistically modeled using a zero-mean Gaussian distribution as follows

$$f(\psi_e) = \frac{1}{\sqrt{2\pi\sigma_e^2}} \exp\left(\frac{-\psi_e^2}{2\sigma_e^2}\right), \tag{A.1}$$

$$f(\psi_a) = \frac{1}{\sqrt{2\pi\sigma_a^2}} \exp\left(\frac{-\psi_a^2}{2\sigma_a^2}\right), \tag{A.2}$$

where σ_e^2 and σ_a^2 represent the variances of the elevation and azimuth misalignment angles, respectively. It is important to note that the elevation and azimuth misalignment errors are independent and identically distributed.

The radial misalignment error angle ψ, both at the transmitter (ψ_t) and the receiver (ψ_r), can then be modeled statistically using the Rayleigh distribution. This is done under the assumption that $\sigma_\psi = \sigma_e = \sigma_a$, due to the symmetry, as follows

$$\psi = \sqrt{\psi_e^2 + \psi_a^2}, \tag{A.3}$$

$$f(\psi_t) = \frac{\psi_t}{\sigma_\psi^2} \exp\left(\frac{-\psi_t^2}{2\sigma_\psi^2}\right), \tag{A.4}$$

$$f(\psi_r) = \frac{\psi_r}{\sigma_\psi^2} \exp\left(\frac{-\psi_r^2}{2\sigma_\psi^2}\right). \tag{A.5}$$

APPENDIX B HARVESTED POWER DEMONSTRATION

We aim to calculate the harvested power P_h for a circular receiver of radius R, considering a Gaussian beam intensity and efficiency factors. The total harvested power P_h is given by

$$P_h = \eta_{\text{Rx}} \cdot \eta_{\text{dust}} \cdot \int_A I(r, z)\, dA, \tag{B.1}$$

where η_{Rx} is the conversion efficiency of the receiver, and η_{dust} accounts for the attenuation of laser intensity due to lunar dust. The intensity $I(r, z)$ of the Gaussian beam at a radial distance r from the beam center is expressed as

$$I(r, z) = \frac{2P_t}{\pi w(z)^2} \exp\left(-\frac{2r^2}{w(z)^2}\right), \tag{B.2}$$

where P_t is the transmitted power, $w(z)$ is the beam radius at distance z, and r is the radial distance from the beam center. For a circular receiver with radius R, we can compute P_h by setting up the integral in polar coordinates

$$P_h = \eta_{\text{Rx}} \cdot \eta_{\text{dust}} \cdot \int_0^{2\pi} \int_0^R I(r, z)\, r\, dr\, d\theta. \tag{B.3}$$

Substituting the Gaussian intensity function into the integral, we obtain

$$P_h = \eta_{\text{Rx}} \cdot \eta_{\text{dust}} \cdot \frac{2P_t}{\pi w(z)^2} \int_0^{2\pi} \int_0^R \exp\left(-\frac{2r^2}{w(z)^2}\right) r\, dr\, d\theta. \tag{B.4}$$

Since the integrand does not depend on θ, the integration over θ simplifies to $\int_0^{2\pi} d\theta = 2\pi$, reducing the expression to

$$P_h = \eta_{\text{Rx}} \cdot \eta_{\text{dust}} \cdot \frac{4P_t}{w(z)^2} \int_0^R \exp\left(-\frac{2r^2}{w(z)^2}\right) r\, dr. \tag{B.5}$$

The remaining radial integral can be evaluated using the standard result

$$\int_0^R e^{-ar^2} r\, dr = \frac{1}{2a}\left(1 - e^{-aR^2}\right), \tag{B.6}$$

where $a = \frac{2}{w(z)^2}$, yielding

$$Integral = \frac{w(z)^2}{4}\left(1 - \exp\left(-\frac{2R^2}{w(z)^2}\right)\right). \tag{B.7}$$

Substituting this result back into the expression for P_h, we obtain

$$P_h = \eta_{\text{Rx}} \cdot \eta_{\text{dust}} \cdot P_t \left(1 - \exp\left(-\frac{2R^2}{w(z)^2}\right)\right). \tag{B.8}$$

This formula expresses the harvested power P_h as a function of the transmitted power P_t, the receiver's radius R, and the beam size $w(z)$. The efficiency factors η_{Rx} and η_{dust} account for the efficiency of the receiver conversion and the reduction in efficiency due to dust, respectively. The exponential term represents the fraction of the beam's power not captured by the receiver due to its finite size. When R is much larger than $w(z)$, the exponential term approaches zero, and P_h approaches $\eta_{\text{Rx}} \cdot \eta_{\text{dust}} \cdot P_t$. Conversely, when R is small compared to $w(z)$, the exponential term significantly reduces the harvested power.

APPENDIX C FOCUSING LENS AT THE LASER OUTPUT

The position and size of the waist image after passing through a lens can be determined using established optical equations [137]. Starting with the fundamental relationship, the position z' of the image waist is given by

$$z' = \left[\frac{1}{\frac{z_R^2}{f-z} - z} + \frac{1}{f} \right]^{-1}, \tag{C.1}$$

and the waist size w_0' at the image position is

$$w_0' = \frac{w_0}{\sqrt{\left(1 - \frac{z}{f}\right)^2 + \left(\frac{z_R}{f}\right)^2}}, \tag{C.2}$$

where $z_R = \frac{\pi d_{\text{Tx}}^2}{4\lambda}$. Here, z represents the object waist position along the same axis as z', with positive values indicating the propagation direction and $z = 0$ corresponding to the laser output. The parameters w_0 and f denote the object waist size and the lens's focal length, respectively, with f being positive for focusing lenses and negative for diverging lenses.

Assuming the output beam is perfectly collimated, we set $z = 0$ and $w_0 = \frac{d_{\text{Tx}}}{2}$. Substituting these values simplifies the equations to

$$z' = \frac{z_R^2 f}{f^2 + z_R^2} \tag{C.3}$$

and

$$w_0' = \frac{d_{\text{Tx}}}{2\sqrt{1 + \left(\frac{z_R}{f}\right)^2}} = \frac{f d_{\text{Tx}}}{2\sqrt{f^2 + z_R^2}}. \tag{C.4}$$

Next, we determine the target diameter d_{Rx} as a function of the distance z beyond the image position z' using the equation

$$d_{\text{Rx}} = 2w_0' \sqrt{1 + \left(\frac{\lambda(z - z')}{\pi w_0'^2} \right)^2}, \quad z > z'. \tag{C.5}$$

To maximize z, we solve for z in terms of d_{Rx} by isolating z:

$$z = \frac{\pi w_0'}{2\lambda}\sqrt{d_{\mathrm{Rx}}^2 - 4w_0'^2} + z' = \frac{\pi f d_{\mathrm{Tx}}}{4\lambda\sqrt{f^2+z_R^2}}\sqrt{d_{\mathrm{Rx}}^2 - \frac{f^2 d_{\mathrm{Tx}}^2}{f^2+z_R^2}} + \frac{z_R^2 f}{f^2+z_R^2}. \tag{C.6}$$

This can be further expanded to

$$z = \frac{\pi f d_{\mathrm{Tx}}}{4\lambda(f^2+z_R^2)}\sqrt{d_{\mathrm{Rx}}^2(f^2+z_R^2) - f^2 d_{\mathrm{Tx}}^2} + \frac{z_R^2 f}{f^2+z_R^2}, \tag{C.7}$$

and subsequently rewritten as

$$z = \frac{f}{f^2+z_R^2}\left[\frac{\pi d_{\mathrm{Tx}}}{4\lambda}\sqrt{d_{\mathrm{Rx}}^2 z_R^2 + f^2(d_{\mathrm{Rx}}^2 - d_{\mathrm{Tx}}^2)} + z_R^2\right], \tag{C.8}$$

where $z_R = \frac{\pi d_{\mathrm{Tx}}^2}{4\lambda}$.

To simplify the expression, we define $\alpha = \frac{f}{z_R}$, leading to

$$z = \frac{\alpha}{\alpha^2+1}\left[\frac{\pi d_{\mathrm{Tx}}}{4\lambda}\sqrt{d_{\mathrm{Rx}}^2 + \alpha^2(d_{\mathrm{Rx}}^2 - d_{\mathrm{Tx}}^2)} + z_R\right]. \tag{C.9}$$

By incorporating M^2 into the development, and by defining α_{opt} as the optimal α value that maximizes z, we get

$$z_{\max}(\alpha_{\mathrm{opt}}) = \frac{\alpha_{\mathrm{opt}}}{\alpha_{\mathrm{opt}}^2+1}\cdot\frac{\pi d_{\mathrm{Tx}}}{4\lambda M^2}\left[\sqrt{d_{\mathrm{Rx}}^2 + (d_{\mathrm{Rx}}^2 - d_{\mathrm{Tx}}^2)\alpha_{\mathrm{opt}}^2} + d_{\mathrm{Tx}}\right]. \tag{C.10}$$

Given the complexity of the derivative with respect to α, obtaining an analytical solution for the maximum z_{max} is difficult. Thus, the maximum value of z_{max} is determined numerically.

APPENDIX D LINE-OF-SIGHT DISTANCE DEMONSTRATION

We consider a spherical Moon of radius R. A transmitter is located at a height h_t above the Moon's surface, and a receiver is positioned at a height h_r above the surface.

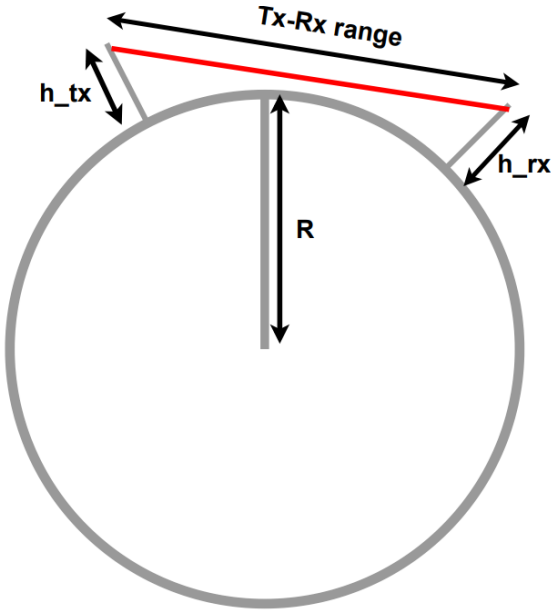

Figure D.1 Geometry of the transmitter and receiver over the Moon's surface.

The minimum possible LoS distance occurs when both the transmitter and receiver are just above the horizon relative to each other, as can be deduced from Figure D.1. If they are below, the curvature of the Moon will block the transmission. To calculate this distance, we first determine the distance to the horizon from a point at height h above a spherical body.

Using the Pythagorean theorem, the distance d to the horizon from a height h is derived from

$$(R+h)^2 = R^2 + d^2. \tag{D.1}$$

Solving for d:

$$d = \sqrt{2Rh + h^2}. \tag{D.2}$$

Thus, the distances from the transmitter and receiver to their respective horizons are

$$d_t = \sqrt{2Rh_t + h_t^2} \quad \text{and} \quad d_r = \sqrt{2Rh_r + h_r^2}. \tag{D.3}$$

The total minimum possible LoS distance between the transmitter and receiver is the sum of these two distances

$$\text{TrRxRange} = d_t + d_r = \sqrt{2Rh_t + h_t^2} + \sqrt{2Rh_r + h_r^2}. \tag{D.4}$$

For clarity, this can be rewritten as

$$\text{TrRxRange}(h_t, h_r) = \sqrt{h_t^2 + 2Rh_t} + \sqrt{h_r^2 + 2Rh_r}. \tag{D.5}$$

This final formula gives the minimum possible LoS distance between a transmitter and receiver located above the surface of the Moon, both located at a certain height, before the curvature of the Moon blocks the transmission.